Mix, A.C., Tiedemann, R., Blum, P., et al., 2003
Proceedings of the Ocean Drilling Program, Initial Reports Volume 202

11. Site 1240[1]

Shipboard Scientific Party[2]

INTRODUCTION

Site 1240 (proposed Site PAN-2A) is located at 0°1.311′N, 86°27.758′W, about midway between mainland Ecuador and the Galapagos Islands (Fig. F1). North of Carnegie Ridge at 2921 m water depth in the Panama Basin, the site is in a small east-west–trending trough in classical abyssal hill topography typical of seafloor spreading centers. Relief is 200–300 m between hills and valleys (Fig. F2). The basaltic oceanic crust underlying the site was formed at the Cocos spreading center about 3 m.y. ago (Hey et al., 1977). A tectonic backtrack path of the Nazca plate (Pisias et al., 1995) moved the site westward and slightly to the south at greater ages, but given the relatively young age of the site, tectonic movement here was slight.

Site 1240 was chosen in an abyssal valley close to the equator to monitor variations in equatorial upwelling at high resolution. A seismic profile (Fig. F3) documents pelagic drape over the abyssal hills, with a slight thickening of the section within the valleys. Sediment cover of 250–280 m is relatively thick for the region, given the young age of the crust, suggesting that this abyssal valley acts as a sediment trap to collect the heavy biogenic rain below the productive equatorial upwelling system. Dominant sediments in the region are foraminifer-bearing nannofossil-diatom ooze, with some intervals of diatom ooze and occasional ash layers.

Equatorial upwelling is strong over Site 1240 (Fig. F4), driven by southeasterly trade winds, especially in Southern Hemisphere winter. The strongest upwelling occurs just south of the equatorial front that separates cool, relatively high salinity surface waters south of the equator from the warm, low-salinity waters of the Panama Basin (Strub et al., 1998). Nutrient-rich waters of the Equatorial Undercurrent (EUC) serve as source waters for the upwelling (Levitus et al., 1993), but nitrate and phosphate are not fully utilized by the phytoplankton in spite of high

F1. Sites 1238–1242 and regional bathymetry, p. 22.

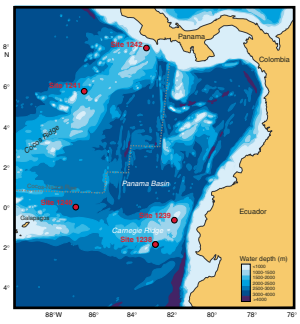

F2. High-resolution swath bathymetry, p. 23.

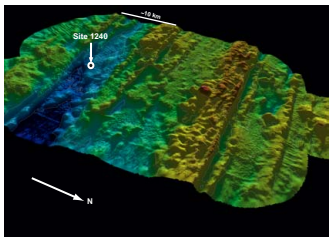

F3. Seismic profile at Site 1240, p. 24.

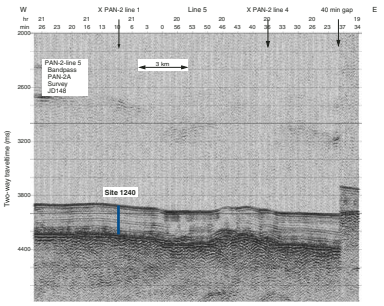

F4. Upper-ocean features of the eastern tropical Pacific, p. 25.

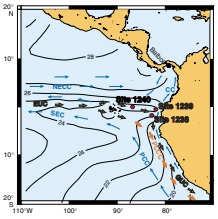

[1]Examples of how to reference the whole or part of this volume.
[2]Shipboard Scientific Party addresses.

Ms 202IR-111

biomass in near-surface waters (Figs. F5, F6). A limited supply of micronutrients such as iron, for which the EUC is a major source, may play an important role as a regulator of production (Murray et al., 1994).

Site 1240 is likely to record changes in upwelling and biological production, as well as long-term changes in upper-ocean temperature and pycnocline depth. The surface-ocean properties of the eastern equatorial Pacific are sensitive to interannual to decadal oscillations such as those of the well-known El Niño Southern Oscillations (ENSO) (Cane, 1986) as well as longer-term changes associated with the Pleistocene ice ages (Pisias and Mix, 1997; Andreasen and Ravelo, 1997; Mix et al., 1999; Lea et al., 2000; Beaufort et al., 2001).

Although Site 1240 is relatively young, which limits the extent of plate movement associated with tectonic drift, even small changes in position may be important near the equator. Plate tectonic backtrack locations can be used to predict general features of oceanographic change at Site 1240, assuming that overall conditions in the region remain constant and that the only change in the system is drift of the site location relative to this fixed oceanographic background (Fig. F7). In this analysis, we ignore changes in the position of the continental margin through time. Sampling of modern oceanographic atlas values at the paleosite locations suggests that from 3 m.y. ago, sea-surface temperatures at Site 1240 may have been slightly cooler (~1°C), salinities were higher, and pycnocline depths were shallower than today. These changes are predicted because Site 1240 was south of the equator just a few million years ago. Here, upwelling into the South Equatorial Current (SEC) is greater than just north of the equator, so we might expect a slight increase in biological production at greater ages due to this geographic effect. In the absence of other regional changes in ocean circulation or tectonics, we would expect that biogenic sediment accumulation rates at Site 1240 would have been relatively high in the past. Eolian sediment components may also have been more prevalent at greater ages when Site 1240 backtracks across the northern edge of the Atacama dust plume near the equator (Molina-Cruz, 1977). Significant deviations from these general trends, if detected in the sediment cores, would imply changes in regional oceanographic or climatic conditions, or errors in the tectonic backtrack or age models.

The deep waters at Site 1240 (Fig. F6) derive from middepth waters that enter the Panama Basin at its sill depth of ~2000–2500 m, both in the north from the Guatemala Basin and in the south from the Peru Basin, as well as from deeper Peru Basin Water that enters the Panama Basin through the Ecuador Trench (Lonsdale, 1976). Anomalously high geothermal heating in the basin helps to maintain a short residence time (40–50 yr) of waters within the basin. In spite of this active circulation, Panama Basin deep waters are relatively depleted in oxygen and $\delta^{13}C$ and enriched in nutrients relative to waters at equivalent depths outside the basin because of in situ oxidation of ^{13}C-depleted organic matter (Kroopnick, 1974). As a result of these processes, the long-term history of benthic foraminiferal $\delta^{13}C$ here combines global, regional, and local effects (Mix et al., 1995).

The primary objective at Site 1240 is to provide a continuous sedimentary sequence of late Pliocene to Quaternary sediment to assess variability of upper-ocean processes, including equatorial upwelling, at millennial to orbital timescales.

F5. Chlorophyll distributions in surface waters, p. 26.

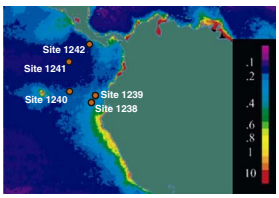

F6. Meridional cross section of water masses, p. 27.

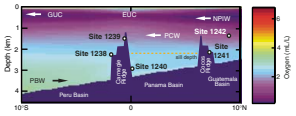

F7. Modern ocean properties at backtrack locations of Site 1240, p. 28.

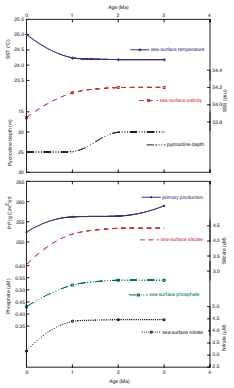

OPERATIONS

The 268-nmi transit to Site 1240 (proposed Site PAN-2A) required 22.2 hr at an average speed of 12.1 kt. Shipboard 3.5-kHz precision depth recorder (PDR) records were used to check the final site characteristics by comparison with precruise survey data. The vessel was on station by 0100 hr on 16 May 2002.

Hole 1240A

Hole 1240A was initiated with the advanced piston corer (APC) and the drill bit at 2928 meters below rig floor (mbrf) at 0750 hr on 16 May. The seafloor depth that was estimated by the amount of recovery of the first core was 2934.0 mbrf. This was 2.4 m shallower than the corrected PDR depth of 2936.4 mbrf. Piston coring penetrated the sediment section to 253 meters below seafloor (mbsf) without resorting to the extended core barrel (XCB). Coring in the hole was terminated when the last piston core (28H) did not achieve a full stroke and was recovered with a bent core barrel, damaged cutting shoe, and 3.87 m of basaltic gravel and nannofossil ooze. The APC cored 253.0 m and recovered 264.0 m (recovery = 104%) (Table T1).

T1. Operations summary, Site 1240, p. 58.

The nonmagnetic core barrel was deployed on even-numbered cores up to and including Core 18H, starting with Core 2H. A total of six core barrels were drilled over starting with Core 22H. The piston cores were oriented starting with Core 4H. Downhole temperature measurements were taken with the APC temperature (APCT) tool at various depths as summarized in Table T1. The odoriferous cores were stored on the catwalk rack to degas H_2S subsequent to splitting. Headspace measurements on the cores yielded trace amounts of methane (<300 ppm) and ethane (<2 ppm). No higher molecular weight hydrocarbon compounds were detected. The bit was pulled free of the seafloor at 1145 hr on 17 May.

Hole 1240B

The vessel was offset 10 m west of Hole 1240A. Prior to coring, a bottom water temperature measurement was obtained with the APCT tool with the bit positioned just above the seafloor. To obtain the desired stratigraphic overlap with the first hole, the bit was placed at 2931.0 mbrf and Hole 1240B was initiated with the APC at 1320 hr. The seafloor depth derived from the recovery of the first core was 2931.8 mbrf. Piston coring combined with a 2-m drilled interval (75.2–77.2 mbsf) deepened the hole to 248.2 mbsf. The cored interval was 246.2 m with 254.8 m recovered (recovery = 104%) (Table T1).

The nonmagnetic core barrel was deployed on odd-numbered cores up to and including Core 21H. Eight core barrels were drilled over in this hole starting with Core 19H. The cores were oriented starting with Core 3H. The depths of downhole temperature measurements are listed in Table T1. The bit was pulled free of the seafloor at 1400 hr on 18 May.

Hole 1240C

The vessel was offset 10 m west of Hole 1240B, and Hole 1240C was initiated with the APC at 1505 hr on 18 May. The bit was positioned at

a depth of 2934.0 mbrf, or 2.2 m deeper than the calculated mudline depth of Hole 1240B (2931.8 mbrf). Piston coring deepened the hole to 80.2 mbsf. Two intervals were drilled to maintain the proper overlap with the data from the previous two holes (0.0–2.2 and 32.7–42.2 mbsf). The cored interval was 76.0 m with 75.3 m recovered (recovery = 99%) (Table T1).

The nonmagnetic core barrel was deployed on even-numbered cores. No core barrels were drilled over. Cores were oriented starting with Core 3H. Additional downhole temperature measurements are summarized in Table T1. The temperature measurements from all holes yielded a gradient of 2.6°C/100 m. The bit was pulled free of the seafloor at 2340 hr on 18 May.

Hole 1240D

The vessel was offset 10 m west of Hole 1240C, and Hole 1240D was initiated with the APC at 0025 hr on 18 May. The bit was positioned at a depth of 2935.0 mbrf, or 3.2 m deeper than the calculated mudline depth of Hole 1240B (2931.8 mbrf). Piston coring and drilling deepened the hole to 31.7 mbsf. One interval was drilled to maintain the proper overlap with the data from the previous two holes (0.0–3.2 mbsf). The cored interval was 28.5 m with 28.6 m recovered (recovery = 100.4%) (Table T1). The nonmagnetic core barrel was deployed on the two odd-numbered cores. Core 3H was oriented.

The vessel was secured for transit and departed for Site 1241 at 0915 hr on 19 May.

COMPOSITE SECTION

We built a meters composite depth (mcd) scale to Section 202-1240A-28H-3 (0.00–282.94 mcd) and a splice (as defined in **"Composite Section,"** p. 4, in the "Explanatory Notes" chapter) that documents complete recovery for the upper 278.36 mcd. The splice ranges from the top of Core 202-1240A-1H to the bottom of Section 202-1240A-27H-7 (Tables T2, T3). All APC cores except for 202-1239A-28H can be correlated to the splice at Site 1240.

The mcd scale and the splice are based primarily on the stratigraphic correlation of whole-core Oregon State University Fast Track magnetic susceptibility data (OSUS-MS) measurements collected at 5-cm intervals with a 10-s integration time (Fig. F8; Tables T4, T5, T6, T7). In one interval (~67–74 mcd), for the tie between Core 202-1240B-7H and 202-1240C-7H, gamma ray attenuation (GRA) bulk density was used to verify the correlation. Tie points (Table T3) were then used to construct representative spliced records for multisensor track magnetic susceptibility (MST-MS), GRA bulk density, and natural gamma radiation (NGR) data (Fig. F9) and color reflectance (L*, a*, and b*) data (Fig. F10).

We assumed that the uppermost sediment (the "mudline") in Core 202-1240C-1H was the sediment/water interface. A mudline was also recovered in Core 202-1240B-1H. Core 202-1240C-1H is the "anchor" in the composite depth scale. From this anchor we worked downhole, correlating records on a core-by-core basis.

A comparison of the mcd and mbsf depth scales (Fig. F11) shows that the mcd scale is on average 11% longer than the mbsf scale. Because the growth factor of 1.11 in the splice was relatively constant and the splice represents ~98% of the drilled section at Site 1240, we appended Core

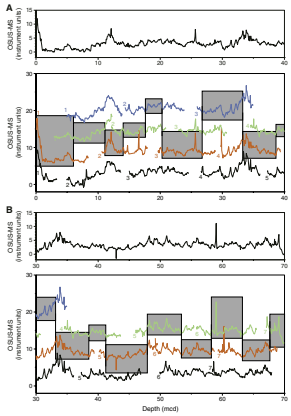

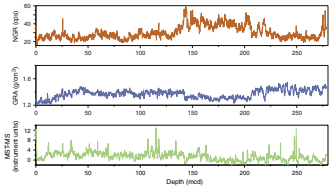

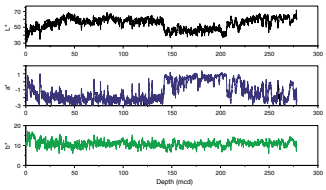

202-1240A-28H by assuming an 11% (1.05 m) offset from the core above.

To facilitate the calculation of mass accumulation rates (MARs), we provide corrected meters composite depth (cmcd) in Table T2 and in Table T3 for depths within the splice.

LITHOSTRATIGRAPHY

A 282.9-m sedimentary sequence was recovered from four holes at Site 1240. Basement was reached in Hole 1240A, where basalt was recovered. The sediments at Site 1240 are mainly nannofossil ooze and diatom nannofossil ooze. Siliciclastic contents are very low and primarily consist of clay minerals. Eight ash layers are present and can be correlated between holes. The presence of brown glass in some of the layers may indicate a different source of ash layers between Site 1240 and previous sites.

A single lithologic unit with three subunits is defined at Site 1240 (Table T8). Subunit boundaries are defined by physical properties and minor lithologic differences (Figs. F12, F13). Subunit IA (0–142.2 mcd; ~0–1.7 Ma) is composed of nannofossil ooze with relatively high percentages of diatoms. Sediments are highly bioturbated, showing very heterogenous color mottling. Subunit IB (142.2–206.4 mcd; ~1.7–2.1 Ma) is enriched in diatoms and siliciclastic components relative to the other two subunits. Color banding (centimeter scale) is frequently present throughout this subunit. Darker bands are associated with the occurrence of pennate diatoms. The overall color is more reddish yellow than in Subunit IA, represented by high values of a* (Fig. F12). Subunit IB is also characterized by relatively low values in grain density, probably as a result of a high biogenic silica content (Fig. F14) and high values of total organic carbon (TOC) (see "Geochemistry," p. 14) and chlorins (Fig. F15). All physical properties show a substantial change in Subunit IB relative to the adjacent subunits, with sharp transitions over intervals of apparently <1 m. Ash layers are absent within Subunit IB. Sediments and physical properties in Subunit IC (206.4–282.9 mcd; ~2.1–2.6 Ma) are very similar to those in Subunit IA.

Compositional differences observed between subunits may reflect the history of primary productivity at Site 1240. Characteristics of Subunit IB indicate an enhancement of equatorial upwelling and thus increased primary productivity between ~1.7 and 2.1 Ma, probably as a result of intensified atmospheric and oceanic circulation. Increased siliciclastic content in that interval also suggests more effective eolian transport toward Site 1240, supporting a potential intensification of atmospheric circulation.

Description of Lithologic Unit

Unit I

Intervals: Cores 202-1240A-1H through 28H; Cores 202-1240B-1H through 26H; Cores 202-1240C-1H through 8H; and Cores 202-1240D-1H through 3H

Depths: 0–282.93 mcd; Hole 1240A: 0–254.38 mbsf (0–282.93 mcd); Hole 1240B: 0–248.81 mbsf (0–274.46 mcd); Hole 1240C: 2.20–80.6 mbsf (2.85–87.30 mcd); and Hole 1240C: 3.20–31.59 mbsf (4.85–35.39 mcd)

F11. A comparison of the mbsf and mcd scales, p. 36.

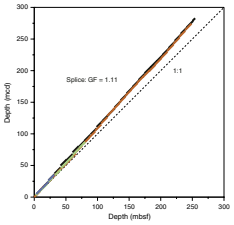

T8. Lithologic Unit I, Site 1240, p. 67.

F12. Lithostratigraphic summary, p. 37.

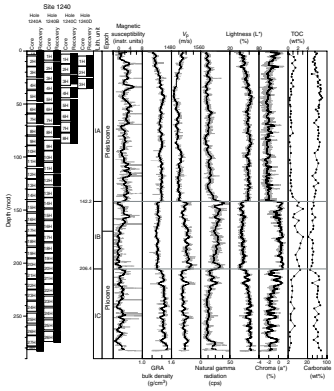

F13. Major components in smear slides, p. 38.

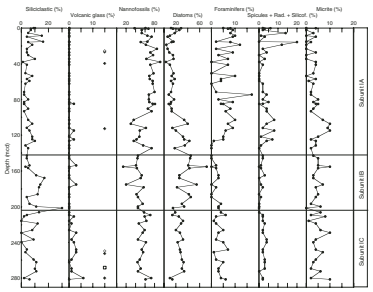

F14. Physical properties measurements, p. 39.

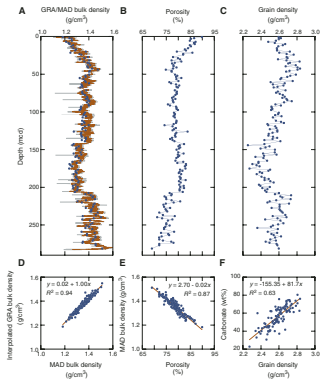

Age: Pleistocene to late Pliocene (0–2.6 Ma)

A single lithologic unit (Unit I) is defined and divided into three subunits (Table **T8**) on the basis of visual core description, smear slide analysis, magnetic susceptibility, color reflectance, *P*-wave velocity, NGR, moisture and density (MAD), and GRA bulk density measurements. Depth boundaries of the subunits are based primarily on changes in physical properties (Fig. **F12**). All three subunits contain nannofossil ooze; however, in Subunit IB, nannofossil-bearing diatom ooze becomes more frequent. Subunit IB is distinguished from Subunits IA and IC by relatively low values of magnetic susceptibility and GRA bulk density, high *P*-wave velocity (V_P) and NGR, low lightness (L*), and high a*.

At Site 1240, GRA bulk density and MAD bulk density are well correlated (r^2 = 0.94) (Fig. **F14**). Porosity mirrors changes in bulk density. Grain density is largely controlled by carbonate content, which is typical in sediments composed mostly of carbonate and opal microfossils (r^2 = 0.63) (Fig. **F14**). Predictive relationships between reflectance and either carbonate or TOC via a multiple linear regression are relatively good for both components (i.e., r^2 = ~0.8). Organic pigments are detected in absorbance features at 410, 510, 560, and 650 nm in reflectance spectra (Fig. **F15**). The strongest absorption feature at 650 nm, which persists throughout the sediment column, is probably a result of chlorins (i.e., chlorophyll-related pigments). The chlorin optical index is well correlated to the TOC (r^2 = ~0.7) (Fig. **F15**).

Subunit IA

Intervals: 202-1240A-1H-1, 0 cm, through 15H-1, 20 cm; 202-1240B-1H-1, 0 cm, through 14H-3, 80 cm; 202-1240C-1H-1, 0 cm, through 8H-CC, 16 cm; and 202-1240D-1H-1, 0 cm, through 3H-CC, 19 cm

Depths: 0.0–142.2 mcd; Hole 1240A: 0.0–127.2 mbsf; Hole 1240B: 0.0–128.5 mbsf; Hole 1240C: 2.20–80.6 mbsf; and Hole 1240D: 3.2–31.59 mbsf

Age: Pleistocene (0–1.7 Ma)

Subunit IA is dominated by diatom-bearing nannofossil ooze and nannofossil ooze. Clay- (diatom) bearing nannofossil ooze is present in the top ~34 mcd and some foraminifer- (diatom) bearing nannofossil ooze is sporadically present throughout the subunit. Diatom nannofossil ooze and nannofossil diatom ooze are present below ~100 mcd. The sediment color alternates between pale olive and light olive gray. These colors are not homogeneously distributed but form amorphous mottles throughout the entire subunit, indicating intense bioturbation. Vertical burrows (5–20 cm in length) and *Zoophycos* traces are also common (Fig. **F16**).

The sediments are dominated by biogenic components (Fig. **F17**), which consist mainly of nannofossils (~40% to ~80%) and diatoms (~10% to ~40%), with minor amounts of foraminifers (~0% to ~15%), spicules, silicoflagellates, and radiolarians (the last three combined = ~3%). Below ~100 mcd, an increase in diatom abundance from 20% to 40% accompanies a decline in nannofossil abundance from 80% to 40%. Siliciclastics, mostly clay minerals, represent a minor component (~5%) of Subunit IA. Micrite is usually present, with values increasing to 5% in the interval of 100–125 mcd. Thin intervals (~40 cm) of color banding coincide with increases in diatom abundance (Fig. **F17**).

F15. Sequential depth plots, Site 1240, p. 40.

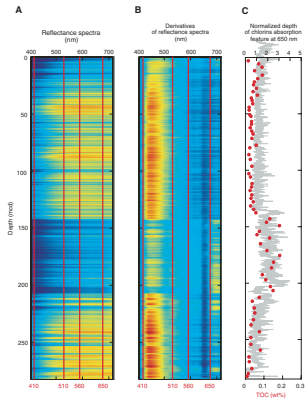

F16. Bioturbation, p. 41.

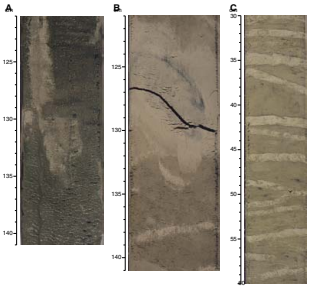

F17. Color banding, p. 42.

Three ash layers are present in Subunit IA (Table T9). These ashes are present both as patches and layers and, in all cases, show evidence of bioturbation (Fig. F18). The ash color varies between brownish, gray, and dark gray. The ash layers contain clear platy and vesicular glass. Accessory minerals include biotite, quartz, and feldspars, with rare occurrences of clinopyroxene and amphiboles. The uppermost ash layer (25.69–25.71 mcd) contains trace amounts of brown volcanic glass.

Overall, magnetic susceptibility is low (~1–4 instrument units) through this subunit, but the values are higher and more variable than those in Subunit IB (Fig. F12). NGR remains between ~5 and 19 cps in Subunit IA. GRA and MAD bulk densities increase between 0 and 45 mcd as a result of dewatering and compaction and remain stable at ~1.4 g/cm³ for the rest of the subunit. Lightness increases slightly from 0 to ~40 mcd and then remains stable through the base of the subunit.

Subunit IB

Intervals: 202-1240A-15H-1, 20 cm, through 21H-1, 90 cm, and 202-1240B-14H-3, 80 cm, through 20H-5, 105 cm
Depths: 142.2–206.4 mcd; Hole 1240A: 127.2–184.9 mbsf; and Hole 1240B: 128.5–188.75 mbsf
Age: early Pleistocene–late Pliocene (1.7–2.1 Ma)

The lithology in Subunit IB is variable and consists of nannofossil-bearing diatom ooze, diatom nannofossil ooze, and diatom-bearing nannofossil ooze. Clay-bearing diatom and/or nannofossil ooze also occur frequently. Color oscillates primarily between dark olive, olive, and olive gray. Intervals containing centimeter-thick color bands are frequent within Subunit IB (Fig. F17). The darker-colored bands contain higher abundances of pennate diatoms, such as *Thalassiothrix* spp., the major component of diatom mats (see **"Biostratigraphy,"** p. 10). Bioturbation, mottling, and burrow traces including *Zoophycos* are less abundant here than in Subunit IA. The intervals with color banding exhibit little evidence of bioturbation.

Nannofossil contents are slightly lower (~40% to ~60%) and diatoms generally more abundant (~30% to ~50%) in Subunit IB than in Subunit IA (Fig. F13). Other biogenic components (foraminifers, spicules, and silicoflagellates) are also present but in smaller percentages (<5%) than in Subunit IA. Siliciclastics, mainly clay minerals, are variable but, on average, are more abundant in this subunit (~10%). Micrite abundance in Subunit IB is similar to that in other subunits (0%–10%).

The physical properties data show abrupt shifts at 142 and 206 mcd, defining the boundaries of Subunit IB (Fig. F12). In Subunit IB, magnetic susceptibility is relatively low (~0–2 instrument units), whereas NGR is relatively high. NGR is more variable than in Subunit IA.

Bulk density shifts to lower values as a result of high porosity and then remains very stable (~1.3 g/cm³) throughout the subunit. Grain density is low in this subunit, consistent with greater concentrations of siliceous components (Fig. F14). *P*-wave velocities show consistently high values in Subunit IB (Fig. F12). High concentrations of biogenic silica are expected to result in a high *P*-wave velocity (e.g., Hamilton and Bachman, 1982; Dunbar, 2001) because angular grains in contact form a rigid framework conducive to the transmission of sound waves. A combination of low density and high compressional wave velocity, similar to the situation in Subunit IB, has been attributed elsewhere to the presence of abundant biogenic silica (e.g., Weber et al., 1997; Weber, 1998). Lightness values are distinctly lower than those in Subunits

T9. Ash layers, Site 1240, p. 68.

F18. Ash layers, p. 43.

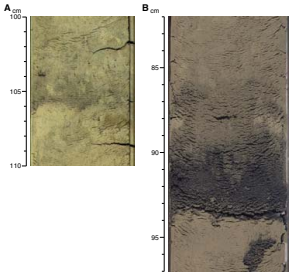

IA and IC. All color measurements at Site 1240 plot in the "yellow" domain of the a*-b* space (Fig. **F19**), but sediment in Subunit IB comprises a distinct color population characterized by a redder hue (i.e., a* > 0).

Subunit IB is characterized by relatively high TOC concentration (~3.4 wt%) (Fig. **F12**), which coincides with high chlorin abundance (Fig. **F15**). Carbonate concentrations are relatively low (~40 wt%) in this subunit (see **"Geochemistry,"** p. 14) in parallel with low grain density values (Fig. **F13**). Sedimentation rates appear to increase in Subunit IB from ~8 to ~13 cm/k.y. However, the age model for Site 1240 is tentative at this time and allows for alternative interpretation (see **"Age Model and Mass Accumulation Rates,"** p. 17).

Subunit IC

Intervals: 202-1240A-21H-1, 90 cm, through 28H-CC, 9 cm, and 202-1240B-20H-5, 105 cm, through 26H-CC, 32 cm
Depths: 206.4–282.93 mcd; Hole 1240A: 184.9–254.38 mbsf; and Hole 1240B: 188.75–248.81 mbsf
Age: late Pliocene (~2.1–2.6 Ma)

The lithology in Subunit IC is mainly diatom-bearing nannofossil ooze and diatom nannofossil ooze. Sediment color is olive, pale olive, and light olive gray. Color mottling is abundant throughout the subunit, indicating intense bioturbation. Burrow traces, including *Zoophycos* (Fig. **F16**), are commonly present, as observed in Subunit IA. The sediments near the basaltic basement contain vivid green mottles, indicative of enrichment in the smectite group of minerals, such as nontronite (Fig. **F20**), resulting from alteration of the basalt.

The major lithologic components of Subunit IC are of biogenic origin (Fig. **F13**). Nannofossils are predominant (~40%–70%), with lesser amounts of diatoms (~20%–40%). Abundances of the other biogenic components (foraminifers, spicules, silicoflagellates, and radiolarians) are slightly higher than in Subunit IB. Siliciclastics, primarily clay, are present in relatively low percentages (~0%–10%). In contrast to the previous subunits, volcanic glass is present as a minor component of the major lithology throughout Subunit IC. Micrite is present in amounts similar to the previous subunits (~5%).

Five ash layers are present in Subunit IC. Three of them are correlative between Holes 1240A and 1240B (Table **T9**). Some of the layers are diffuse as a result of bioturbation, whereas others have a clear, sharply defined base (Fig. **F18**). The ash color varies between light gray, dark gray, and black. With the exception of the layer at 268.03–268.12 mcd, ash layers in Subunit IC are mainly composed of platy and vesicular clear volcanic glass, with feldspars, biotite, and rare amphiboles. The ash layer at 249.46–249.54 mcd contains very small amounts of brownish glass. The ash layer at 268.03–268.12 mcd is composed of brown glass shards.

Physical properties are similar to those recorded in Subunit IA (Figs. **F12, F14**). Magnetic susceptibility values oscillate between ~0 and 3 instrumental units. NGR values are stable with some oscillations near ~15 cps, although values increase sharply near the base of the subunit (below 272.5 mcd). Bulk density values are more variable than in Subunit IA (~1.4 g/cm^3). Lightness increases in relation to Subunit IB.

F19. Color measurements, p. 44.

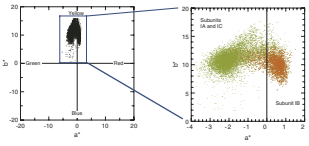

F20. Sediment above basaltic basement, p. 45.

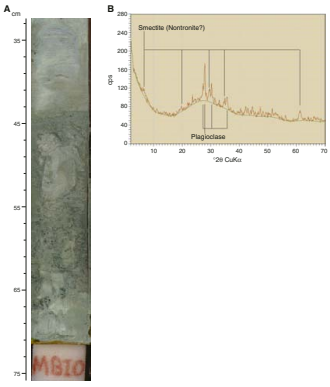

Interpretation and Depositional History

The recovered sedimentary sequence at Site 1240 forms a continuous record of the last ~2.6 m.y. (late Pliocene–Pleistocene) with unusually high sedimentation rates for a pelagic site (~8 cm/k.y. for Subunit IA; ~13 cm/k.y. for Subunits IB and IC). Such high sedimentation rates, together with the dominantly biogenic composition of the sediments, indicate a relatively high productivity regime. This interpretation is consistent with the present geographic location of the site beneath the equatorial upwelling zone, suggesting that this highly productive system has been active throughout the last 2.6 m.y.

Primary production at Site 1240 was dominated by calcareous nannoplankton. Diatoms were also important particularly between ~1.7 and 2.1 Ma (Subunit IB). Characteristics of the sediment during this time period (i.e., presence of layers enriched in pennate diatoms, higher TOC weight percentages, high chlorins, and increased sedimentation rates) are consistent with an overall increase in productivity at ~2.1 Ma, likely resulting from an increase in the strength of the equatorial upwelling system, leading to higher nutrient availability. Enhanced equatorial upwelling in the Pacific has been attributed to intensified atmospheric and oceanic circulation caused by an increased meridional temperature gradient (Farrell et al., 1995).

Intensified atmospheric circulation during this interval is further suggested by increased siliciclastic content within Subunit IB, which is most likely of eolian origin. A synchronous strengthening of the equatorial upwelling system and enhancement of eolian supply is consistent with results from Ocean Drilling Program (ODP) Leg 138 (Hovan, 1995). The dominance of clay-sized siliciclastic particles may indicate that siliciclastic transport to Site 1240 occurred via wet deposition. This enhanced siliciclastic input could provide additional nutrients, further contributing to the increase of primary productivity.

Grain compositions of ash layers are mostly similar to those for Sites 1238 and 1239, suggesting that the majority of the ash at Site 1240 might also originate from northern South American volcanism. However, some ash layers with brown volcanic glass as an accessory component (one in Subunit IA and one in Subunit IC) indicate the presence of an additional volcanic source. The presence of ash layers with minor amounts of brown volcanic glass, also observed at Site 1241, suggests that Central America is a possible source region (Cadet et al., 1982). In addition, the presence of an ash layer fully composed of brown glass (268.03–268.12 mcd) may indicate a hotspot source, such as Galapagos.

Ash layers are absent in Subunit IB, although ash layers were deposited at the more southern Sites 1238 and 1239 during the same time interval (~1.7–2.1 Ma) (Fig. F21). The distribution of ash layers in the equatorial Pacific is mainly controlled by the extent and location of the volcanic eruption, the high-altitude winds that are predominantly westerly, low-altitude winds that are dominated by the southeast trade winds, and by the directions of the surface currents. Today, Sites 1238–1240 are located below the path of the southeast trade winds. A weakening of the trade winds system or a strengthening of upper-atmosphere westerlies may have restricted the distribution of ash to the west and prevented a long-range transport of wind-blown material to the more distal location of Site 1240. Alternatively, the eastward flow of the very strong EUC at Site 1240 may have offset the atmospheric fallout pattern toward the east. However, the absence of ash in Subunit IB

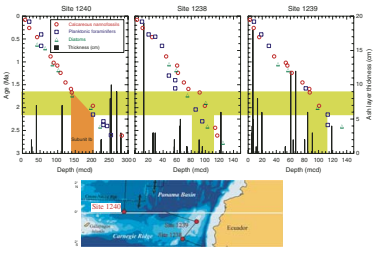

F21. Downhole distribution of ash layers, Sites 1240, 1239, and 1238, p. 46.

could also a result of an episode of relatively infrequent explosive volcanism in northern South America.

BIOSTRATIGRAPHY

The 283-m-thick sedimentary sequence recovered from the three holes cored at Site 1240 is of Pleistocene–late Pliocene age (Table T10; Fig. F32).

Persistent reworking of late Miocene microfossils is noted throughout the sequence; however, the three microfossil groups provide a well-constrained biostratigraphic model, which indicates an expanded Pleistocene–upper Pliocene sequence with a sediment accumulation rate of ~80 m/m.y (Table T10).

Calcareous nannofossils are generally abundant and well preserved but show a slight decline in preservation between 20 and 46 mcd and below 120 mcd. Foraminifers are common, except between 163 and 194 mcd, where the percentage of benthic foraminifers relative to total foraminifers also increases. Preservation is moderate to good. Diatoms are common throughout the section but have lower abundance and poorer preservation between 120 and 170 mcd (Fig. F22).

Calcareous Nannofossils

Calcareous nannofossils are abundant, and their preservation is good to moderate in all samples examined (Table T11; Fig. F22). All the well-known nannofossil datums for the Pleistocene have been determined within a sample spacing of ~1.5 m. The nannofossil datums show a relatively high and remarkably uniform sedimentation rate (~8 cm/k.y.) for the Pleistocene. *Florisphaera profunda,* a well-established nannofossil proxy for upwelling intensity, is few to abundant at the site. Thus, this site offers an excellent opportunity to use nannofossil assemblages to reconstruct centennial- to millennial-scale upwelling variability in the east equatorial Pacific and also to investigate variations on orbital or longer timescales.

The placements of all the nannofossil datums are listed in Table T10. All the Pleistocene nannofossil datums are well determined without any apparent complications. The late Pliocene datums are less well constrained and deserve some discussion. Two factors limited the nannofossil biostratigraphy of the upper Pliocene: (1) evidence of reworking of nannofossils and (2) the fact that the well-established nannofossil zonation relies exclusively on last occurrence (LO) datums for this interval. When there is indication of persistent reworking, it is generally difficult to precisely determine where the true LOs of marker species are. We tentatively considered the rare specimens of *Discoaster brouweri* above Sample 202-1240A-20H-CC (205.9 mcd) as reworked because they are less abundant and not consistently present. Similarly, we considered the rare and sporadic presence of *Discoaster surculus* above Sample 202-1240A-28H-3, 40 cm (282.5 mcd), as reworked. We placed the LO of *D. surculus* (2.61 Ma) between Samples 202-1240A-28H-2, 75 cm (281.3 mcd), and 28H-3, 40 cm (282.5 mcd), based on the more abundant and consistent presence of the species from the latter sample downhole. The deepest sample, 202-1240A-28H-CC (282.8 mcd), is just slightly below the LO of *D. surculus* and has an extrapolated age of ~2.7 Ma. It is clearly younger than 3.6 Ma, as *Sphenolithus* spp. are sporadic and considered reworked in these samples.

T10. Age-depth control points, p. 69.

F22. Calcareous nannofossils, planktonic and benthic foraminifers, and diatoms, Hole 1240A, p. 47.

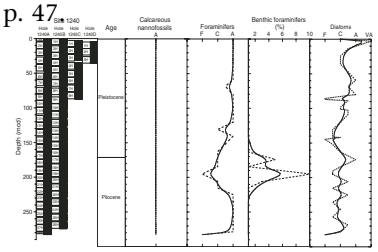

T11. Distribution of calcareous nannofossils, p. 70.

Planktonic Foraminifers

Planktonic foraminifers are generally common to frequent in samples from the upper part of Hole 1240A (mudline to Sample 202-1240A-15H-CC; 0–47.22 mcd). Between Samples 202-1240A-16H-CC and 21H-CC (163.03–215.29 mcd), the abundance of foraminifers decreases significantly (Table T11; Fig. F22) and radiolarians are particularly abundant in the >63-µm coarse fraction. In the lower part of Hole 1240A (Samples 202-1240A-22H-CC to 27H-CC; 224.97–278.67 mcd), foraminifers are common, except for the lowermost sample above the basalt (Sample 28H-CC; 282.84 mcd), where they are rare. Preservation is moderate overall, and planktonic tests show some evidence of dissolution (etching and fragmentation in 5%–30% of tests).

Diversity is relatively low, and assemblages tend to be dominated by typical upwelling taxa such as *Neogloboquadrina dutertrei* or *Neogloboquadrina pachyderma*. The Pleistocene–early Pliocene assemblage also frequently includes *Globigerina bulloides, Globorotalia menardii, Globorotalia scitula, Globorotalia tumida, Globigerinoides sacculifer, Globigerinoides trilobus, Neogloboquadrina acostaensis, Orbulina universa,* and *Sphaeroidinella dehiscens*. A preliminary biostratigraphy can be established for the Pleistocene–upper Pliocene interval recovered at Site 1240, based on the presence of some standard marker species (Table T10).

The LO of *Globigerinoides ruber* (pink) (0.12 Ma) is placed between Samples 202-1240A-2H-CC and 3H-CC (13.97–24.82 mcd), and the overlying section can be assigned to upper Pleistocene Subzone Pt1b of Berggren et al. (1995) (Fig. F12, p. 63, in the "Explanatory Notes" chapter). The first occurrence (FO) of *G. ruber* (pink) (0.9 Ma) is recognized between Samples 202-1240A-5H-CC and 6H-CC (47.22–59.73 mcd).

The boundary between upper Pleistocene Subzone Pt1b and the lower Pleistocene Subzone Pt1a is marked by the LO of *Globorotalia tosaensis* (0.65 Ma; Zone Pl5), which can be placed between Samples 202-1240A-5H-CC and 6H-CC (47.22–59.73 mcd). The LO of *Globigerinoides obliquus* (1.77 Ma), which can be identified between Samples 202-1240A-13H-CC and 14H-CC (130.80–140.60 mcd), indicates Subzone Pt1a.

The Pliocene/Pleistocene boundary could not be recognized because of the absence of the standard zonal markers. However, the LO of *Globorotalia exilis* (2.15 Ma), between Samples 202-1240A-19H-CC and 20H-CC (195.24–205.92 mcd), indicates upper Pliocene Zone Pl6, and the LO of *Globorotalia pseudomiocenica* (2.30 Ma), between Samples 22H-CC and 23H-CC (224.97–235.31 mcd), marks the base of this zone. The LO of *Globorotalia limbata* (2.38 Ma), between Samples 202-1240A-22H-CC and 23H-CC (224.97–235.31 mcd), and the LOs of *Glorotalia puncticulata* (2.40 Ma) and of *Globorotalia pertenuis* (2.60 Ma), identified between Samples 23H-CC and 24H-CC (235.31–245.88 mcd), all provide useful markers for upper Pliocene Zone Pl5.

Sample 202-1240A-28H-CC (282.84 mcd), at the base of Hole 1240A, contains only a sparse planktonic foraminiferal assemblage, which does not include any age diagnostic index species. However, the presence of *S. dehiscens* in Sample 202-1240A-27H-CC (278.67 mcd) indicates an age no older than 3.25 Ma for this sample.

Benthic Foraminifers

Benthic foraminifers are generally rare in Hole 1240A samples, and the percentage of benthic foraminifers relative to total foraminifers is consistently low (~1%), except for Samples 202-1240A-17H-CC (174.04 mcd), 19H-CC (195.24 mcd), and 20H-CC (205.92 mcd), where benthic foraminifers represent 3%–10% of the total foraminiferal assemblage (Table T12). Benthic foraminifers, overall, show better preservation than planktonic foraminifers and are only rarely fragmented as a result of dissolution.

T12. Distribution of planktonic foraminifers, p. 72.

The Pleistocene–late Pliocene assemblage is characterized by *Chilostomella ovoidea, Eggerella bradyi, Ehrenbergina serrata, Eubulimina exilis, Globocassidulina subglobosa, Globobulimina affinis, Globobulimina pyrula, Gyroidinoides soldanii, Laticarinina pauperata, Melonis pompilioides, Oridorsalis umbonatus, Planulina wuellerstorfi, Plectofrondicularia vaughani, Pullenia bulloides, Pyrgo murrhina, Pyrgo serrata,* and *Uvigerina peregrina*. Preliminary shipboard study of core catcher samples suggests that the proportion of *Bolivina, Bulimina, Globobulimina,* and *Uvigerina,* which represent useful indicators of high carbon fluxes at the seafloor, vary significantly downhole. However, it was not possible to quantify such changes or to evaluate to what extent the changes may be related to variations in upwelling intensity and/or circulation patterns or merely reflect a preservation bias (e.g., change in benthic foraminiferal accumulation rate).

Diatoms

All core catcher samples from Hole 1240A, as well as smear slides from some additional layers of the split cores, were analyzed.

Diatoms are generally few to abundant, but abundance decreases and preservation deteriorates between 120 and 170 mcd (Table T13; Fig. F22). Diatom assemblages are either dominated by *Thalassiothrix* and *Thalassionema* spp. or *Azpetia nodulifer,* and *Thalassiothrix* oozes were observed at the following levels: intervals 202-1240A-15H-2, 12–100 cm (143.6–144.5 mcd); 15H-2, 135 cm (144.8 mcd); 15H-2, 139 cm (144.9 mcd); 18H-CC (184.5 mcd); and 19H-CC (190.6 mcd).

T13. Distribution of diatoms, p. 73.

Diatoms recovered from Site 1240 span a continuous stratigraphic interval from the Holocene *Fragilariopsis doliolus* Zone to the *Nitzschia marina* Zone (Table T10). The absence of *Nitzschia jouseae* at the bottom of the hole (Sample 202-1240-28H-CC; 282.8 mcd) indicates an age <2.77 Ma (LO age for this species).

Late Miocene diatoms are observed in trace abundances in most of the studied samples, and the presence of the marker species *Thalassiosira miocenica* and *Nitzschia miocenica* indicates reworking from a 6.55- to 6.08-Ma formation.

Two mid-Pleistocene diatom datums were identified; the LO of *Nitzschia reinholdii* (0.62 Ma) is placed between Samples 202-1240A-4H-CC and 5H-CC (36.4–47.2 mcd), and the LO of *Nitzschia fossilis* (0.70 Ma) between Samples 7H-4, 75 cm, and 7H-5, 75 cm (73.7–65.2 mcd).

The following early Pleistocene diatom datums were recognized: the LO of *Rhizosolenia matuyamai* (1.05 Ma) between Samples 202-1240A-9H-4, 75 cm, and 9H-5, 75 cm (84.4–85.9 mcd); the FO of *R. matuyamai* (1.18 Ma) between Samples 11H-2, 75 cm, and 11H-3, 75 cm (101.3–102.8 mcd); the LO of *Rhizosolenia praebergonii* var. *robusta* (1.73 Ma) between Samples 14H-CC and 15H-1, 10 cm (140.6–142.1 mcd). The presence of *F. doliolus* within samples at depths above 194 mcd places its FO

(2.00 Ma) between Samples 202-1240A-19H-6, 75 cm, and 1240A-19H-7, 40 cm (193.6–194.8 mcd). Of the late Pliocene diatom datums, only the LO of *Thalassiosira convexa* s.l. (2.41 Ma) could be recognized between Samples 202-1240A-22H-4, 75 cm, and 22H-5, 75 cm (220.2–221.7 mcd).

PALEOMAGNETISM

Natural Remanent Magnetization

The natural remanent magnetization (NRM) of the archive half of each core section was initially measured then remeasured after alternating-field (AF) demagnetization at selected levels. Cores 202-1240A-1H through 14H were AF demagnetized at 10 and 20 mT. Additionally, Section 202-1240A-1H-1 was demagnetized at 15 mT and Section 2H-3 was demagnetized at 25 mT. Cores 202-1240A-15H through 28H and all cores from Holes 1240B, 1240C, and 1240D were demagnetized at 20 mT. Sections obviously affected by drilling disturbance were not measured.

The NRM intensity before and after demagnetization shows the same general downhole trend with ~1 order of magnitude less intensity after 20-mT AF demagnetization than before (Fig. **F23**). NRM intensities after AF demagnetization are in the 10^{-3} to 10^{-4} A/m range throughout the section. Intensities oscillate downhole, but no downhole trend is observed in contrast to other Leg 202 sites. The overall pattern of NRM intensity is similar to that observed from magnetic susceptibility.

Steep positive inclinations observed prior to demagnetization are due to a drill string magnetic overprint partially, but incompletely, removed after 20-mT AF demagnetization. The inclination values after demagnetization have a positive bias, with steeper (higher) positive values below 70 mcd (Fig. **F24**). Biostratigraphic datums (see **"Biostratigraphy,"** p. 10) indicate that this depth corresponds to the approximate position of where the Brunhes/Matuyama boundary should occur; therefore, the steeper positive inclinations could in some way be related to the overprint on top of an interval with reversed magnetization or low intensity (Fig. **F23**). Because of the equatorial location of Site 1240 and its current ~20° inclination, only small deviations in inclination are expected even from polarity changes.

Because the inclination of the Earth's magnetic field is on average ~0° at the equator (Site 1240 latitude), declination shifts of 180° provide the only means of ascertaining if polarity has reversed. The declinations within individual cores at Site 1240 are generally consistent (show similar directions) when the drill string overprint has been mostly removed. But, when a significant high-inclination drill string overprint remains after AF demagnetization, the declinations become more random in orientation (Fig. **F25**). Intervals with more randomly oriented declinations are usually associated with lower NRM intensities.

To evaluate the polarity stratigraphy at Site 1240, we have used the Tensor tool to provide azimuthal orientation to the declination data. The Tensor tool was employed for Cores 202-1240A-4H through 28H, 202-1240B-3H through 26H, and 202-1240C-3H through 8H and was used to reorient the declination for each hole (Fig. **F26**). Oriented declinations near zero are considered to represent normal polarity and those ~180° represent reversed polarity. Based on declination data, the following polarity intervals can be identified by correlation to the geomag-

F23. NRM intensity before and after AF demagnetization, p. 48.

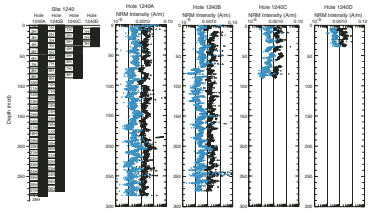

F24. NRM inclinations after demagnetization, p. 49.

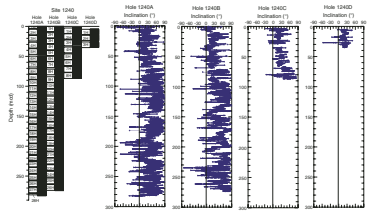

F25. NRM declinations after demagnetization, p. 50.

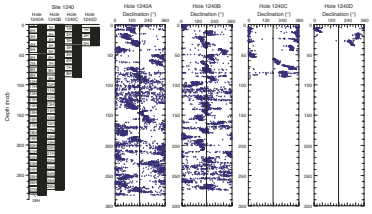

F26. Tensor-corrected declinations after demagnetization, p. 51.

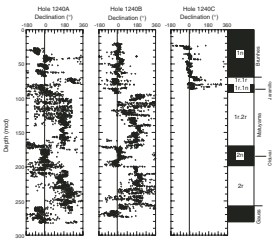

netic polarity timescale (Cande and Kent 1995): Brunhes (1n) Chron, the Jaramillo (1r.1n) and Olduvai (2n) normal polarity subchrons of the Matuyama Chron, and the upper part of the Gauss (2An.1n) Chron. However, most reversal boundaries are not well defined (because of intervals of fluctuating polarity) or are present in core breaks (Fig. F26; Table T14). For example, the Brunhes/Matuyama boundary is not observed in Holes 1240A or 1240B but may be preserved in Core 202-1240C-7H, where a 110° shift in declination is observed. This is complicated because the polarity of sediment below can only be identified as reversed in Core 202-1240A-8H. The Jaramillo (1r.1n) Subchron is also difficult to resolve. The Olduvai Subchron and the upper and lower Olduvai/Matuyama boundaries are particularly well defined in sediments from both Holes 1240A and 1240B. These data suggest that Site 1240 preserves a good paleomagnetic record (Table T15) and that if postcruise demagnetization and analysis are successful, Site 1240 could prove to be a unique paleomagnetic record for the equator.

T14. Determinations of polarity chron boundaries, p. 75.

T15. Paleomagnetic age control points, p. 76.

GEOCHEMISTRY

Sediment Gases

Concentrations of headspace gases were routinely monitored in Hole 1240A sediments according to shipboard safety and pollution prevention considerations (Fig. F27; Table T16). Methane concentration exceeding laboratory blanks was first detected in a headspace gas sample at 19.5 mcd. Below this depth, methane increased gradually, reaching a maximum of 57 ppmv at 146.5 mcd. Methane concentrations then decreased downhole to concentrations <10 ppmv. Low ethane concentrations were detected, and no higher molecular weight hydrocarbons were observed. The reduction of dissolved sulfate in the depth range where methane increased indicates that these small amounts of methane probably originate from in situ fermentation (methanogenesis) of organic matter. The presence of interstitial sulfate inhibits methanogenesis in marine sediments (Claypool and Kvenvolden, 1983).

F27. Headspace methane concentrations, p. 52.

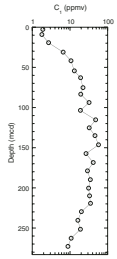

T16. Headspace gases concentrations and C_1/C_2 ratios, p. 77.

T17. Interstitial water geochemical data, p. 78.

Interstitial Water Geochemistry

We collected 28 interstitial water samples from Hole 1240A sediments for shipboard analyses. We collected an additional 44 interstitial water samples at a frequency of one per section for the upper 60 mbsf for shore-based analyses. Chemical gradients at this site (Table T17; Fig. F28) reflect the influence of organic matter oxidation by a limited degree of sulfate reduction, the influence of fluid flow of relatively unaltered seawater in the underlying basement, the dissolution of biogenic silica driven by the relatively low thermal gradient that results from the effects of this fluid flow on conductive heat flow, and the effects of authigenic calcite precipitation. Subunit IB (see "Description of Lithologic Unit," p. 5, in "Lithostratigraphy") is relatively rich in organic carbon and is the focus of the organic carbon oxidation reactions and the resulting signatures in the interstitial water chemistry.

Chlorinity increases from 551 mM at 1.5 mcd to >560 mM by 31.1 mcd then persists at these values throughout until a decline in the deepest sample toward a value similar to seawater (Fig. F28). Salinity, measured refractively as total dissolved solids, is 35 throughout (Table T18). Sodium concentrations measured by inductively coupled plasma–

F28. Interstitial water geochemical data, p. 53.

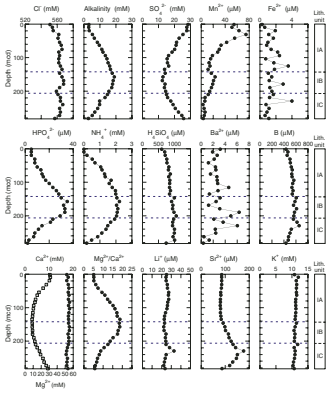

T18. IC, $CaCO_3$, TC, TOC, TOC CFB, TN, and TOC/TN ratios, p. 79.

atomic emission spectrophotometry averaged 1.5% lower than those estimated by charge balance reported here (Table T19). Sodium concentrations parallel chlorinity, with a total range from 472 to 489 mM.

Organic matter diagenesis, driven by microbially mediated oxidation reactions, influences the interstitial water chemistry. Sulfate decreases from 28.5 mM at 1.5 mcd to a broad minimum of <15 mM from 135.1 to 200.4 mcd, coincident with the organic carbon–rich interval of Subunit IB (see "Description of Lithologic Unit," p. 5, in "Lithostratigraphy"). Sulfate increases to 25.7 mM at 282.0 mcd. The alkalinity profile is the inverse of sulfate, with alkalinity increasing from 3.1 mM at 1.5 mcd to a maximum >17 mM from 146.5 to 189.8 mcd, within Subunit IB. Alkalinity then declines to 2.8 mM at 282.0 mcd. Alkalinity is generated by sulfate reduction and consumed partially by authigenic mineral precipitation within the sediments.

The return of sulfate and alkalinity concentrations toward seawater values near the sediment/basalt interface, along with that of other elements, indicates flow of relatively unaltered seawater in the underlying basement. Large-scale horizontal advection of such waters through oceanic crust in the central equatorial Pacific has been inferred from interstitial water geochemistry and is thought responsible for the low conductive heat flow (i.e., low thermal gradients) observed in that region (Baker et al., 1991; Oyun et al., 1995).

Dissolved manganese concentrations increase from 55 µM at 1.5 mcd to a maximum of 75 µM at 31.1 mcd, indicating the importance of suboxic diagenesis of organic matter in this depth zone. Manganese generally declines downcore, with a rapid decrease in Subunit IA to a small, secondary maximum in Subunit IB to >20 µM from 157.5 to 168.5 mcd, followed by a decline to 3 µM at 282.0 mcd. Dissolved iron is present at relatively low concentrations, presumably reflecting a limited supply of reducible iron minerals.

Phosphate concentrations increase to a maximum in Subunit IB, from 5 µM at 1.5 mcd to ≥30 µM from 146.5 to 189.8 mcd, then decline to 2 µM at 282.0 mcd. Ammonium concentrations increase from below the detection limit (0.15 mM) at 1.5 mcd to a maximum >2 mM from 146.5 to 200.4 mcd then decline to 0.17 mM (just above the detection limit) at 282.0 mcd. The increases in phosphate and ammonium result from the oxidation of organic matter, whereas the decreases with depth below Subunit IB indicate the influence of seawater flow in the underlying oceanic crust.

Dissolved silicate increases from 601 µM at 1.5 mcd to ~1000 µM by 273.0 mcd then declines in the deepest sample. Site 1240 has a significantly lower thermal gradient (~2.56°C/100 m) than Site 1238 (~12.7°C/100 m) or Site 1239 (~8.8°C/100 m). The silicate increase with depth for Site 1240 is also much less steep than those observed at Sites 1238 and 1239, and Site 1240 never reaches temperatures high enough to produce silicate concentrations >1800 µM as seen at depth in Sites 1238 and 1239.

Barium concentrations are low (<7 µM) throughout, indicating that sulfate concentrations are sufficient to prevent significant dissolution of barite. Boron concentrations are close to seawater values in the shallowest and deepest samples (436 µM at 1.5 mcd and 433 µM at 282.0 mcd, respectively), with a middepth maximum to 600 µM or greater.

Calcium decreases from 10.3 mM at 1.5 mcd to a minimum of <3.5 mM from 103.5 to 178.9 mcd. This calcium minimum is present at a shallower depth than the alkalinity maximum. Calcium increases to 9.5 mM at 282.0 mcd. The shallow part of this profile is controlled by au-

T19. Results of Rock-Eval pyrolysis analyses, p. 81.

thigenic calcite precipitation driven by the alkalinity increase, and the deeper portion reflects the influence of seawater advection in the underlying oceanic crust. Magnesium concentrations average ~54 mM, with little variation with depth. Magnesium/calcium ratios increase from 5.1 at 1.5 mcd to >17 from 125.3 to 189.8 mcd then decrease to 5.7 at 282.0 mcd (Fig. F28). The increase in magnesium/calcium in the shallower sediments, driven by the decrease in calcium, indicates that calcite precipitation is the dominant authigenic mineralization reaction, consuming calcium and alkalinity. Despite the resulting high magnesium/calcium ratios, the formation of dolomite is apparently inhibited by the presence of sulfate in interstitial water throughout Site 1240.

Lithium concentrations show little variation with depth, with the exception of a small maximum in Subunit IC to 33 µM at 229.8 mcd. Strontium concentrations are close to seawater values in the shallowest and deepest samples and increase in Subunit IB from 91 µM at 146.5 mcd to a maximum in Subunit IC of 177 µM at 229.8 mcd. Potassium concentrations have a small initial increase then have a small overall decline with depth.

Sedimentary Inorganic Carbon, Organic Carbon, Nitrogen, and Sulfur Concentrations

Inorganic carbon (IC), total carbon (TC), total nitrogen (TN), and total sulfur (TS) concentrations were determined on sediment samples from Hole 1240A (Table T18). Organic matter carbon/nitrogen ratios and Rock-Eval pyrolysis were employed to characterize the organic matter.

Calcium carbonate concentrations range between 22.8 and 80.3 wt% (average = 56.0 wt%) (Table T18; Fig. F29). Carbonate concentrations decrease from ~60 to ~40 wt% in the uppermost 10.1 m and increase to a maximum of 80.3 wt% between 10.1 and 44.1 mcd. Calcium carbonate concentrations reach a minimum from 137.4 to 206.2 mcd, with values typically <50 wt% and as low as 22.8 wt% at 175.2 mcd. Below 206.2 mcd, carbonate contents increase abruptly to >35 wt% with large-amplitude variations at depth.

TOC concentrations range between 0.2 and 3.1 wt% (average = 1.0 wt%) (Table T18; Fig. F29). In the uppermost 140 m, TOC concentrations range between 0.3 and 1.5 wt%, with the highest concentrations in the upper ~35 m. TOC concentrations are >1 wt% and up to 3.1 wt% (average = 2.0 wt%) from 142.7 to 212.3 mcd, with the TOC maximum coincident with the calcium carbonate minimum. At greater depths, TOC contents are generally <1 wt%. Variations in TOC are apparently not driven solely by dilution by calcium carbonate, as variations in TOC on a carbonate-free basis (CFB) are similar to those in TOC (Fig. F29). Higher TOC concentrations are associated with lower calcium carbonate concentrations (Fig. F30).

Variations in TN concentration are similar to those in TOC (Fig. F29). In the uppermost 142.7 mcd, TOC/TN ratios average 4.8, typical of unaltered marine organic matter (Bordovskiy, 1965; Emerson and Hedges, 1988; Meyers, 1997). In the TOC-rich interval from 142.7 to 212.3 mcd, TOC/TN ratios range from ~2 to 9. Below 212.3 mcd, where both TOC and TN contents are low, TOC/TN ratios average 9.0. The interval of high TOC concentrations is unlikely to be the result of enhanced terrigenous organic matter input because high TOC concentrations are associated with lower TOC/TN ratios. The increase in TOC/TN ratios at

F29. $CaCO_3$, TOC, TOC CFB, TN, and TOC/TN, p. 54.

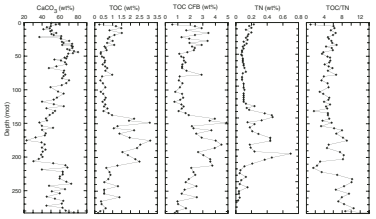

F30. $CaCO_3$ vs. TOC and TN vs. TOC, p. 55.

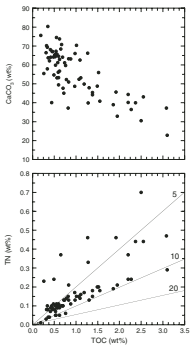

depths >212.3 mcd may be the result of preferential loss of nitrogen relative to carbon during organic matter diagenesis (Meyers, 1997).

Nine samples were selected for Rock-Eval pyrolysis from the depth interval of the TOC maximum. Low T_{max} values indicate that the organic matter is thermally immature (Table T19). The relationship between S_2 and TOC concentrations indicates Type II organic matter (Fig. F31) (i.e., marine algal organic matter) (Tissot and Welte, 1984; Langford and Blanc-Valleron, 1990). This is consistent with the interpretation that the supply of terrigenous organic matter has played only a minor role at this site.

Fresh marine plankton has a relatively high lipid content, thus high H/C ratios. Therefore, well-preserved organic matter of marine algal origin (Type II) yields high hydrogen index (HI) values when subjected to pyrolysis. The HI values vary between 254 and 379 (average = 352) (Table T19; Fig. F31). These values are typical for high-productivity areas (e.g., upwelling) associated with a high organic carbon flux and rapid burial (Whelan et al., 1990). High sedimentation rates mark the interval of high TOC concentrations (~143–212 mcd) and may have favored the preservation of the organic material (see "Biostratigraphy," p. 10, and "Age Model and Mass Accumulation Rates" p. 17). The presence of diatom oozes during this Pliocene–Pleistocene interval supports a hypothesis of enhanced productivity for this interval (see "Lithostratigraphy," p. 5, and "Diatoms," p. 12, in "Biostratigraphy").

F31. S_2 vs. TOC and HI vs. TOC, p. 56.

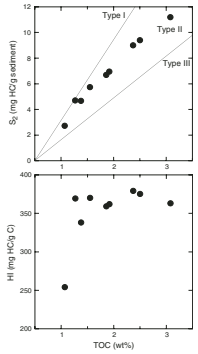

AGE MODEL AND MASS ACCUMULATION RATES

A 282.9-mcd-thick (253.0 mbsf) sequence of Pliocene (~2.8 Ma) to Holocene pelagic sediments was recovered at Site 1240. Biostratigraphic and magnetostratigraphic datums (see Tables T10, T15) were used to construct an age-depth model for this site (Table T20; Fig. F32). Linear sedimentation rates (LSRs), total MARs, and carbonate MARs were calculated at 0.4-m.y. intervals (see "Age Models and Mass Accumulation Rates," p. 41, in the "Explanatory Notes" chapter).

T20. Age-depth model, LSR, and MAR, p. 82.

F32. Shipboard biostratigraphic and magnetostratigraphic datums and age-depth model, p. 57.

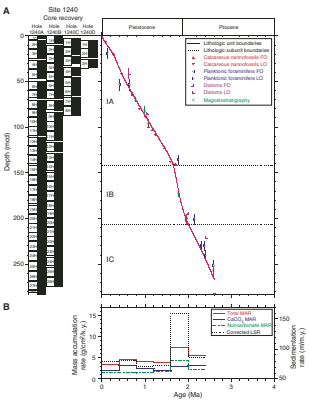

Age-Depth Model

The definition of the age model at high-sedimentation-rate Site 1240 relied primarily upon magnetostratigraphic and calcareous nannofossil datums (Fig. F32). Microfossil reworking was evident in the upper Pliocene section (see "Biostratigraphy," p. 10), and two magnetic reversal boundaries (~70–100 mcd) were poorly defined (see "Paleomagnetism," p. 13). Two inflections in the age-depth profile are reasonably well defined, however, at ~140 and ~200 mcd. These inflections correspond very well to lithologic subunit boundaries (Subunit IB; see "Lithostratigraphy," p. 5).

Linear Sedimentation and Mass Accumulation Rates

LSRs range between ~72 and 160 m/m.y., and total MARs range between 1.6 and 8.5 g/cm²/k.y. The LSRs vary slightly around values of 70–100 m/m.y., except for a peak (160 m/m.y.) between 2.0 and 1.6 Ma. MAR values have a similar pattern but are more differentiated as a result of the dry density variations. The main MAR peaks at 2.0–1.6 Ma are not as pronounced as the LSR peak because this interval (lithologic Subunit IB; 142.2-206.4 mcd) has high diatom and organic carbon concen-

trations (see "Lithostratigraphy," p. 5, "Biostratigraphy," p. 10, and "Geochemistry," p. 14), which maintain high porosity and lower the grain density. The youngest interval (0.4–0 Ma) also has LSR values proportionally higher than the low MAR values. Again, the low MAR values in this interval result from lowered dry densities, probably related to both increased biogenic opal contents and reduced overburden toward the top of the sediment sequence.

Total MARs at Site 1240 are controlled by the combined variations in calcareous and siliceous microfossil accumulation. Diatom productivity dominated at 2.4–1.6 Ma and after 0.4 Ma, whereas calcareous productivity dominated at all other times.

REFERENCES

Andreasen, D.J., and Ravelo, A.C., 1997. Tropical Pacific Ocean thermocline depth reconstructions for the last glacial maximum. *Paleoceanography,* 12:395–413.

Baker, P.A., Stout, P.M., Kastner, M., and Elderfield, H., 1991. Large-scale lateral advection of seawater through oceanic crust in the central equatorial Pacific. *Earth Planet. Sci. Lett.,* 105:522–533.

Beaufort, L., Garidel-Thoron, T., Mix, A.C., and Pisias, N.G., 2001. ENSO-like forcing on oceanic primary production during the late Pleistocene. *Science,* 293:2440–2444.

Behrenfeld, M.J., Randerson, J.T., McClain, C.R., Feldman, G.C., Los, S.O., Tucker, C.J., Falkowski, P.G., Field, C.B., Frouin, R., Esaias, W.E., Kolber, D.D., and Pollack, N.H., 2001. Biospheric primary production during and ENSO transition. *Science,* 291:2594–2597.

Berggren, W.A., Kent, D.V., Swisher, C.C., III, and Aubry, M.-P., 1995. A revised Cenozoic geochronology and chronostratigraphy. *In* Berggren, W.A., Kent, D.V., Aubry, M.-P., and Hardenbol, J. (Eds.), *Geochronology, Time Scales and Global Stratigraphic Correlation*. Spec. Publ.—SEPM, 54:129–212.

Bordovskiy, O.K., 1965. Accumulation and transformation of organic substances in marine sediment, 2. Sources of organic matter in marine basins. *Mar. Geol.,* 3:5–31.

Cadet, J.-P., Pouclet, A., Thisse, Y., Bardintzeff, J.M., and Azéma, J., 1982. Middle America Neogene explosive volcanism and ash layers: evidence from the Middle America Trench transect, Deep Sea Drilling Project Leg 167. *In* Aubouin, J., von Huene, R., et al., *Init. Repts. DSDP,* 67: Washington (U.S. Govt. Printing Office), 475–491.

Cande, S.C., and Kent, D.V., 1995. Revised calibration of the geomagnetic polarity timescale for the Late Cretaceous and Cenozoic. *J. Geophys. Res.,* 100:6093–6095.

Cane, M.A., 1986. El Niño. *Annu. Rev. Earth Planet. Sci.,* 14:43–70.

Claypool, G.E., and Kvenvolden, K.A., 1983. Methane and other hydrocarbon gases in marine sediment. *Annu. Rev. Earth Planet. Sci.,* 11:299–327.

Dunbar, G.B., 2001. A detailed characterization of Dansgaard–Oeschger cycles at Site 1063 (Bermuda Rise). *In* Keigwin, L.D., Rio, D., Acton, G.D., and Arnold, E. (Eds.), *Proc. ODP, Sci. Results,* 172, 1–24 [CD-ROM]. Available from: Ocean Drilling Program, Texas A&M University, College Station TX 77845-9547, USA.

Emerson, S., and Hedges, J.I., 1988. Processes controlling the organic carbon content of open ocean sediments. *Paleoceanography,* 3:621–634.

Farrell, J.W., Murray, D.W., McKenna, V.S., and Ravelo, A.C., 1995. Upper ocean temperature and nutrient contrasts inferred from Pleistocene planktonic foraminifer $\delta^{18}O$ and $\delta^{13}C$ in the eastern equatorial Pacific. *In* Pisias, N.G., Mayer, L.A., Janecek, T.R., Palmer-Julson, A., and van Andel, T.H. (Eds.), *Proc. ODP, Sci. Results,* 138: College Station, TX (Ocean Drilling Program), 289–319.

Hamilton, E.L., and Bachman, R.T., 1982. Sound velocity and related properties of marine sediments. *J. Acoust. Soc. Am.,* 72:1891–1904.

Hey, R., Johnson, G.L., and Lowrie, A., 1977. Recent plate motions in the Galapagos area. *Geol. Soc. Am. Bull.,* 88:1385–1403.

Hovan, S.A., 1995. Late Cenozoic atmospheric circulation intensity and climatic history recorded by eolian deposition in the eastern equatorial Pacific Ocean, Leg 138. *In* Pisias, N.G., Mayer, L.A., Janecek, T.R., Palmer-Julson, A., and van Andel, T.H. (Eds.), *Proc. ODP, Sci. Results,* 138: College Station, TX (Ocean Drilling Program), 615–625.

Kroopnick, P., 1974. The dissolved O_2-CO_2-^{13}C system in the eastern equatorial Pacific. *Deep-Sea Res. Part A,* 21:211–227.

Langford, F.F., and Blanc-Valleron, M.M., 1990. Interpreting Rock-Eval pyrolysis data using graphs of pyrolizable hydrocarbons vs. total organic carbon. *AAPG Bull.,* 74:799–804.

Lea, D.W., Pak, D.K., and Spero, H.J., 2000. Climate impact of late Quaternary equatorial Pacific sea surface temperature variations. *Science,* 289:1719–1724.

Levitus, S., Conkright, M.E., Reid, J.L., Najjar, R.G., and Mantyla, N.A., 1993. Distribution of nitrate, phosphate, and silicate in the world oceans. *Prog. Oceanogr.,* 31:245–273.

Lonsdale, P., 1976. Abyssal circulation of the southeastern Pacific and some geological implications. *J. Geophys. Res.,* 81:1163–1176.

Lyle, M., Liberty, L., Mix, A., Pisias, N., Goldfinger, C., Hulett, D., and Janik, A., 2000. *Site Survey Data Package 5: Site Surveys for ODP Leg 201 from the NEMO-3 Cruise, in Support of Proposal 465: Southeast Pacific Paleoceanographic Transects*. CGISS Tech. Rpt. 2000-06, Boise State University.

Meyers, P.A., 1997. Organic geochemical proxies of paleoceanographic, paleolimnologic, and paleoclimatic processes. *Org. Geochem.,* 27:213–250.

Mix, A.C., Morey, A.E., Pisias, N.G., and Hostetler, S., 1999. Foraminiferal faunal estimates of paleotemperatures: circumventing the no-analog problems yields cool ice-age tropics. *Paleoceanography,* 14:350–359.

Mix, A.C, Pisias, N.G., Goldfinger, C., Lyle, M., Liberty, L., Janik, A., Hebbeln, D., Wefer, G., and Lamy, F., 2000. *Southeast Pacific Paleoceanographic Transects, Site Survey Data Package 4: NEMO Expedition, Leg III,* R/V Melville, *May–June 2000:* Corvallis (Oregon State Univ.).

Mix, A.C., Pisias, N.G., Rugh, W., Wilson, J., Morey, A., and Hagelberg, T.K., 1995. Benthic foraminifer stable isotope record from Site 849 (0–5 Ma): local and global climate changes. *In* Pisias, N.G., Mayer, L.A., Janecek, T.R., Palmer-Julson, A., and van Andel, T.H. (Eds.), *Proc. ODP, Sci. Results,* 138: College Station, TX (Ocean Drilling Program), 371–412.

Molina-Cruz, A., 1977. The relation of the southern trade winds to upwelling processes during the last 75,000 years. *Quat. Res.,* 8:324–339.

Murray, J.W., Barber, R.T., Roman, M.R., Bacon, M.P., and Feely, R.A., 1994. Physical and biological controls on carbon cycling in the equatorial Pacific. *Science,* 266:58–65.

Ocean Climate Laboratory, 1999. *World Ocean Atlas 1998 (WOA98)* [CD-ROM]. Available from: National Climatic Data Center, Asheville NC 28801-5001, USA.

Oyun, S., Elderfield, H., and Klinkhammer, G.P., 1995. Strontium isotopes in pore waters of east equatorial Pacific sediments: indicators of seawater advection through oceanic crust and sediments. *In* Pisias, N.G., Mayer, L.A., Janecek, T.R., Palmer-Julson, A., and van Andel, T.H. (Eds.), *Proc. ODP, Sci. Results,* 138: College Station, TX (Ocean Drilling Program), 813–819.

Pisias, N.G., Mayer, L.A., and Mix, A.C., 1995. Paleoceanography of the eastern equatorial Pacific during the Neogene: synthesis of Leg 138 drilling results. *In* Pisias, N.G., Mayer, L.A., Janecek, T.R., Palmer-Julson, A., and van Andel, T.H. (Eds.), *Proc. ODP, Sci. Results,* 138: College Station, TX (Ocean Drilling Program), 5–21.

Pisias, N.G., and Mix, A.C., 1997. Spatial and temporal oceanographic variability of the eastern equatorial Pacific during the late Pleistocene: evidence from radiolaria microfossils. *Paleoceanography,* 12:381–393.

Strub, P.T., Mesias, J.M., Montecino, V., Rutllant, J., and Salinas, S., 1998. Coastal ocean circulation off western South America. *In* Robinson, A.R., and Brink, K.H. (Eds.), *The Sea* (Vol. 11): *Coastal Oceans:* New York (Wiley), 273–313.

Tissot, B.P., and Welte, D.H., 1984. *Petroleum Formation and Occurrence* (2nd ed.): Heidelberg (Springer-Verlag).

Weber, M.E., 1998. Estimation of biogenic carbonate and opal by continuous nondestructive measurements in deep-sea sediments: application to the eastern equatorial Pacific. *Deep-Sea Res., Part I,* 45:1955–1975.

Weber, M.E., Hiessen, F., Kuhn, G., and Weidicke, M., 1997. Calibration and application of marine sedimentary physical properties using a multi-sensor core logger. *Mar. Geol.,* 136:151–172.

Whelan, J.K., Kanyo, Z., Tarafa, M., and McCaffrey, M.A., 1990. Organic matter in Peru upwelling sediments—analysis by pyrolysis, pyrolysis-gas chromatography, and pyrolysis-gas chromatography mass spectrometry. *In* Suess, E., von Huene, R., et al., *Proc. ODP, Sci. Results,* 112: College Station, TX (Ocean Drilling Program), 573–590.

Figure F1. Locations of Sites 1238–1242 and regional bathymetry of the Panama Basin, which is bounded to the north by Cocos Ridge, to the south by Carnegie Ridge, and split in midbasin by the Galapagos spreading center.

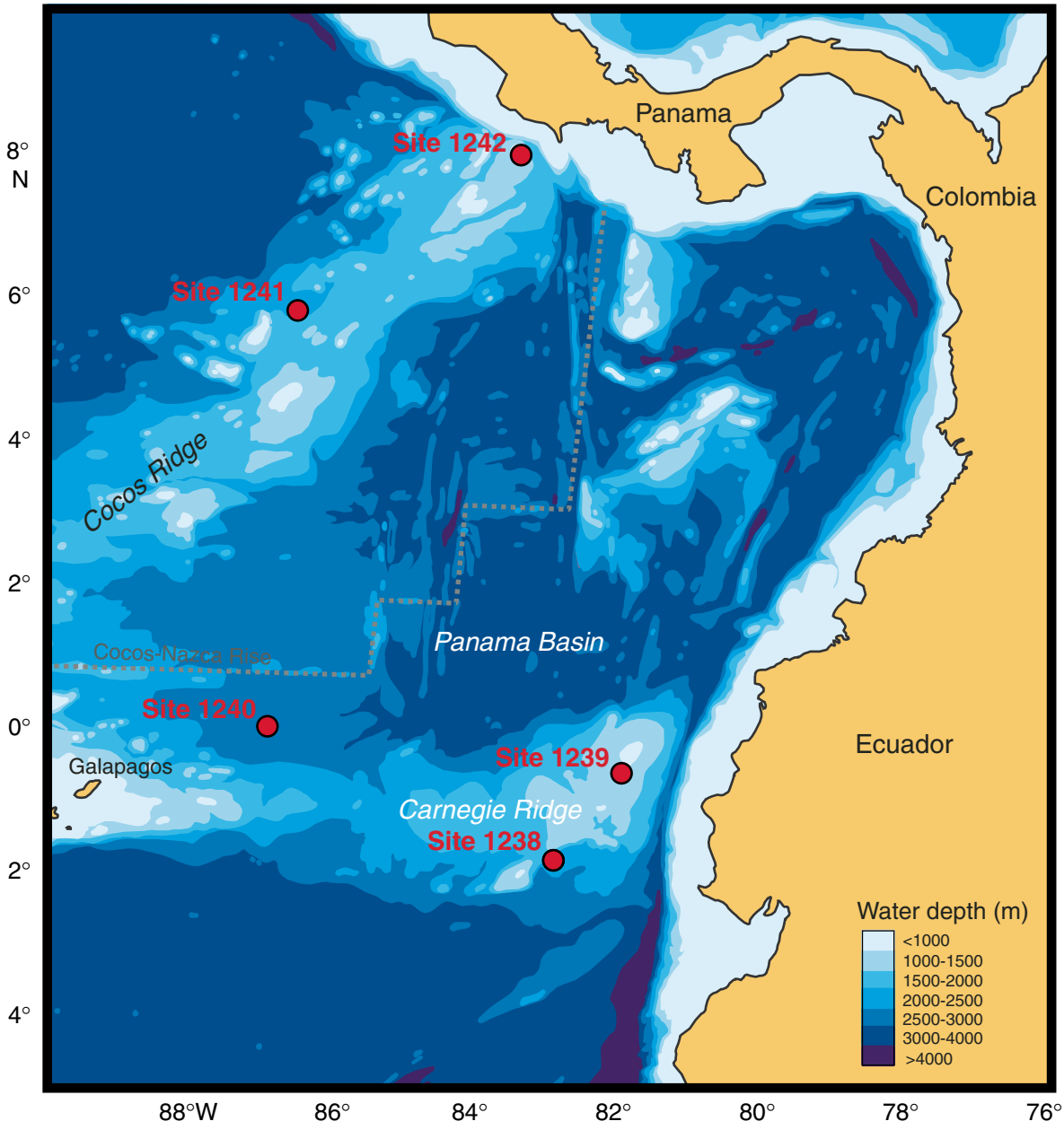

Figure F2. High-resolution swath bathymetry, illustrated in an oblique view (Mix et al., 2000). The abyssal hill topography illustrated here covers an area of ~30 km (north-south) × 30 km (east-west).

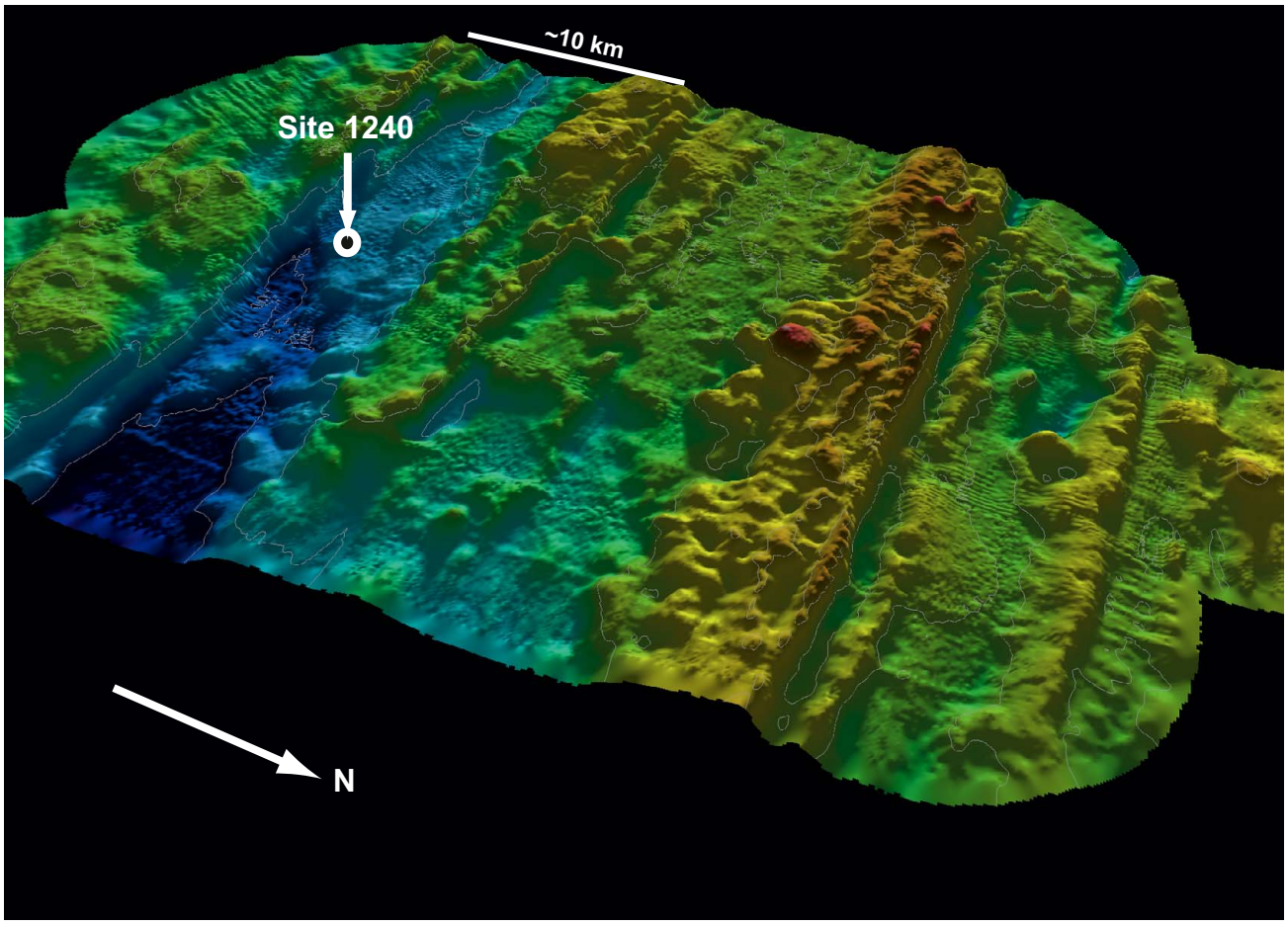

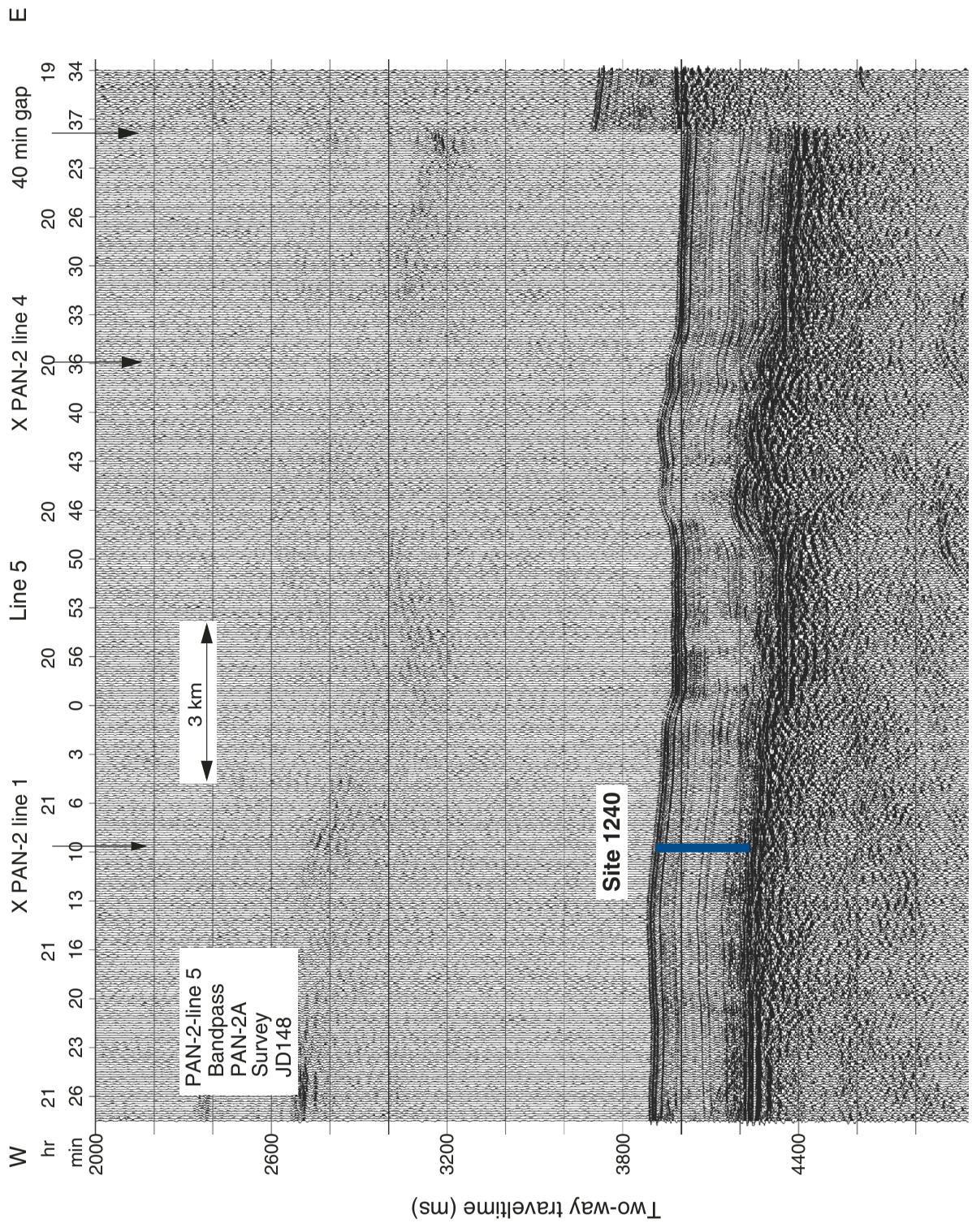

Figure F3. Seismic profile at Site 1240 (*Melville*, NEMO-3, PAN2, line 5, JD148, 27 May 2000; two 150-in^3 generator injector guns; Lyle et al., 2000).

Figure F4. Upper-ocean features of the eastern tropical Pacific (after Strub et al., 1998). SEC = South Equatorial Current, NECC = North Equatorial Countercurrent, EUC = Equatorial Undercurrent, PCC = Peru-Chile Current, PCCC = Peru-Chile Countercurrent, CC = Coastal Current, GUC = Gunther Undercurrent. Modern mean annual sea-surface temperatures (SSTs) (in degrees Celsius, after Ocean Climate Laboratory, 1999).

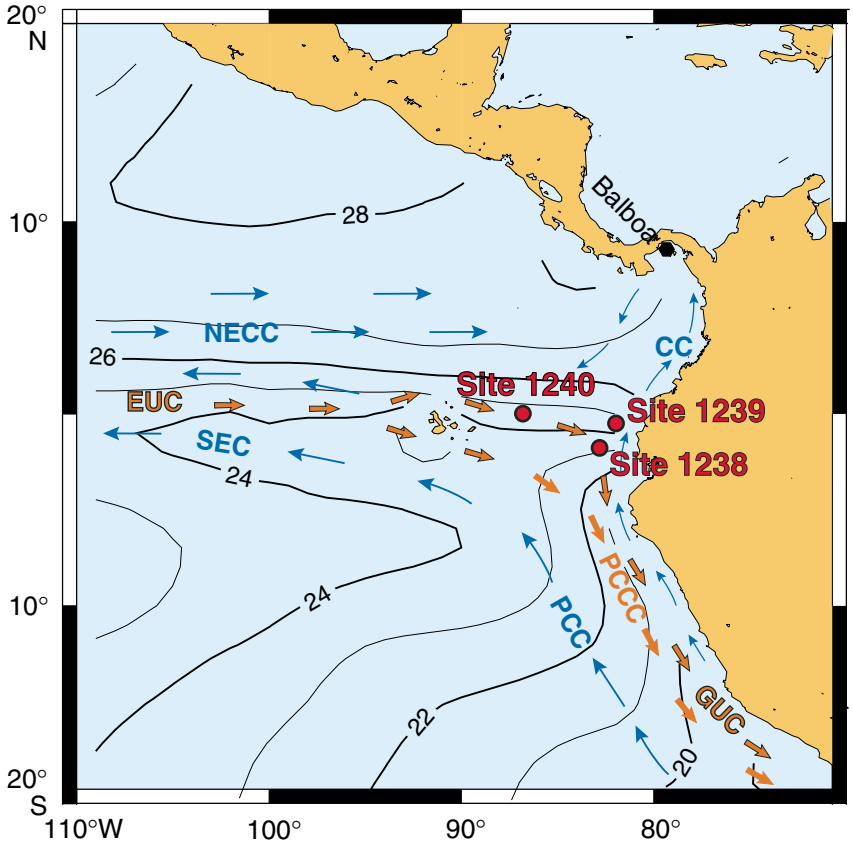

Figure F5. Chlorophyll distributions in surface waters of the equatorial Pacific, based on satellite color data, reveal that Site 1240 is now within the highly productive upwelling system off Ecuador.

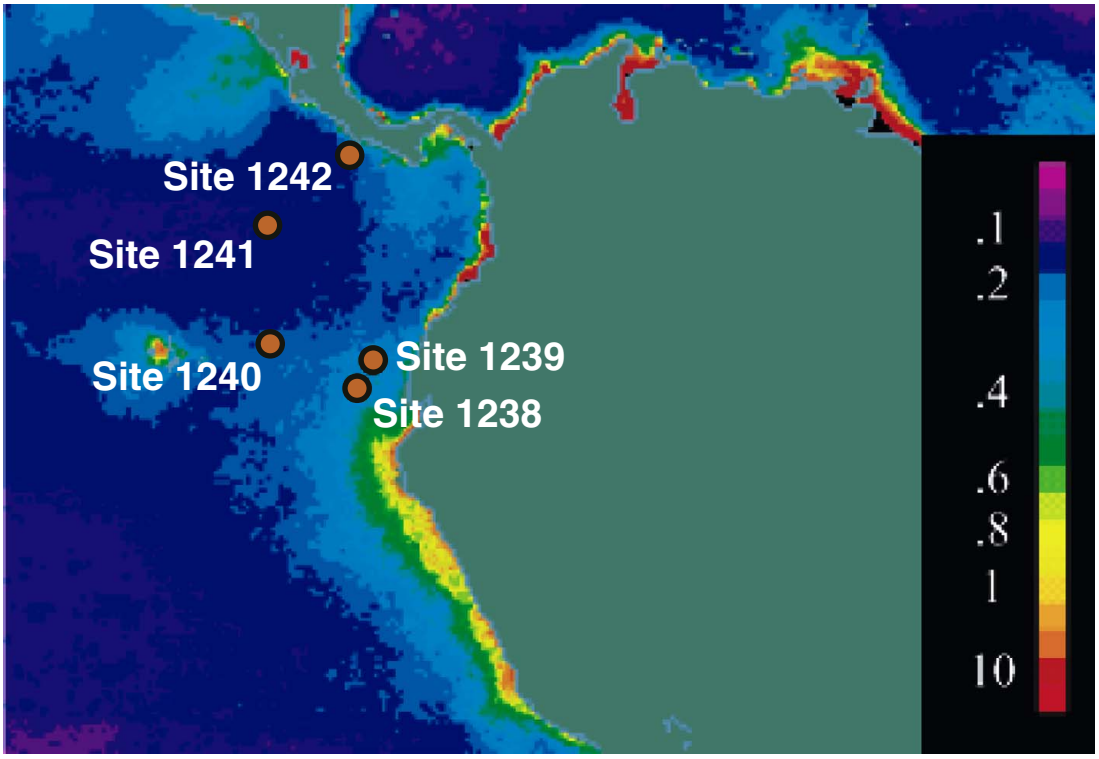

Figure F6. Meridional cross section of water masses, characterized by dissolved oxygen concentrations in the southeast Pacific (Ocean Climate Laboratory, 1999). GUC = Gunther Undercurrent, EUC = Equatorial Undercurrent, NPIW = North Pacific Intermediate Water, PCW = Pacific Central Water, PBW = Peru Basin Water.

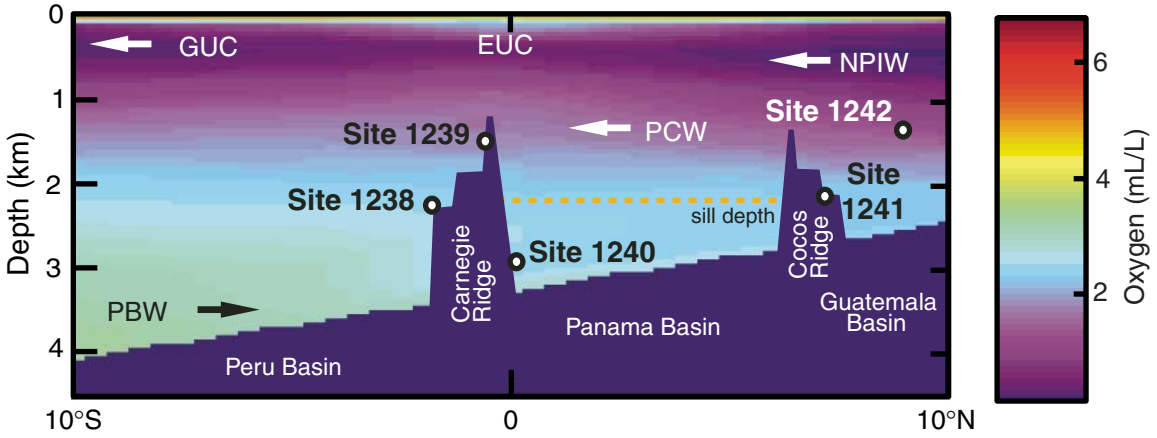

Figure F7. Modern annual-average properties of the upper ocean at paleolocations of Site 1240, based on plate tectonic backtracking and an assumption of no temporal changes in regional oceanic properties. Atlas data on physical and chemical properties are from WOA98 (Ocean Climate Laboratory, 1999). Primary productivity (PP) is from satellite measurements of sea-surface color (Behrenfeld et al., 2001). Pycnocline depth is calculated to the nearest 5 m, based on the shallowest maximum in the vertical density gradient. Symbols are average values extracted from the nearest 1° latitude-longitude box in each atlas. Lines = smoothed trends of each property along the backtrack path. SST = sea-surface temperature, SSS = sea-surface salinity.

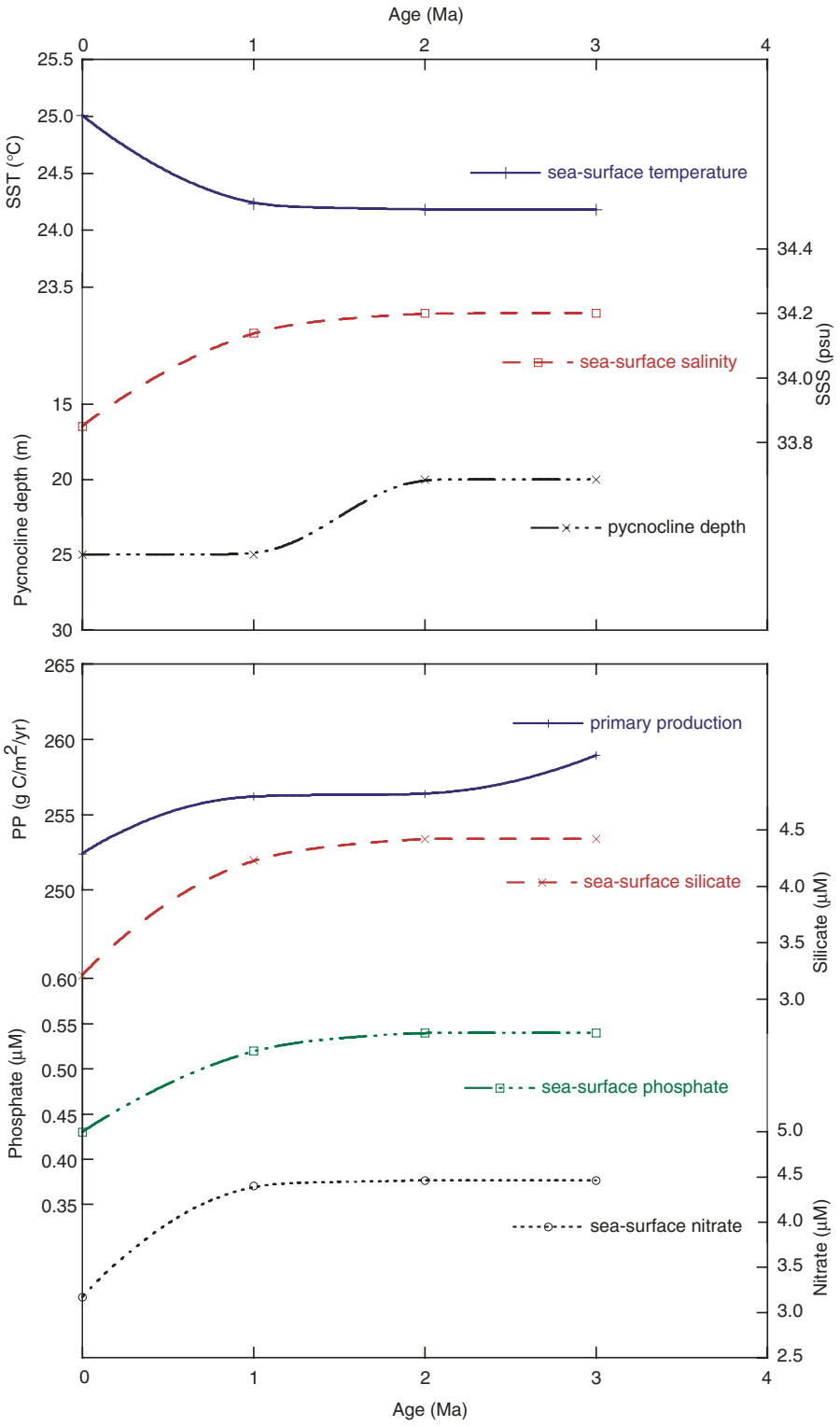

Figure F8. OSU Fast Track magnetic susceptibility data (OSUS-MS) vs. mcd for the spliced record and Holes 1240A (black), 1240B (red), 1240C (green), and 1240D (blue). Gray boxes indicate the portions of cores that are in the splice. **A.** 0–40 mcd. **B.** 30–70 mcd. (Continued on next four pages.)

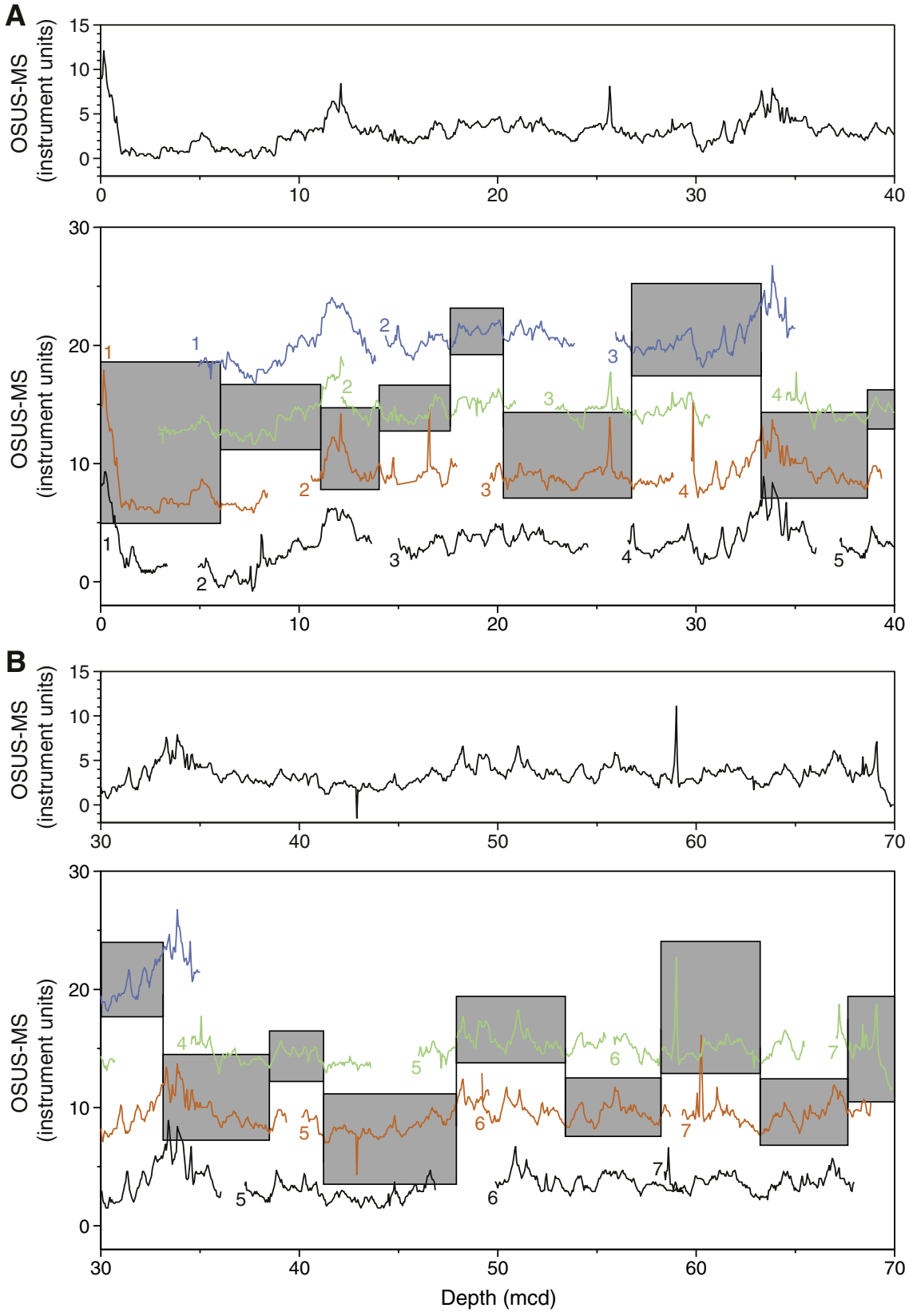

Figure F8 (continued). C. 60–100 mcd. D. 90–130 mcd.

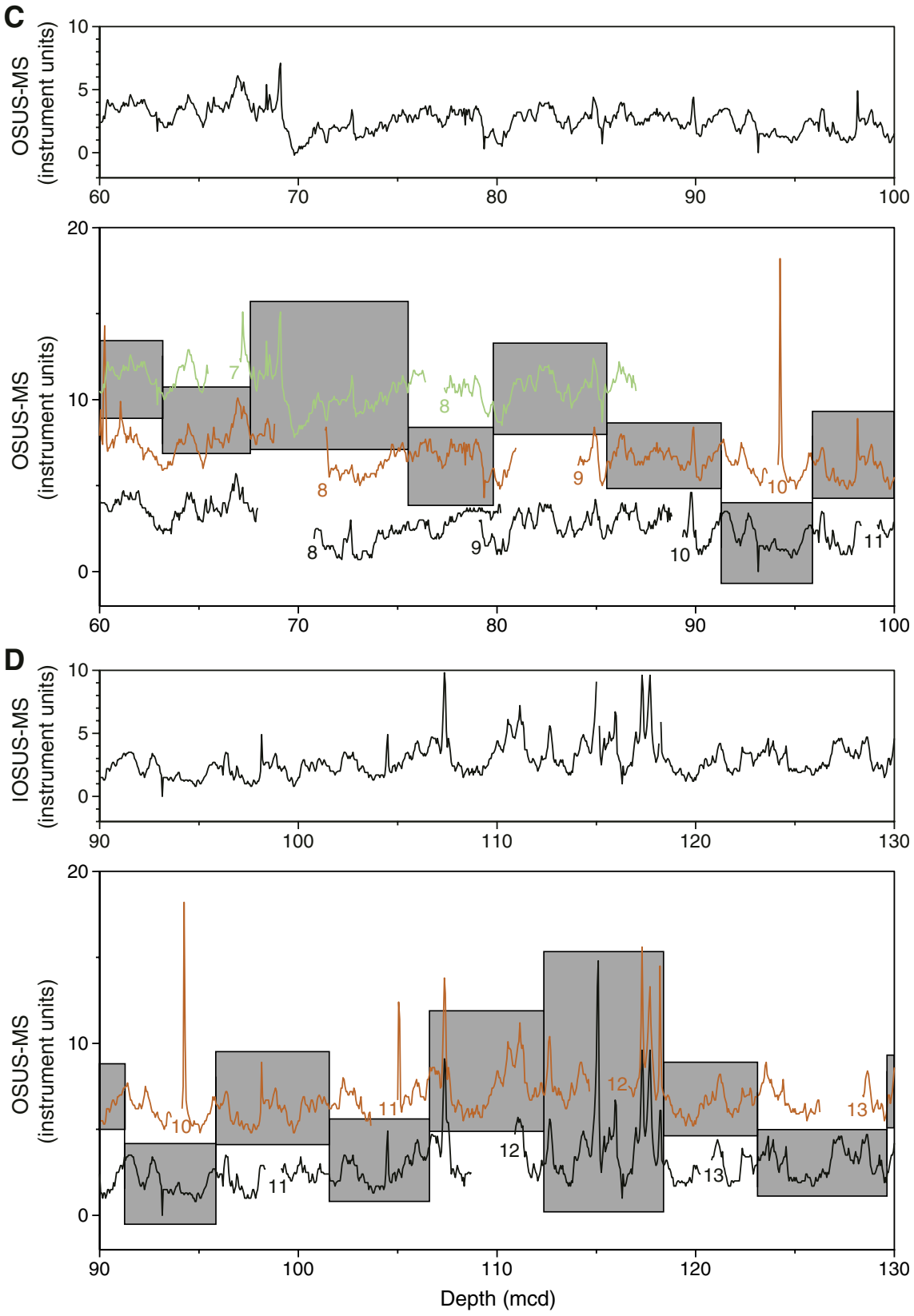

Figure F8 (continued). E. 120–160 mcd. F. 150–190 mcd.

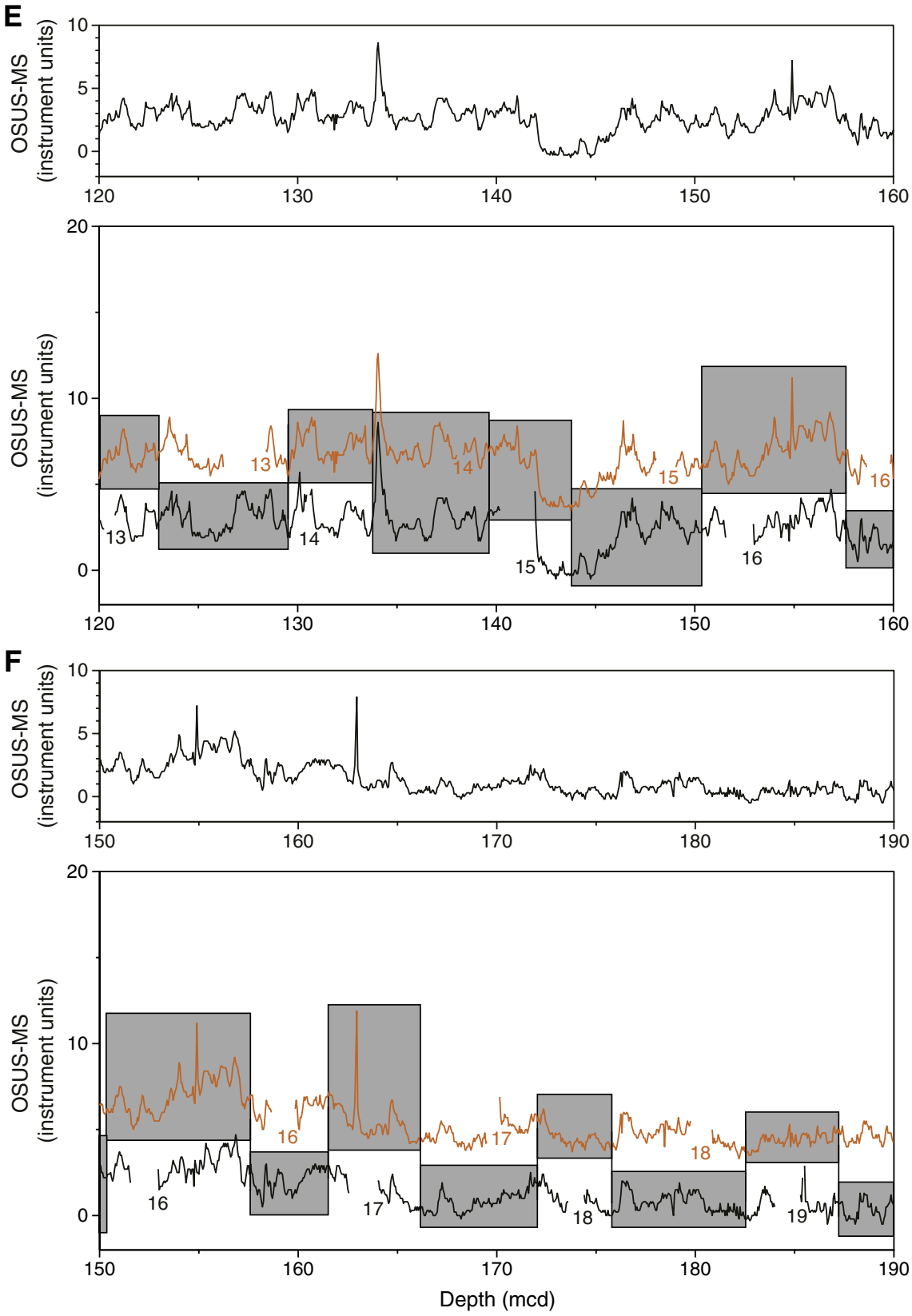

Figure F8 (continued). G. 180–220 mcd. H. 210–250 mcd.

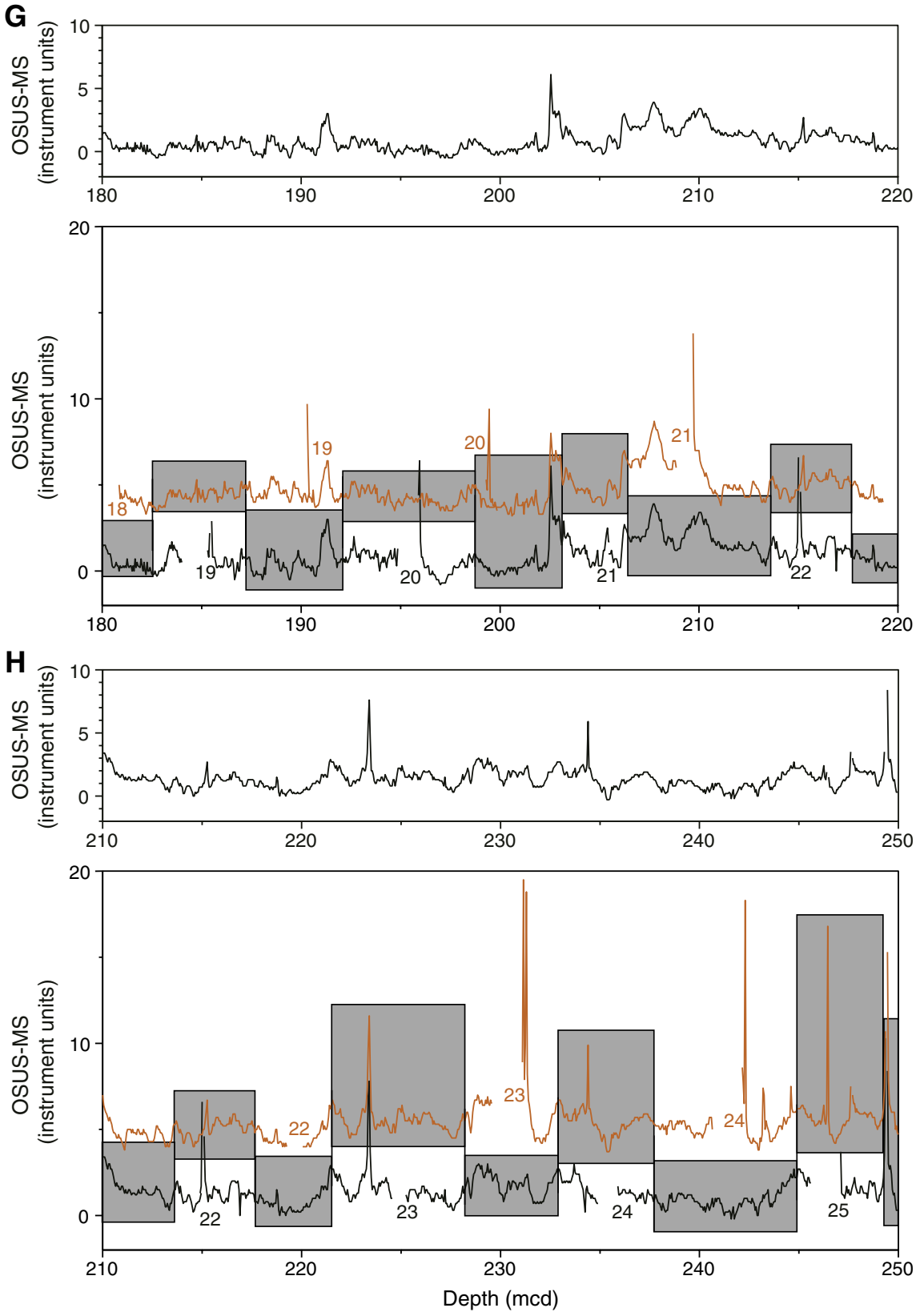

Figure F8 (continued). I. 240–280 mcd. **J.** 270–310 mcd.

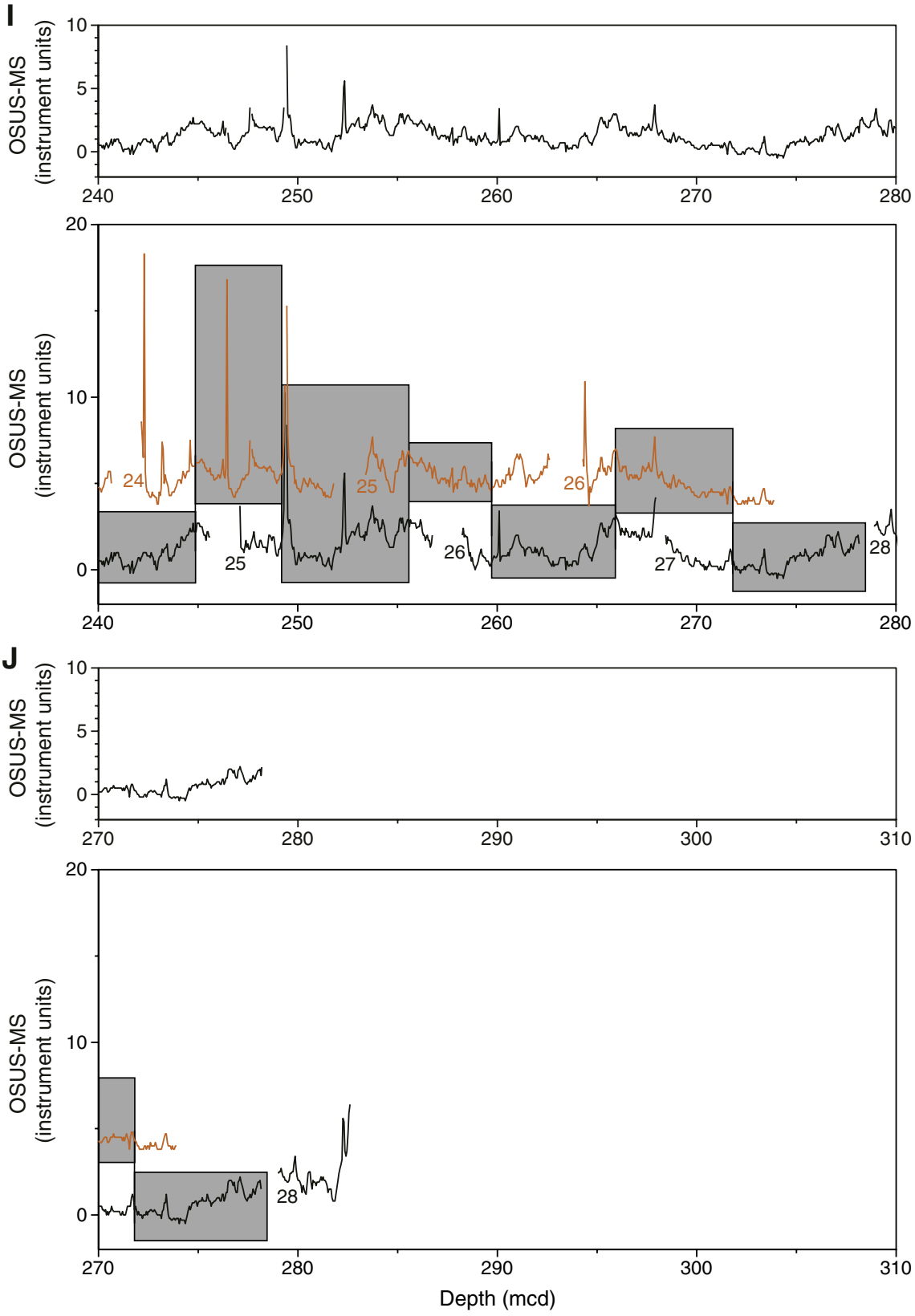

Figure F9. Smoothed (9-point Gaussian) spliced records of natural gamma radiation (NGR), gamma ray attenuation (GRA) bulk density, and magnetic susceptibility (MST-MS) for Site 1240.

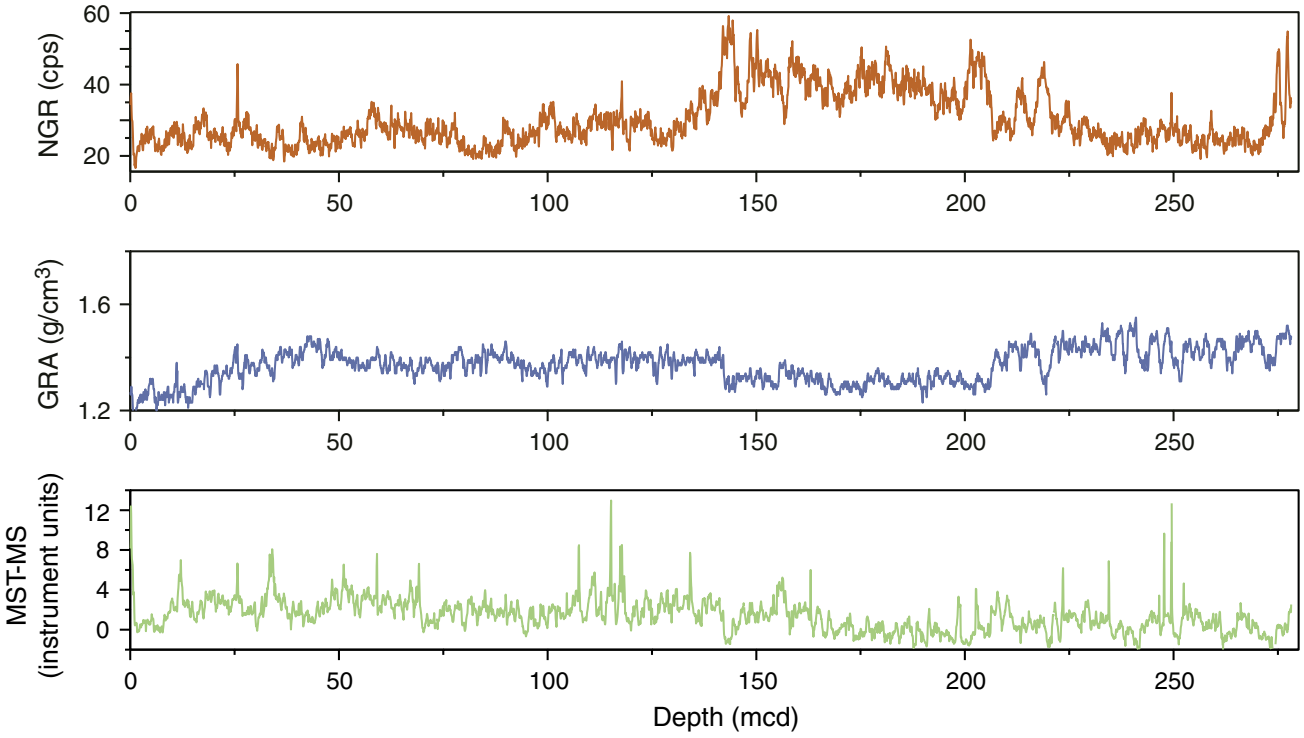

Figure F10. Smoothed (9-point Gaussian) spliced records of color reflectance from Site 1240: L*, a*, and b*.

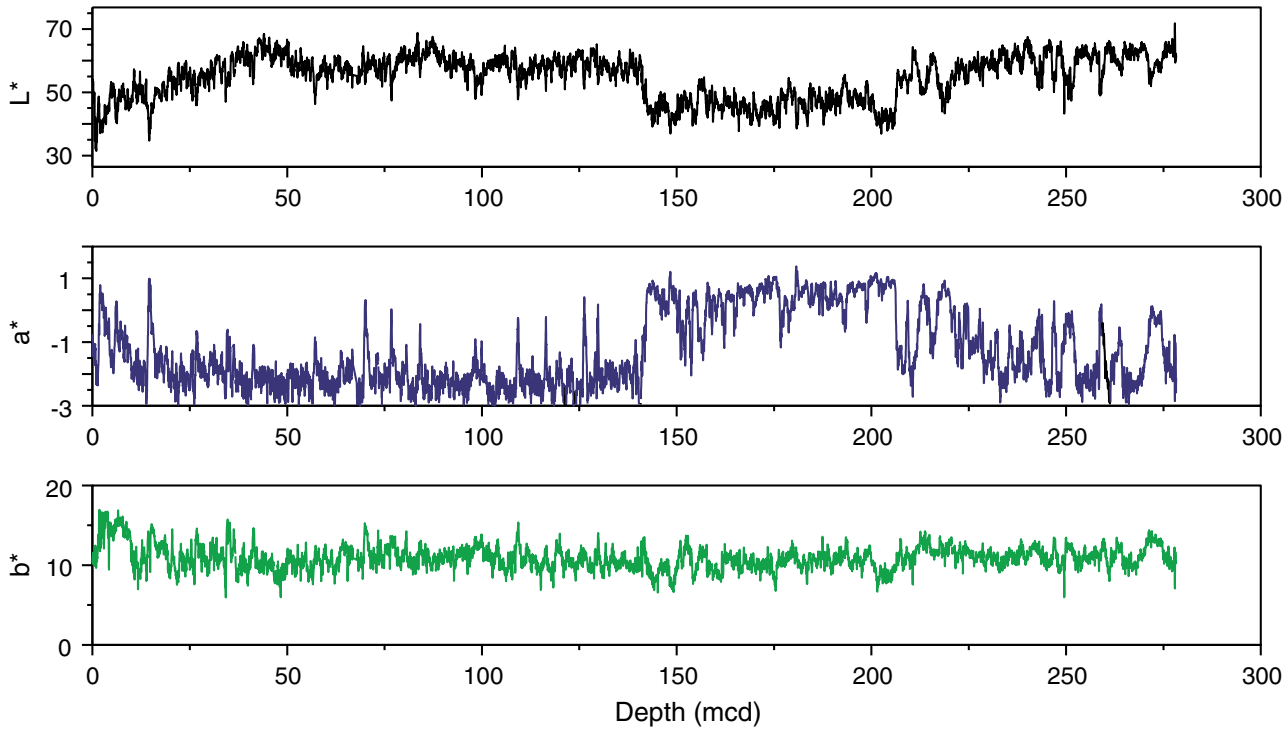

Figure F11. A comparison of the drillers depth (mbsf) and meters composite depth (mcd) scales in Holes 1240A through 1240D. On average, mcd is 11% greater than mbsf. The 1:1 (mbsf:mcd) line is also shown for comparison. GF = growth factor.

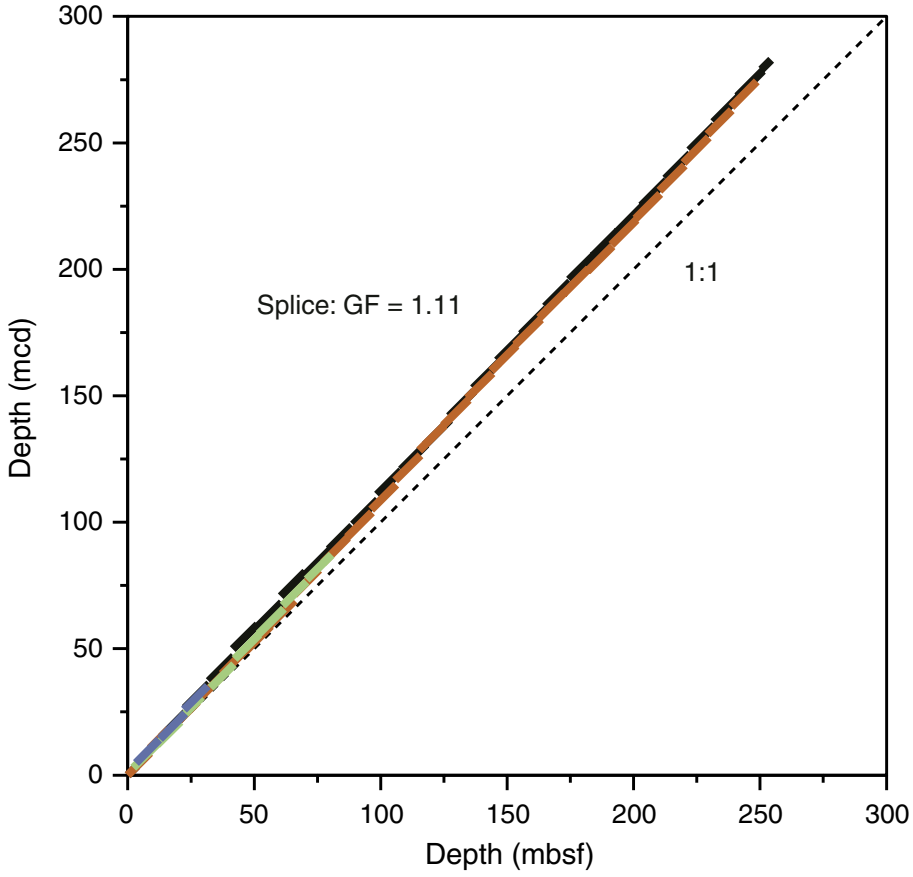

Figure F12. Core recovery, lithostratigraphic subunits, age, magnetic susceptibility, gamma ray attenuation (GRA) bulk density, *P*-wave velocity (V_P), natural gamma radiation (NGR), lightness, a*, total organic carbon (TOC), and calcium carbonate ($CaCO_3$) of sediments recovered from Site 1240. Gray lines show the original data, black lines are 50-point smoothing averages of the original data.

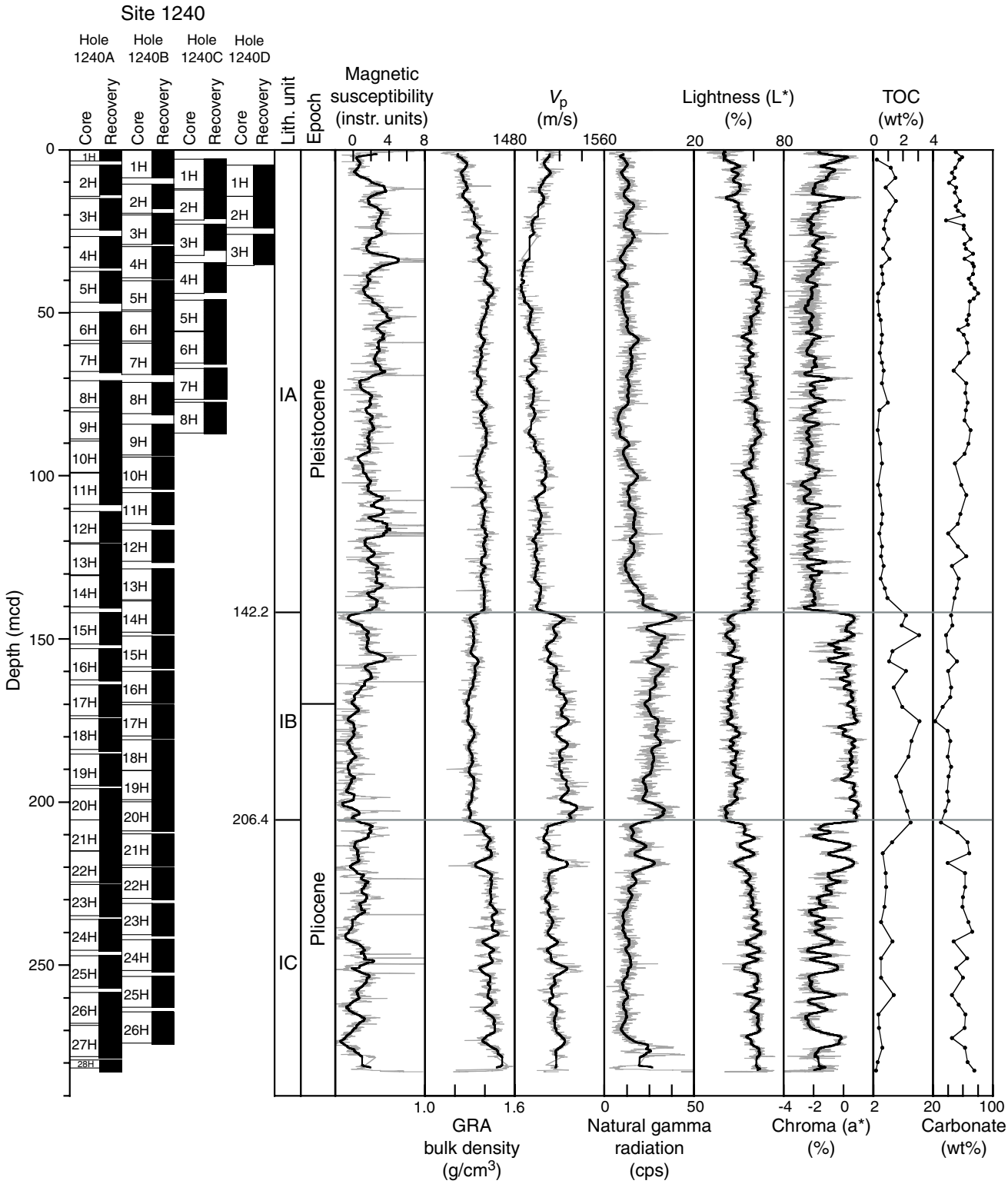

Figure F13. Major siliciclastic, biogenic, and authigenic components observed in Site 1240 smear slides. Symbols on the volcanic glass panel indicate the position of the ash layers. White diamonds = ash layers containing traces of brownish volcanic glass, white square = ash layer fully composed of brown volcanic glass. Rad. = radiolarians, silicof. = silicoflagellates.

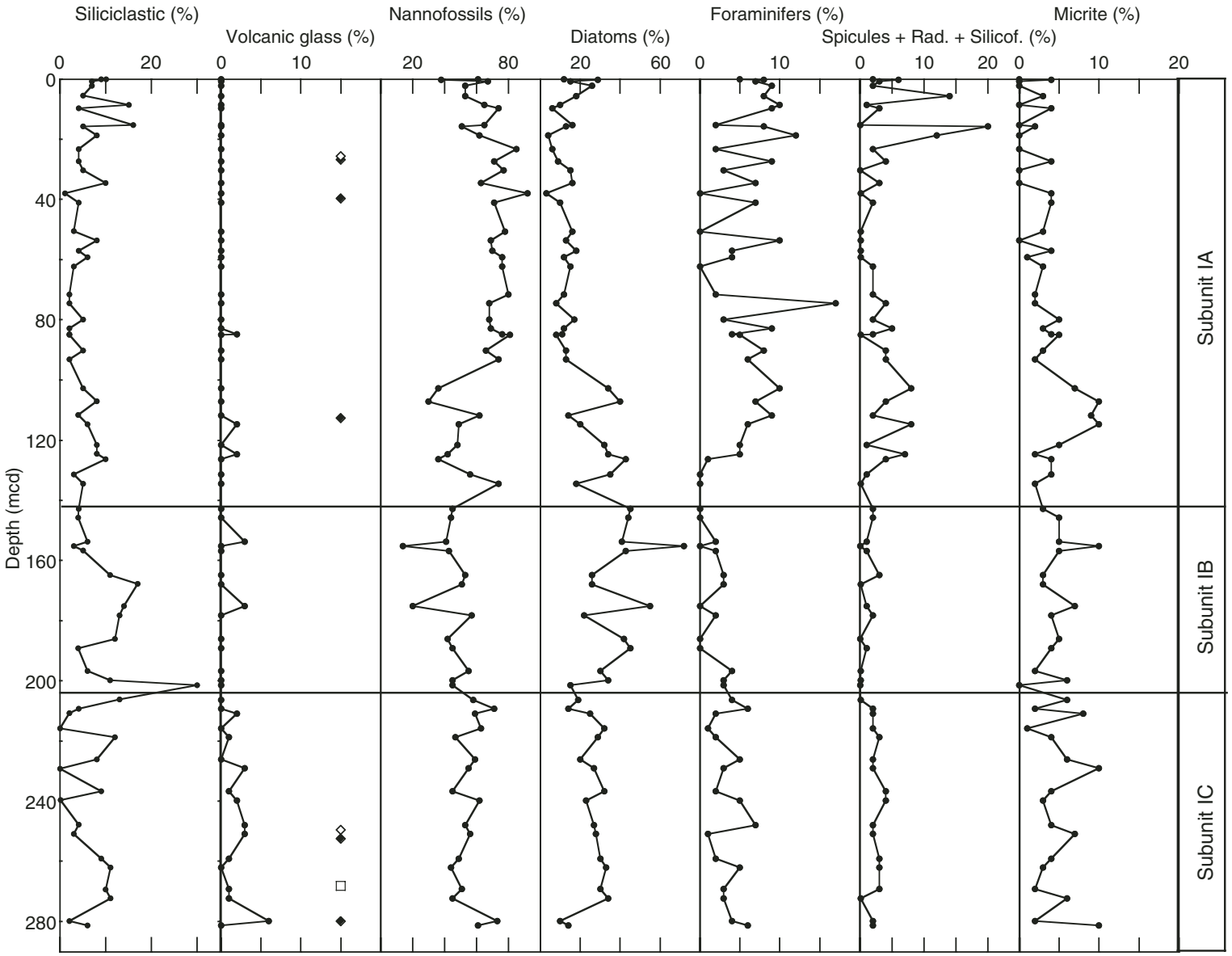

Figure F14. Physical properties measurements for Site 1240. **A.** Gamma ray attenuation (GRA) bulk density and moisture and density (MAD) bulk density. **B.** Porosity. **C.** Grain density. **D.** Correlation between interpolated GRA and discrete MAD bulk density measurements. **E.** Correlation between MAD bulk density and porosity. **F.** Correlation between carbonate and grain density.

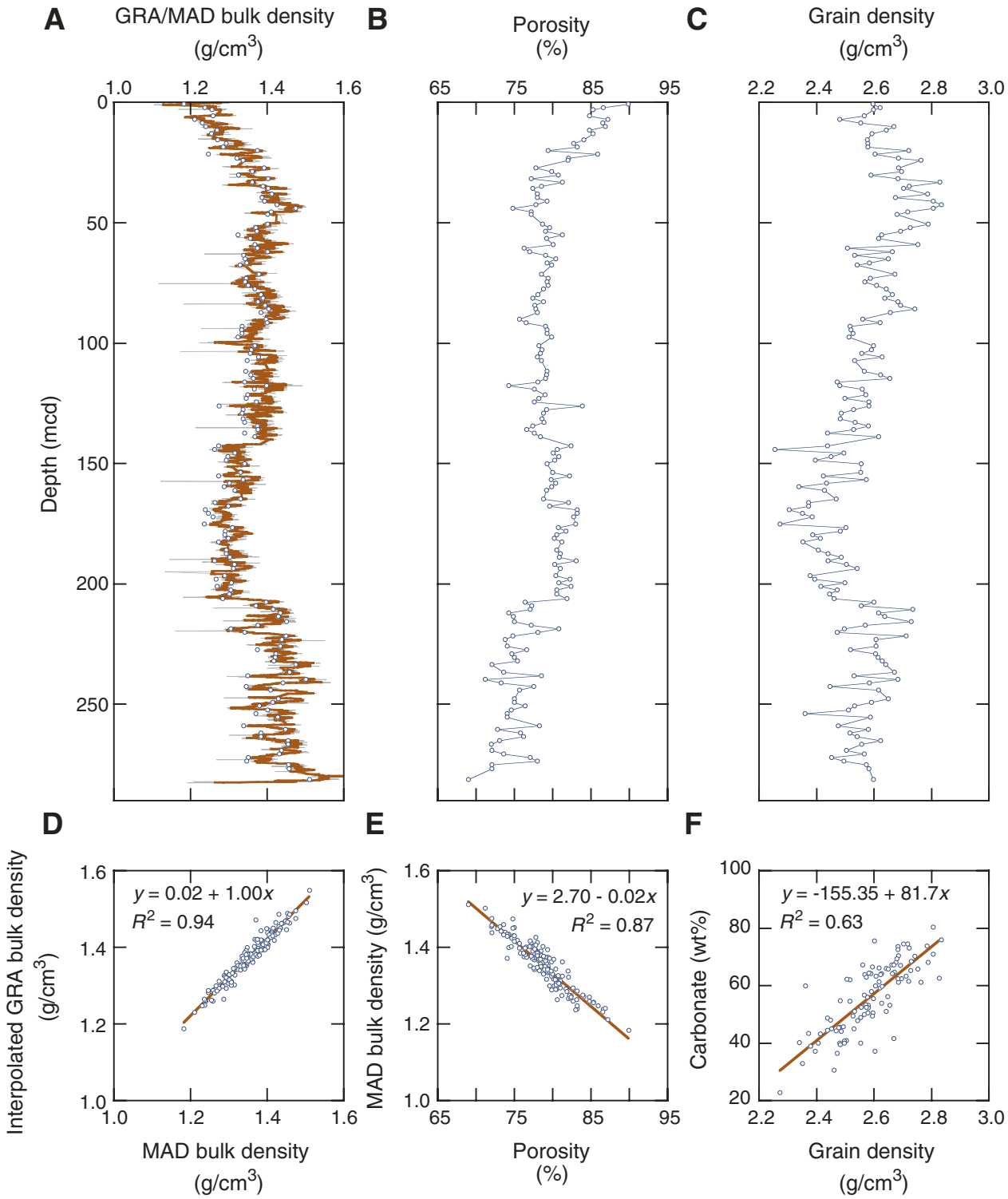

Figure F15. **A.** Sequential depth plots of raw reflectance data for Site 1240. **B.** First derivatives of raw reflectance data. Red lines = absorption features typical of organic pigments (i.e., at 410, 510, 560, and 650 nm). **C.** The depth of the absorption feature at 650 nm, estimated relative to 630 and 700 nm and normalized to a measure of the general slope of the spectrum, is plotted with depth as a proxy for the abundance of chlorins. Total organic carbon (TOC) measurements are also plotted for comparison.

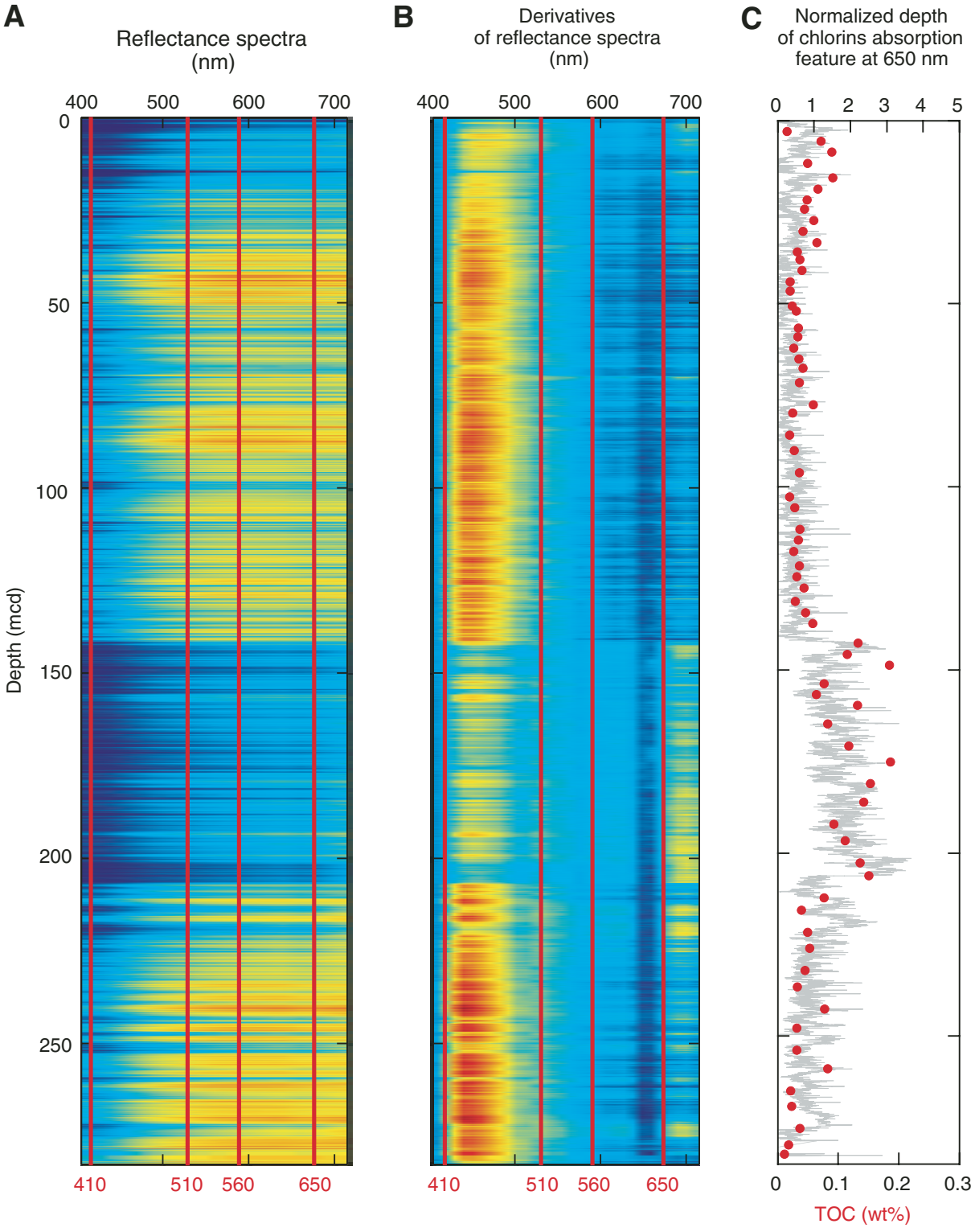

Figure F16. Close-up photograph of evidence of bioturbation at Site 1240. **A.** Vertical burrow (interval 202-1240A-1H-1, 121–141 cm). **B.** Color mottles and *Zoophycos* (interval 202-1240B-14H-2, 121–141 cm). **C.** *Zoophycos* (interval 202-1240D-1H-5, 30–60 cm).

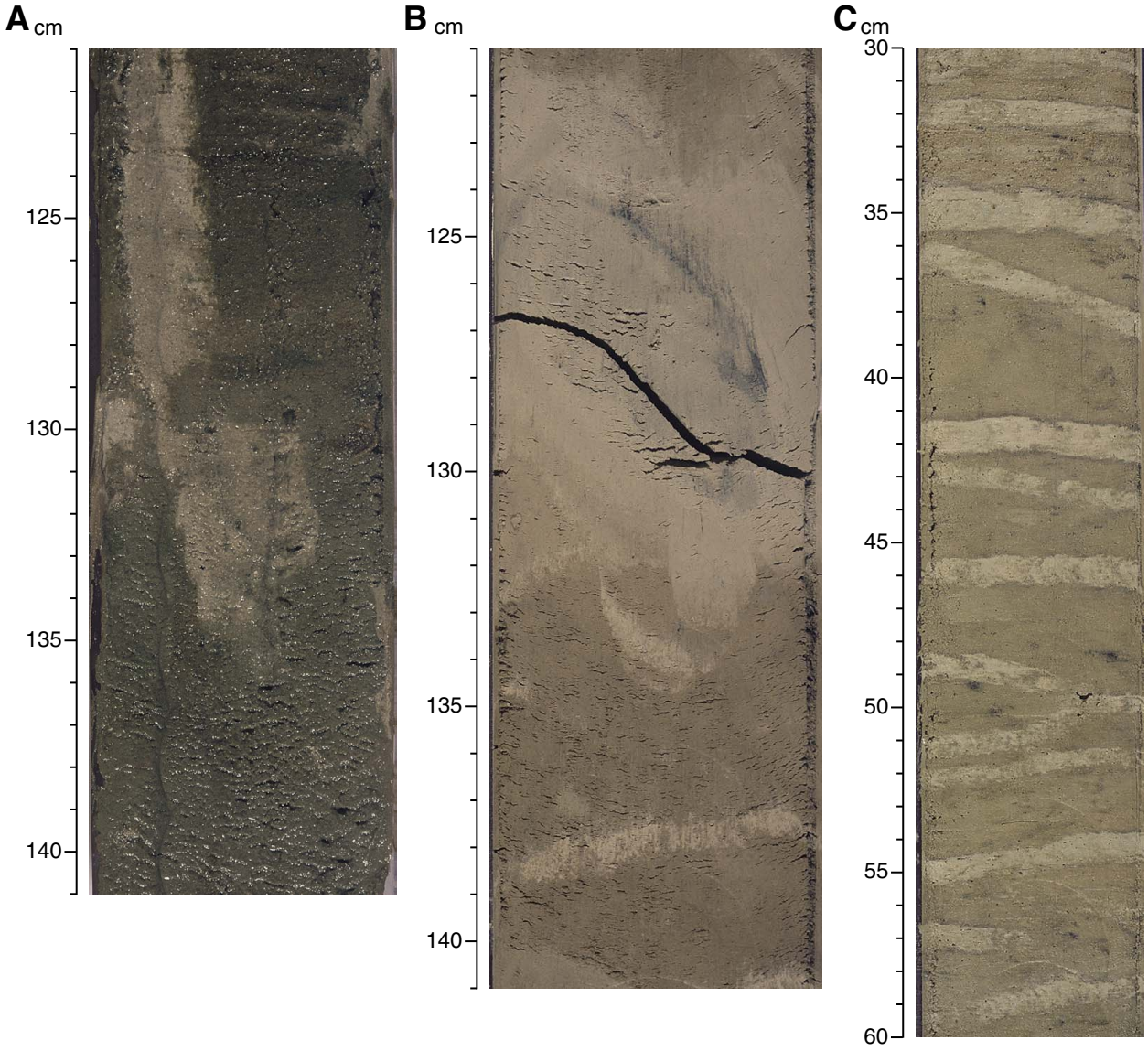

Figure F17. Close-up photograph of color banding frequently observed in Subunit IB; dark olive bands are enriched in pennate diatoms. The photograph corresponds to the base of Subunit IA (interval 202-1240A-12H-4, 83–106 cm), where this banding, typical of Subunit IB, is rare.

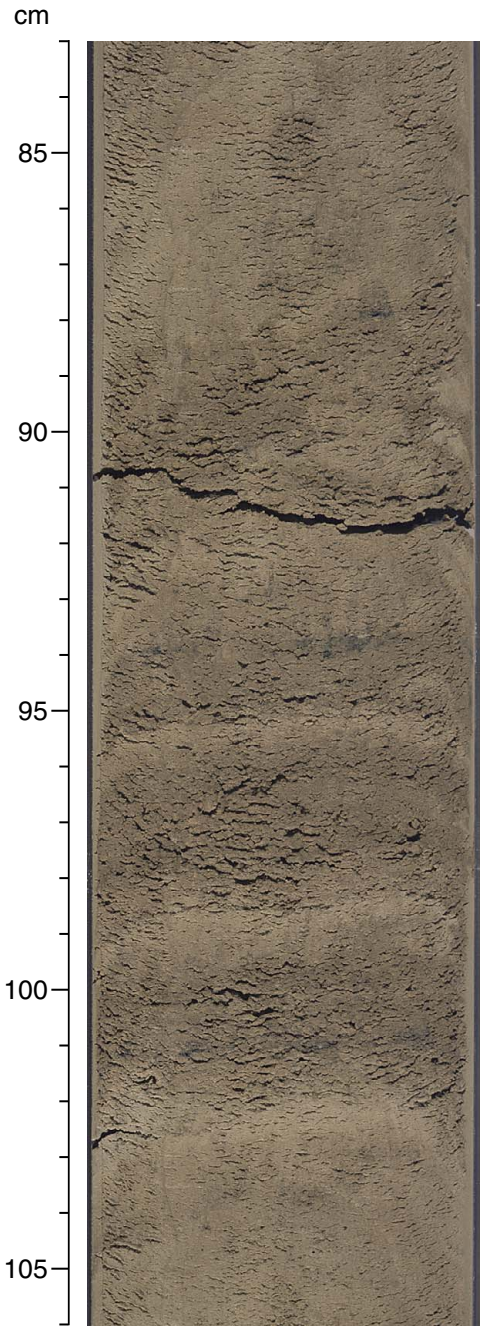

Figure F18. Ash layers in (**A**) interval 202-1240A-22H-6, 100–110 cm, and (**B**) interval 202-1240A-25H-2, 82–97 cm.

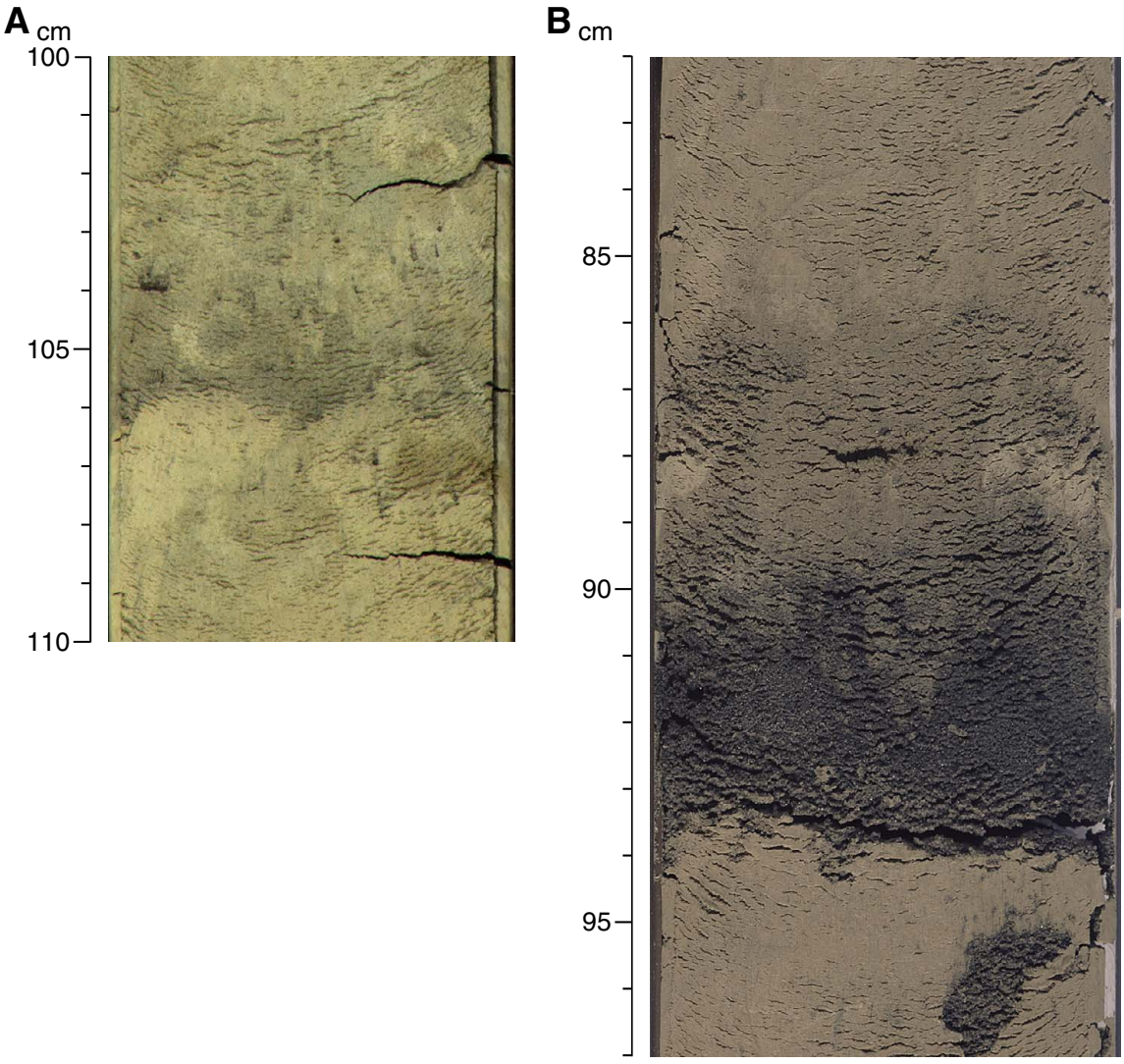

Figure F19. Color measurements for Site 1240 (spliced record) plotted in the a*-b* color plane (left). A close up of the measurement field (right) shows that color values in Subunit IB are a distinct population characterized by a red hue (i.e., a* > 0).

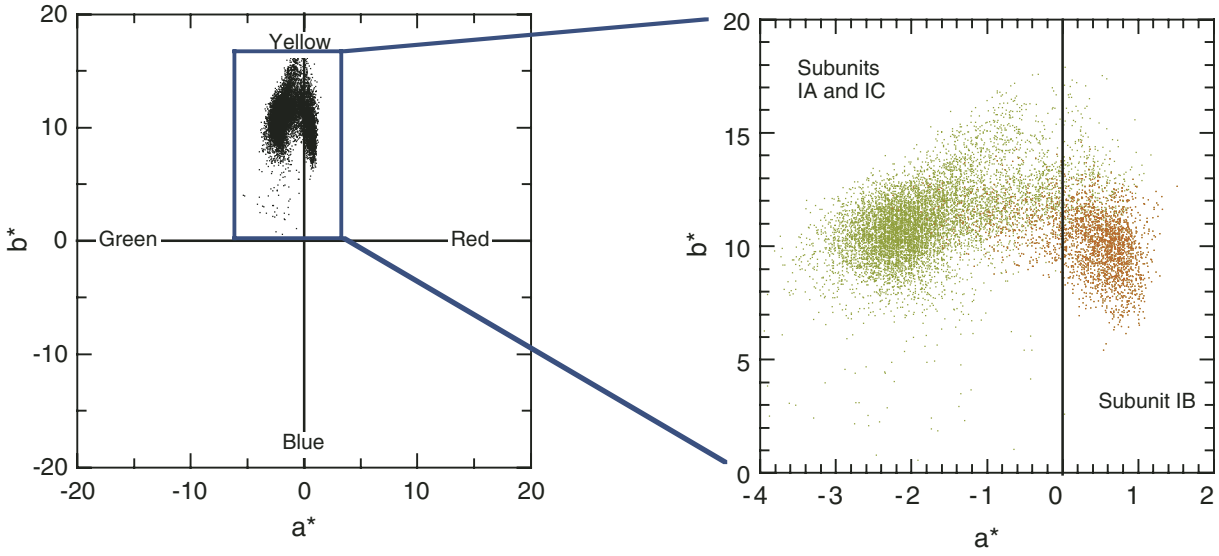

Figure F20. A. Sediment located immediately above the basaltic basement (interval 202-1240A-28H-3, 33–76 cm). **B.** X-ray diffractogram of the green grains forming the coarse fraction (>250 µm) in Section 202-1240A-28H-CC. Several peaks are indicative of smectite minerals (probably nontronite), and other peaks indicate plagioclase. The background hump around 27°2θ indicates volcanic glass.

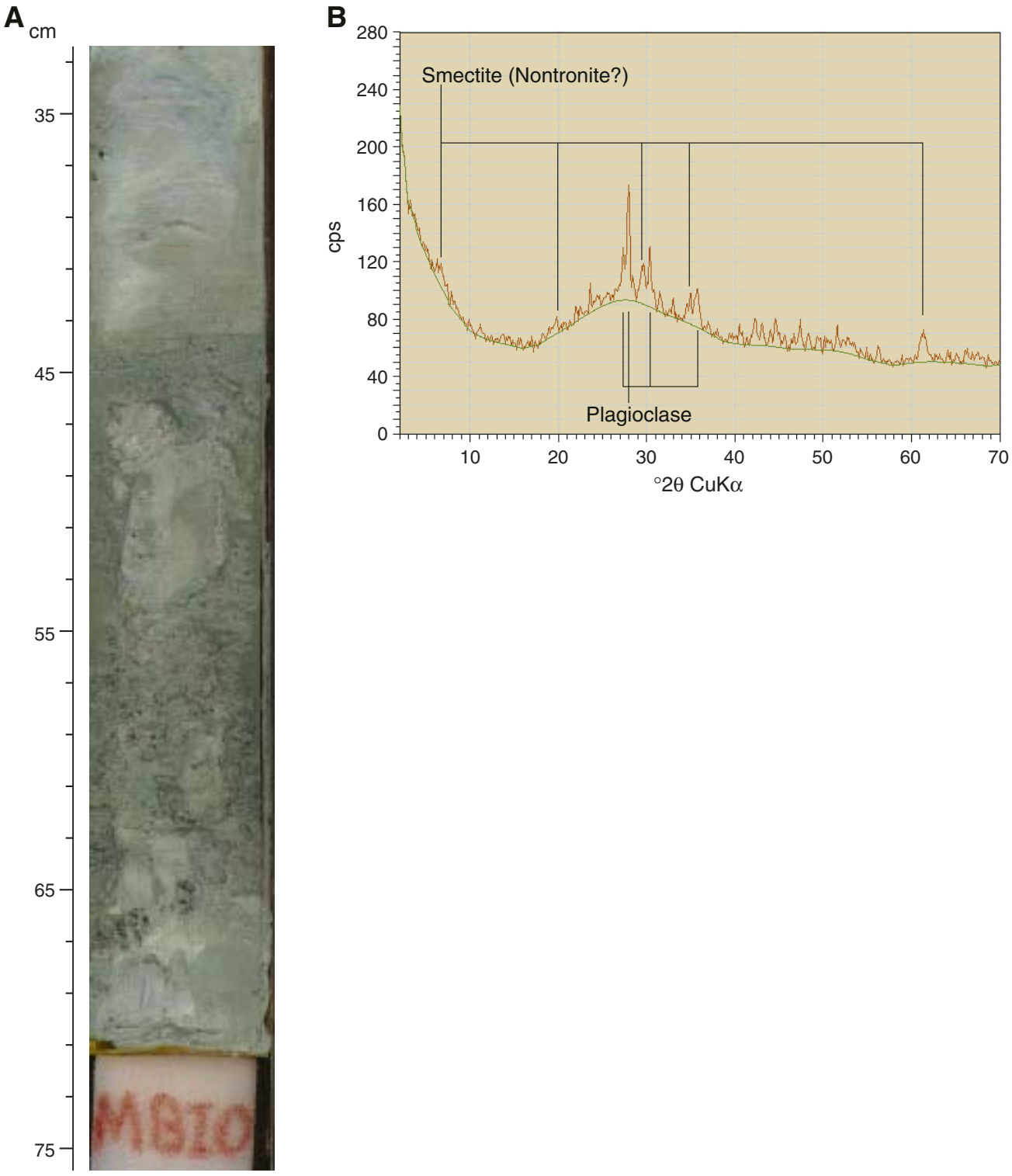

Figure F21. Downhole distribution of ash layers for Sites 1240, 1239, and 1238, plotted on an age vs. depth profile based on biostratigraphic datums. Length of bars = ash layer thickness. Color shade = time interval of Subunit IB at Site 1240. The map at the bottom indicates the geographical position of the sites.

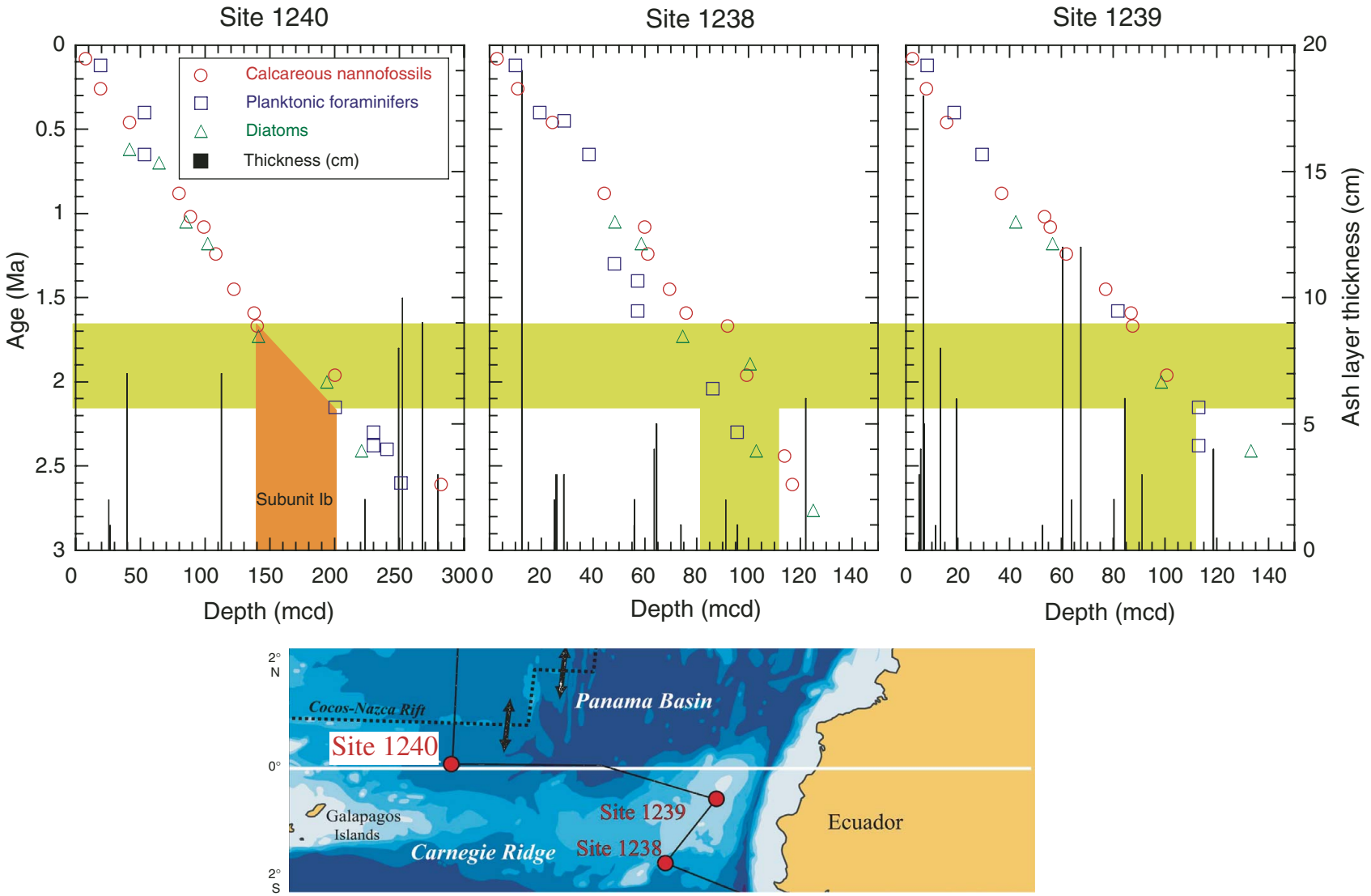

Figure F22. Core recovery, calcareous nannofossil and foraminifer abundance, benthic foraminifer percentage of total foraminifers, and diatom abundance at Hole 1240A (smoothed lines). F = few, C = common, A = abundant, VA = very abundant.

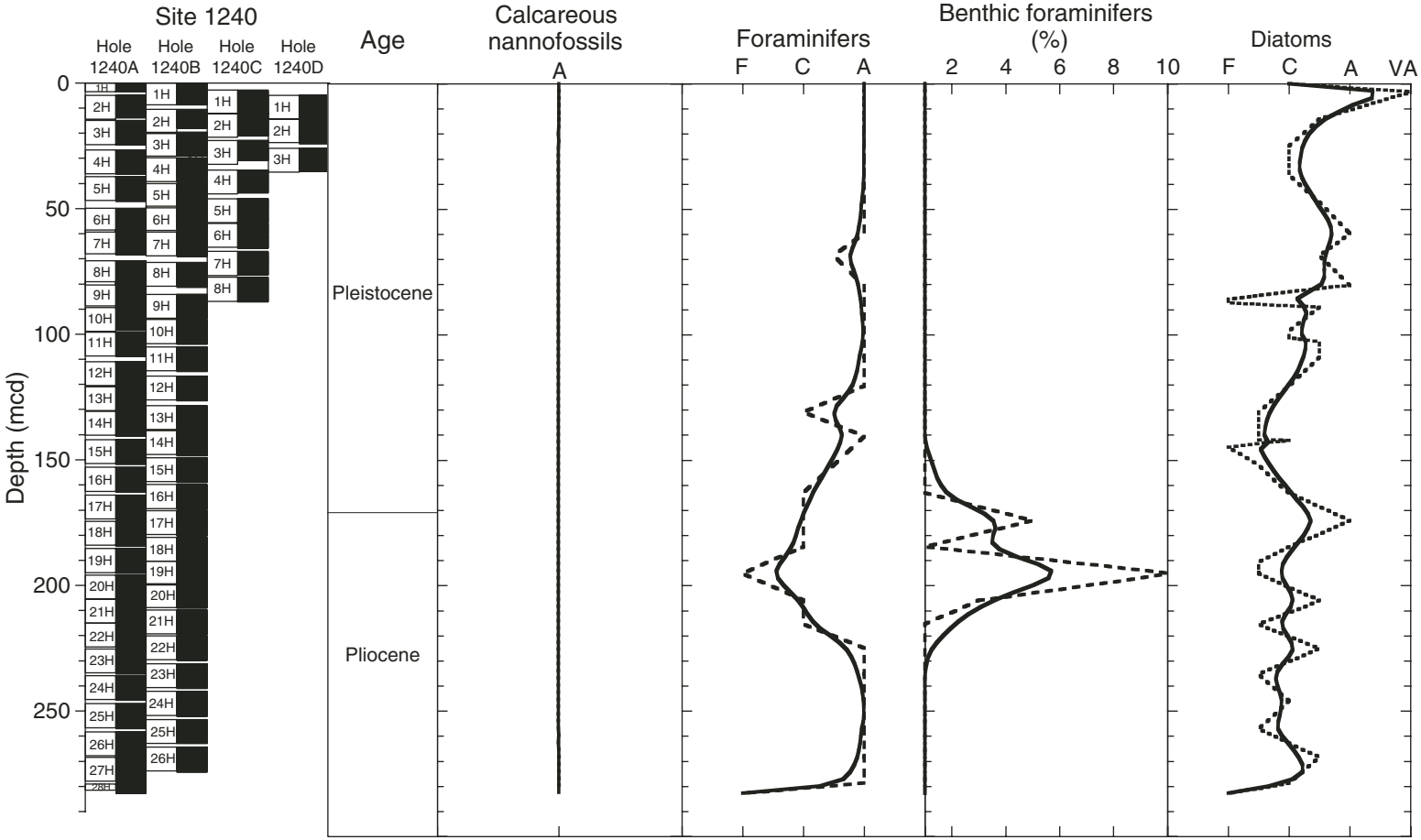

Figure F23. Site 1240 natural remanent magnetization (NRM) intensity vs. depth before (black) and after (blue) AF demagnetization at peak fields of 20 mT. Core recovery is shown for reference.

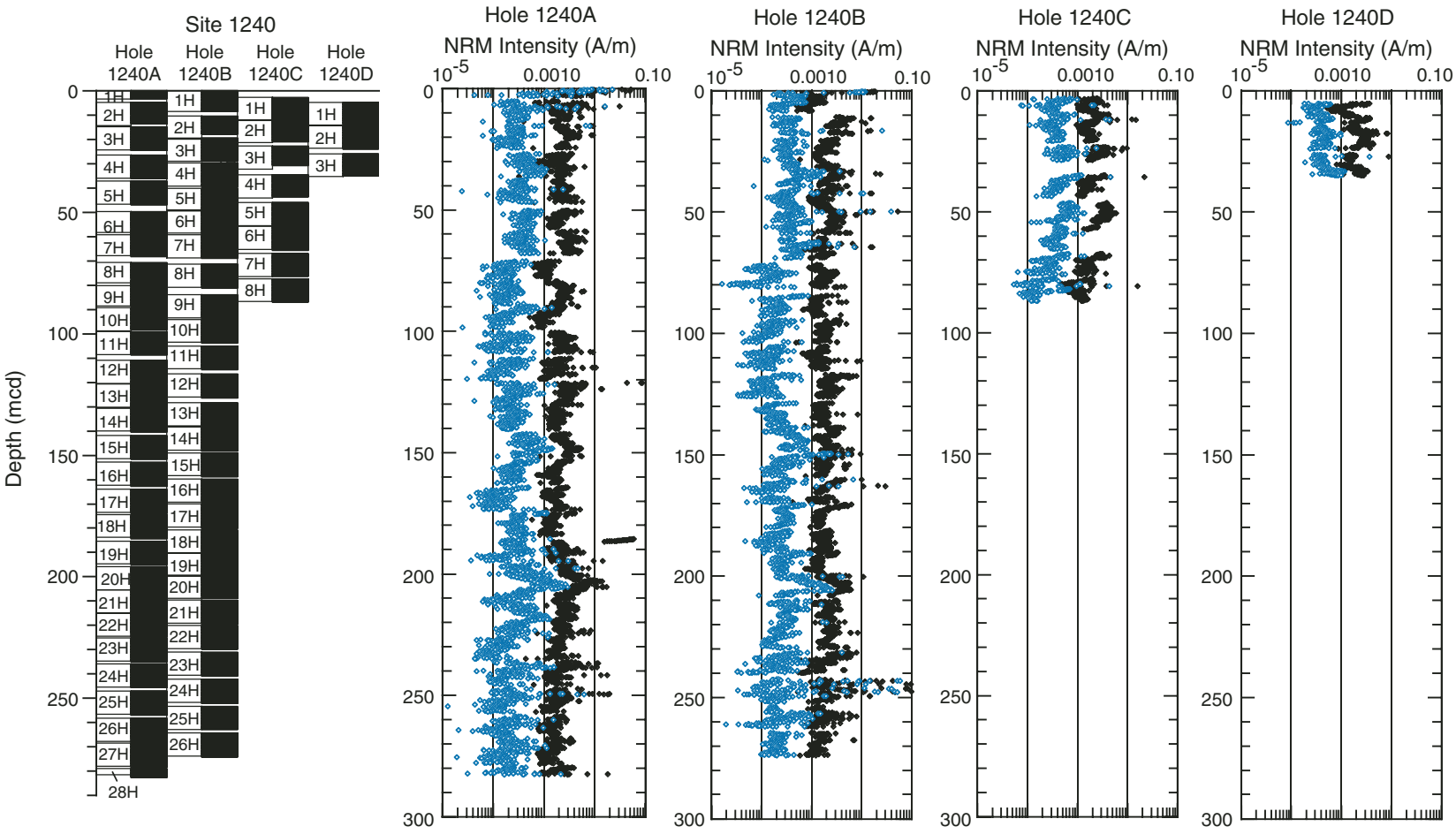

Figure F24. Site 1240 inclinations vs. depth after demagnetization at peak alternating fields of 20 mT. Core recovery is shown for reference.

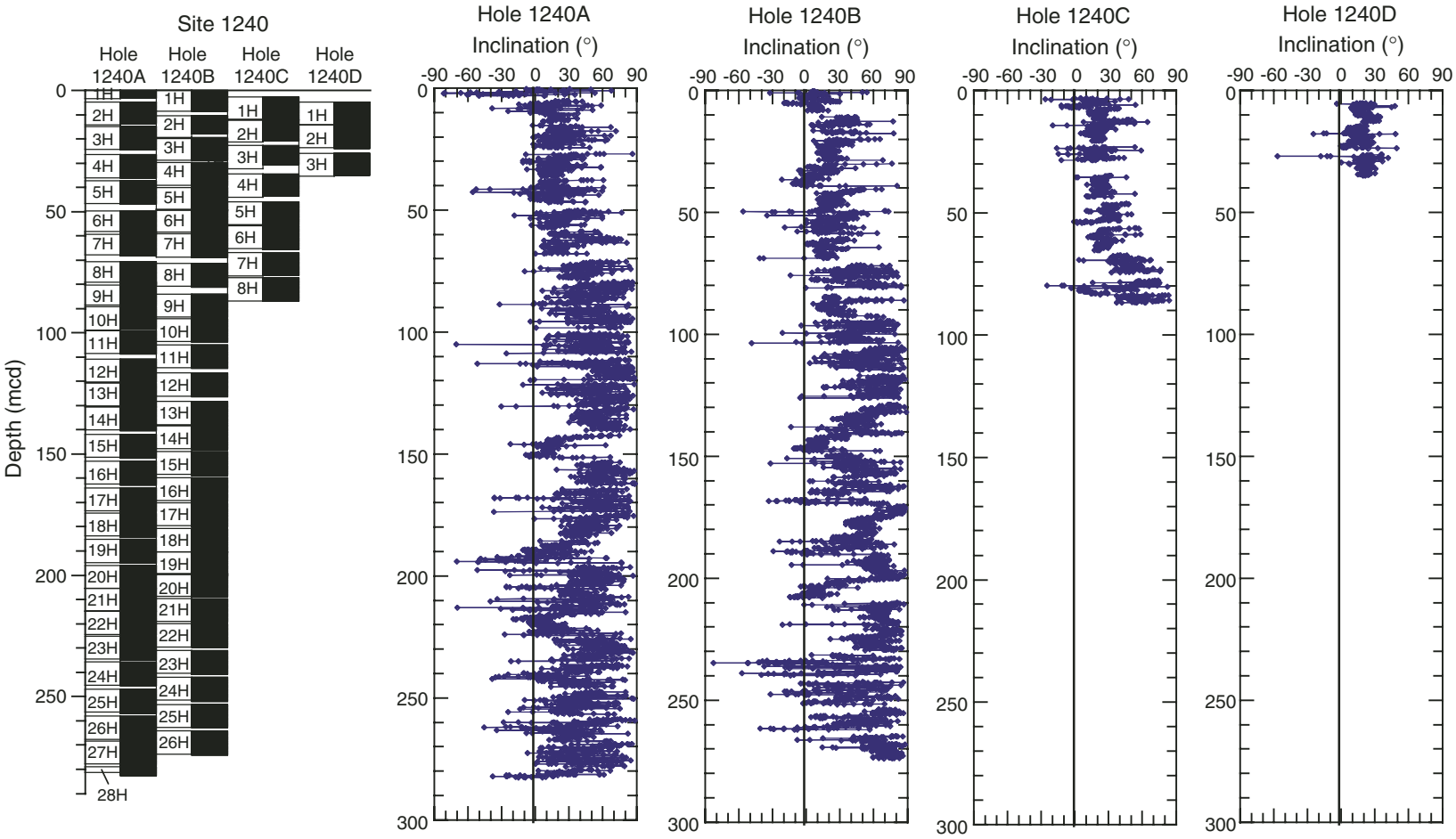

Figure F25. Site 1240 declinations vs. depth after demagnetization at peak alternating fields of 20 mT. Core recovery is shown for reference.

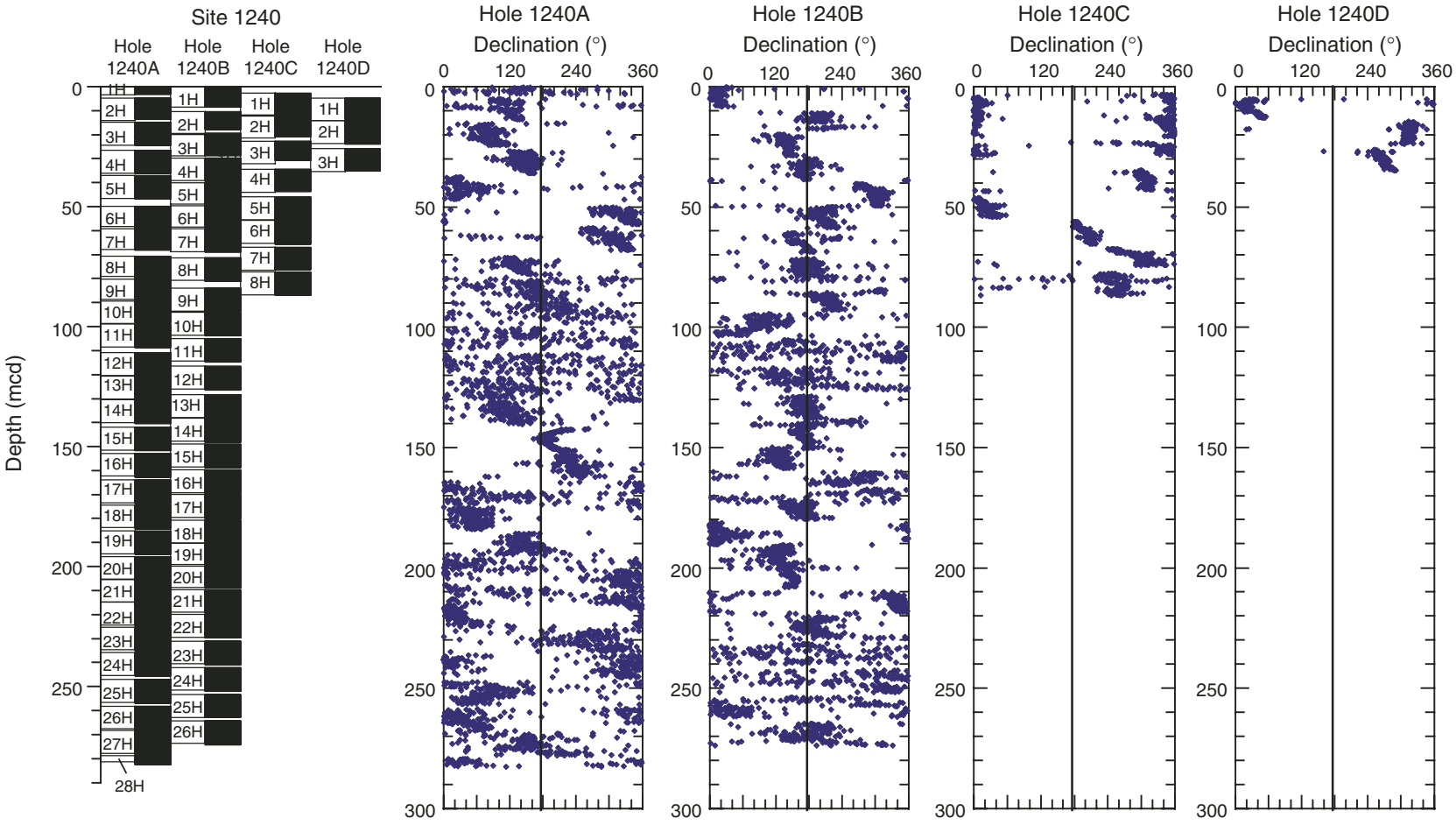

Figure F26. Site 1240 Tensor-corrected declinations vs. depth after demagnetization at peak alternating fields of 20 mT. Polarity interpretations are shown at right.

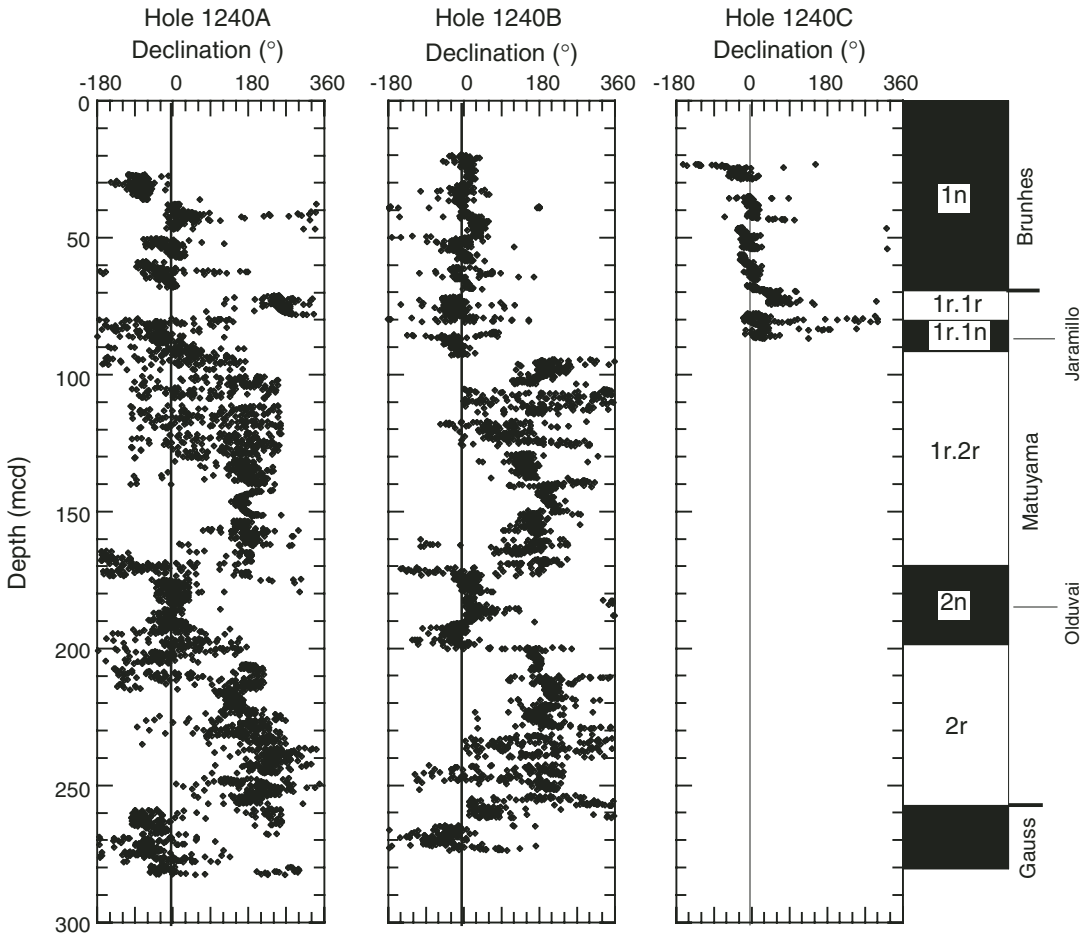

Figure F27. Headspace methane (C_1) concentrations in sediments vs. depth for Hole 1240A.

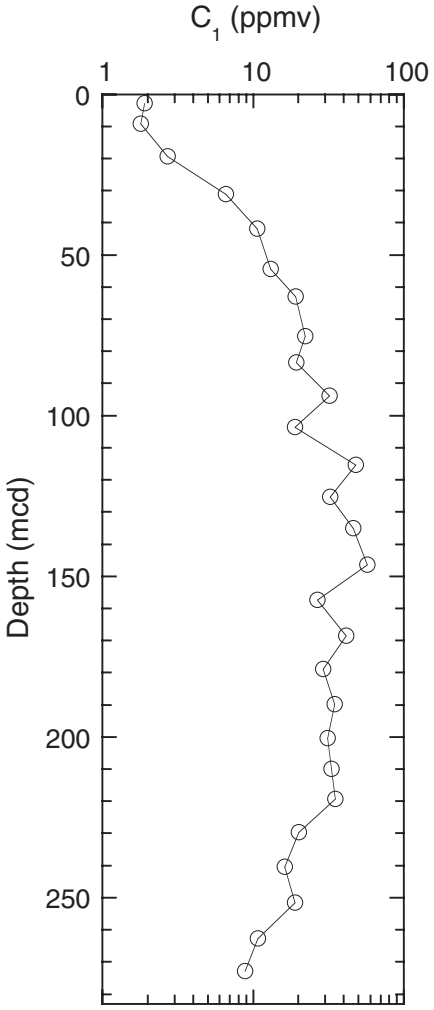

Figure F28. Interstitial water geochemical data for Site 1240. Open squares = calcium concentrations. Horizontal dashed lines indicate lithologic subunit boundaries (see **"Description of Lithologic Unit,"** p. 5, in "Lithostratigraphy"). Values below the detection limit (0.15 mM for ammonium) are plotted at zero. Note that the blank correction for iron (0.8 µM) was significant compared to many of the measured concentrations, so this profile should be interpreted with caution.

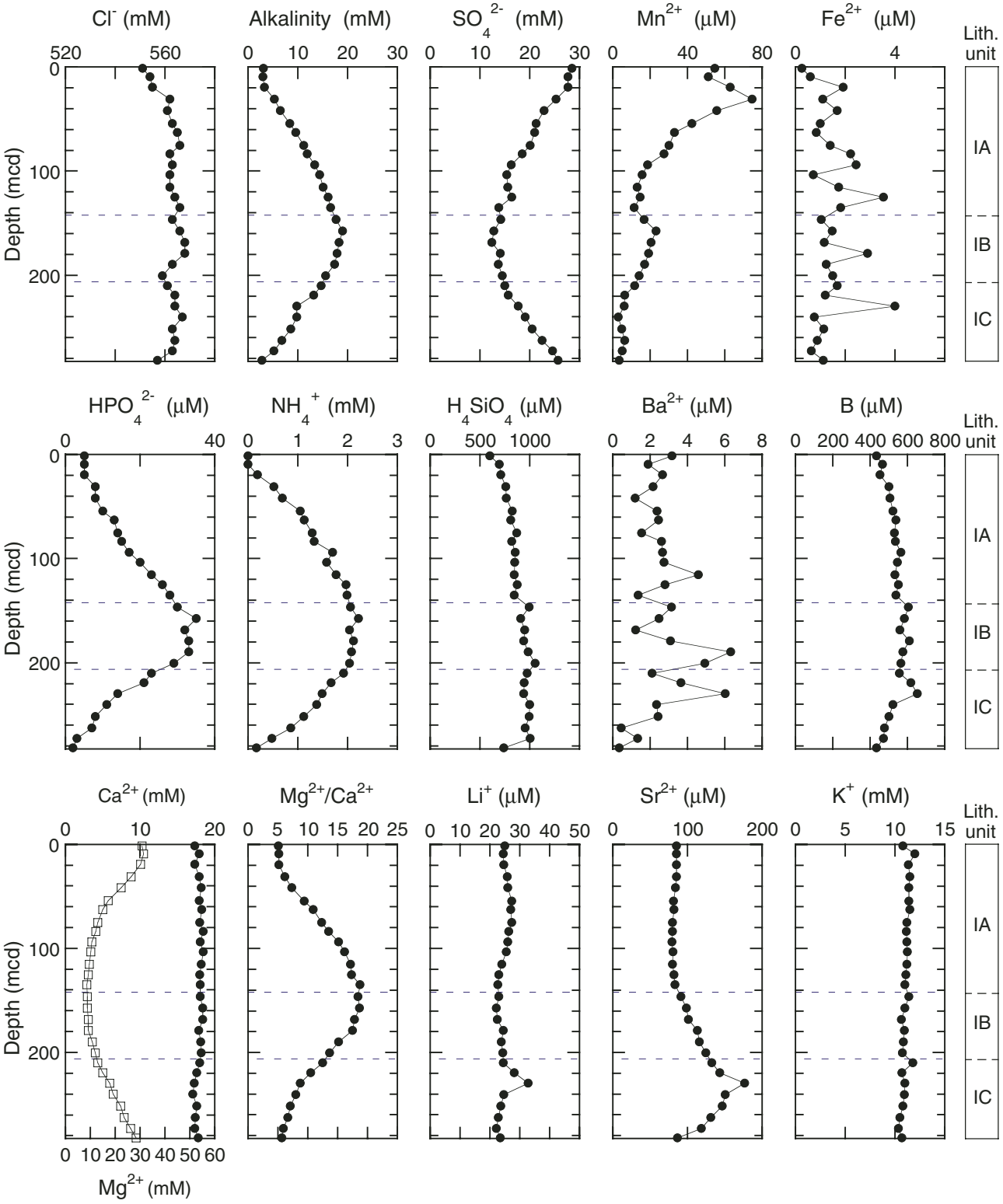

Figure F29. Calcium carbonate ($CaCO_3$), total organic carbon (TOC), TOC on a carbonate-free basis (TOC CFB), and total nitrogen (TN) concentrations, and TOC/TN ratios vs. depth in sediments for Hole 1240A.

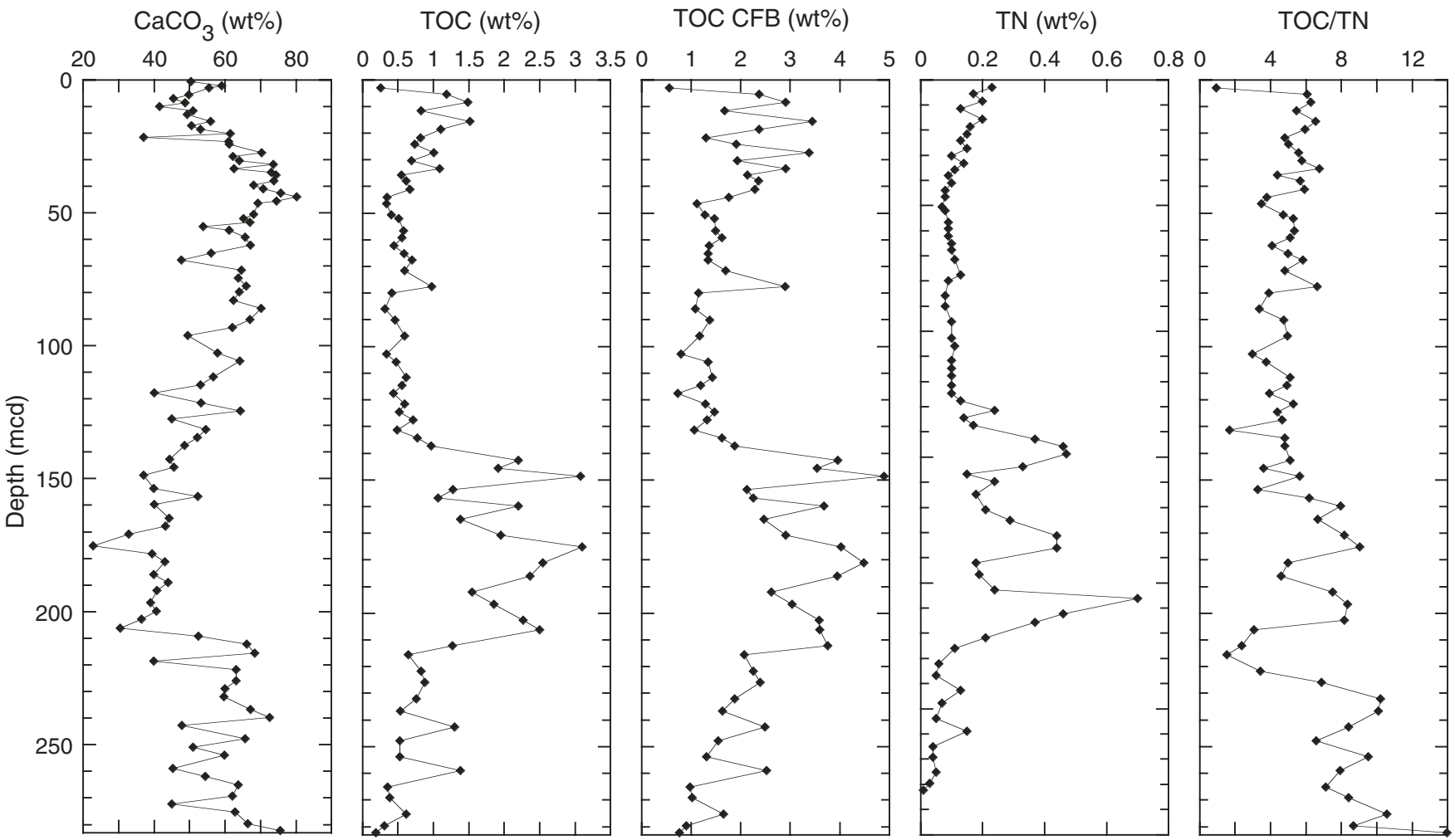

Figure F30. Calcium carbonate ($CaCO_3$) vs. total organic carbon (TOC) concentrations and total nitrogen (TN) vs. TOC concentrations in sediments of Hole 1240A.

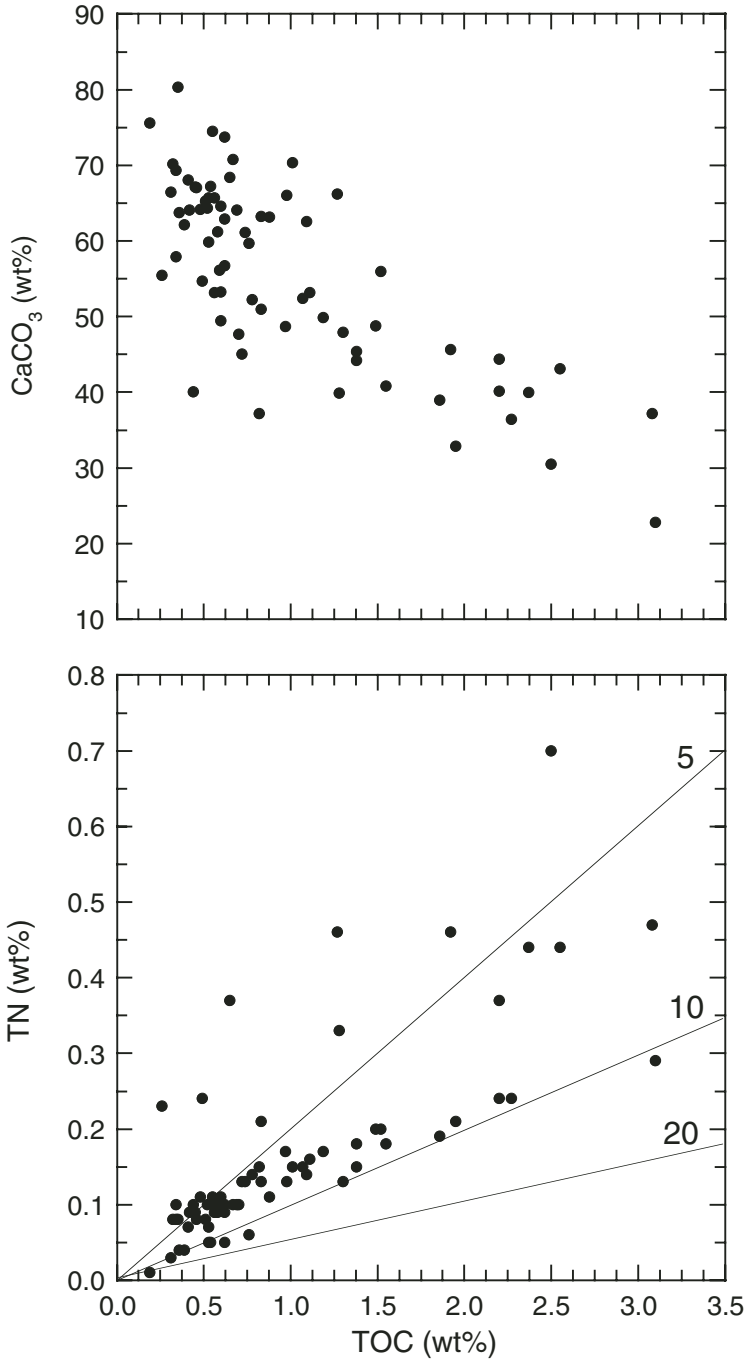

Figure F31. S_2 vs. total organic carbon (TOC) and hydrogen index (HI) vs. TOC. Boundaries for Types I, II, and III kerogen fields are taken from Langford and Blanc-Valleron (1990).

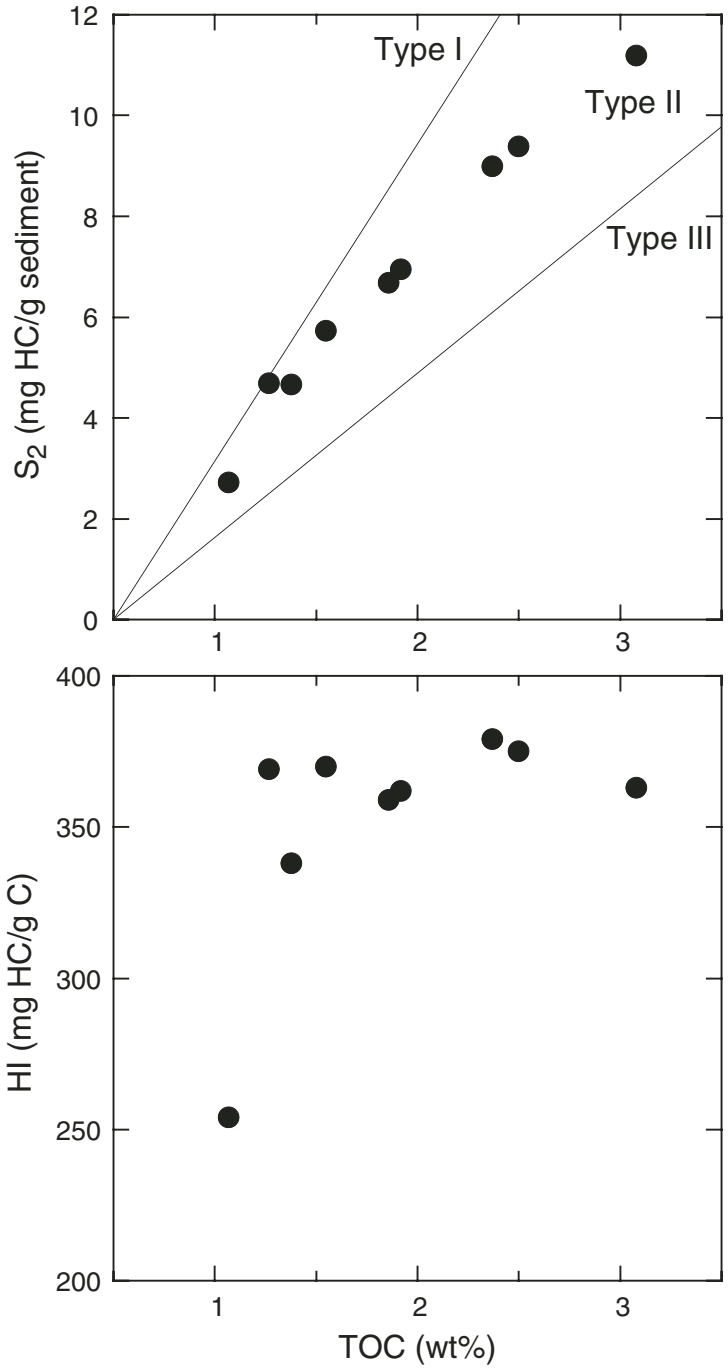

Figure F32. A. Shipboard biostratigraphic and magnetostratigraphic datums and age-depth model. **B.** Corrected linear sedimentation rates (LSRs), total mass accumulation rates (MARs), and carbonate mass accumulation rates calculated from the smooth age model, average dry density, and calcium carbonate concentrations at 0.4-m.y. intervals. FO = first occurrence, LO = last occurrence.

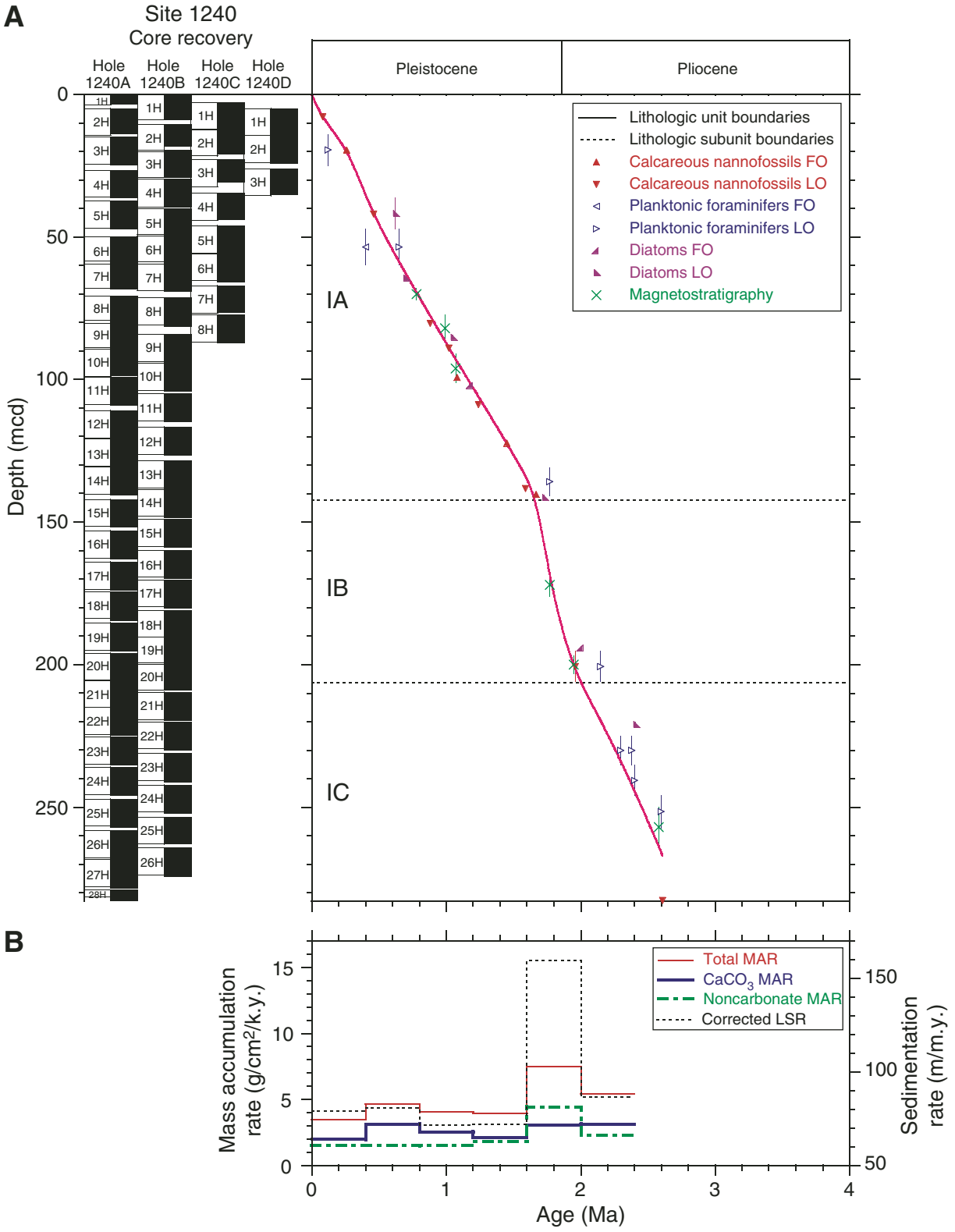

Table T1. Operations summary, Site 1240. (See table notes. Continued on next page.)

Core	Date (May 2002)	Local time (hr)	Depth (mbsf) Top	Depth (mbsf) Bottom	Length (m) Cored	Length (m) Recovered	Recovery (%)	APCT	Orientation	NMCB
202-1240A-										
1H	16	0810	0.0	3.5	3.5	3.54	101.1			
2H	16	0855	3.5	13.0	9.5	9.11	95.9			X
3H	16	0935	13.0	22.5	9.5	9.84	103.6			
4H	16	1020	22.5	32.0	9.5	9.79	103.1		Tensor	X
5H	16	1105	32.0	41.5	9.5	9.93	104.5		Tensor	
6H	16	1225	41.5	51.0	9.5	9.81	103.3	X	Tensor	X
7H	16	1305	51.0	60.5	9.5	9.94	104.6		Tensor	
8H	16	1415	60.5	70.0	9.5	9.71	102.2	X	Tensor	X
9H	16	1500	70.0	79.5	9.5	9.97	105.0		Tensor	
10H	16	1605	79.5	89.0	9.5	9.25	97.4	X	Tensor	X
11H	16	1650	89.0	98.5	9.5	9.82	103.4		Tensor	
12H	16	1755	98.5	108.0	9.5	9.64	101.5	X	Tensor	X
13H	16	1845	108.0	117.5	9.5	9.96	104.8		Tensor	
14H	16	1950	117.5	127.0	9.5	9.95	104.7	X	Tensor	X
15H	16	2045	127.0	136.5	9.5	9.94	104.6		Tensor	
16H	16	2150	136.5	146.0	9.5	10.08	106.1	X	Tensor	X
17H	16	2240	146.0	155.5	9.5	9.97	105.0		Tensor	
18H	16	2345	155.5	165.0	9.5	10.13	106.6	X	Tensor	X
19H	17	0055	165.0	174.5	9.5	9.89	104.1		Tensor	
20H	17	0155	174.5	184.0	9.5	9.95	104.7		Tensor	
21H	17	0250	184.0	193.5	9.5	9.79	103.1		Tensor	
22H	17	0340	193.5	203.0	9.5	10.01	105.4		Tensor	
23H	17	0430	203.0	212.5	9.5	10.01	105.4		Tensor	
24H	17	0535	212.5	222.0	9.5	9.91	104.3		Tensor	
25H	17	0655	222.0	231.5	9.5	10.06	105.9		Tensor	
26H	17	0755	231.5	241.0	9.5	10.02	105.5		Tensor	
27H	17	0900	241.0	250.5	9.5	10.14	106.7		Tensor	
28H	17	0955	250.5	253.0	2.5	3.87	154.8		Tensor	
				Cored totals:	253.0	264.03	104.4			
202-1240B-										
1H	17	1340	0.0	8.7	8.7	8.79	101.0	X		X
2H	17	1420	8.7	18.2	9.5	7.61	80.1			
3H	17	1510	18.2	27.7	9.5	9.52	100.2		Tensor	X
4H	17	1552	27.7	37.2	9.5	9.92	104.4		Tensor	
5H	17	1645	37.2	46.7	9.5	9.79	103.1		Tensor	X
6H	17	1735	46.7	56.2	9.5	9.90	104.2		Tensor	
7H	17	1820	56.2	65.7	9.5	9.80	103.2		Tensor	X
8H	17	1905	65.7	75.2	9.5	9.96	104.8		Tensor	
9H	17	1955	77.2	86.7	9.5	9.87	103.9		Tensor	X
10H	17	2040	86.7	96.2	9.5	9.87	103.9		Tensor	
11H	17	2125	96.2	105.7	9.5	9.91	104.3		Tensor	X
12H	17	2215	105.7	115.2	9.5	9.98	105.1		Tensor	
13H	17	2300	115.2	124.7	9.5	9.97	105.0		Tensor	X
14H	17	2345	124.7	134.2	9.5	10.08	106.1		Tensor	
15H	18	0040	134.2	143.7	9.5	10.01	105.4		Tensor	X
16H	18	0130	143.7	153.2	9.5	10.02	105.5		Tensor	
17H	18	0245	153.2	162.7	9.5	10.20	107.4	X	Tensor	X
18H	18	0345	162.7	172.2	9.5	10.00	105.3		Tensor	
19H	18	0500	172.2	181.7	9.5	10.10	106.3	X	Tensor	X
20H	18	0610	181.7	191.2	9.5	9.90	104.2		Tensor	
21H	18	0725	191.2	200.7	9.5	9.98	105.1	X	Tensor	X
22H	18	0815	200.7	210.2	9.5	9.87	103.9		Tensor	
23H	18	0930	210.2	219.7	9.5	10.03	105.6	X	Tensor	
24H	18	1025	219.7	229.2	9.5	10.06	105.9		Tensor	
25H	18	1130	229.2	238.7	9.5	9.61	101.2		Tensor	
26H	18	1255	238.7	248.2	9.5	10.05	105.8		Tensor	
				Cored totals:	246.2	254.80	103.5			
202-1240C-										
1H	18	1520	2.2	11.7	9.5	9.59	101.0			
2H	18	1620	11.7	21.2	9.5	9.11	95.9			X
3H	18	1740	21.2	30.7	9.5	8.13	85.6	X	Tensor	
4H	18	1900	32.7	42.2	9.5	9.34	98.3		Tensor	X
5H	18	2000	42.2	51.7	9.5	9.70	102.1	X	Tensor	
6H	18	2050	51.7	61.2	9.5	10.00	105.3		Tensor	X
7H	18	2150	61.2	70.7	9.5	9.54	100.4	X	Tensor	
8H	18	2255	70.7	80.2	9.5	9.89	104.1		Tensor	X

Table T1 (continued).

Core	Date (May 2002)	Local time (hr)	Depth (mbsf) Top	Depth (mbsf) Bottom	Length (m) Cored	Length (m) Recovered	Recovery (%)	APCT	Orientation	NMCB
				Cored totals:	76.0	75.30	99.1			
202-1240D-										
1H	20	0050	3.2	12.7	9.5	9.19	96.7			X
2H	20	0140	12.7	22.2	9.5	9.87	103.9			
3H	20	0245	22.2	31.7	9.5	9.35	98.4		Tensor*	X
				Cored totals:	28.5	28.41	99.7			
				Site totals:	603.7	622.54	103.1			

Notes: APCT = advanced hydraulic piston corer temperature tool (stainless-steel housing is cutting shoe). NMCB = nonmagnetic core barrel, including cutting shoe (made from monel). X = APCT or NMCB was used. Tensor = brand name for core-barrel orientation tool. * = Tensor measurement attempted but problem occurred, resulting in bad or no data.

Table T2. Composite depth scale, Site 1240. (See table notes. Continued on next page.)

Core	Depth of core top		Depth offset		Translation to cmcd	
	Drillers (mbsf)	Composite (mcd)	Cumulative (m)	Differential (m)	Growth factor*	Depth (cmcd)†
202-1240A-						
1H	0.0	0.00	0.00	0.00	1.11	0.00
2H	3.5	4.85	1.35	1.35	1.11	4.37
3H	13.0	14.95	1.95	0.60	1.11	13.47
4H	22.5	26.60	4.10	2.15	1.11	23.96
5H	32.0	37.30	5.30	1.20	1.11	33.60
6H	41.5	49.90	8.40	3.10	1.11	44.95
7H	51.0	58.45	7.45	–0.95	1.11	52.66
8H	60.5	70.84	10.34	2.89	1.11	63.82
9H	70.0	79.15	9.15	–1.19	1.11	71.31
10H	79.5	89.40	9.90	0.75	1.11	80.54
11H	89.0	99.17	10.17	0.27	1.11	89.34
12H	98.5	110.95	12.45	2.28	1.11	99.95
13H	108.0	120.85	12.85	0.40	1.11	108.87
14H	117.5	130.65	13.15	0.30	1.11	117.70
15H	127.0	142.00	15.00	1.85	1.11	127.93
16H	136.5	153.00	16.50	1.50	1.11	137.84
17H	146.0	164.05	18.05	1.55	1.11	147.79
18H	155.5	174.45	18.95	0.90	1.11	157.16
19H	165.0	185.35	20.35	1.40	1.11	166.98
20H	174.5	195.95	21.45	1.10	1.11	176.53
21H	184.0	205.50	21.50	0.05	1.11	185.14
22H	193.5	214.95	21.45	–0.05	1.11	193.65
23H	203.0	225.30	22.30	0.85	1.11	202.97
24H	212.5	235.95	23.45	1.15	1.11	212.57
25H	222.0	247.10	25.10	1.65	1.11	222.61
26H	231.5	258.30	26.80	1.70	1.11	232.70
27H	241.0	268.50	27.50	0.70	1.11	241.89
28H	250.5	279.05	28.55	1.05	1.11	251.40
202-1240B-						
1H	0.0	0.00	0.00	0.00	1.11	0.00
2H	8.7	10.55	1.85	1.85	1.11	9.50
3H	18.2	19.55	1.35	–0.50	1.11	17.61
4H	27.7	29.80	2.10	0.75	1.11	26.85
5H	37.2	40.15	2.95	0.85	1.11	36.17
6H	46.7	49.15	2.45	–0.50	1.11	44.28
7H	56.2	59.35	3.15	0.70	1.11	53.47
8H	65.7	71.40	5.70	2.55	1.11	64.32
9H	77.2	84.10	6.90	1.20	1.11	75.77
10H	86.7	94.20	7.50	0.60	1.11	84.86
11H	96.2	105.05	8.85	1.35	1.11	94.64
12H	105.7	116.65	10.95	2.10	1.11	105.09
13H	115.2	128.45	13.25	2.30	1.11	115.72
14H	124.7	138.40	13.70	0.45	1.11	124.68
15H	134.2	149.10	14.90	1.20	1.11	134.32
16H	143.7	159.90	16.20	1.30	1.11	144.05
17H	153.2	170.20	17.00	0.80	1.11	153.33
18H	162.7	180.90	18.20	1.20	1.11	162.97
19H	172.2	190.35	18.15	–0.05	1.11	171.49
20H	181.7	199.35	17.65	–0.50	1.11	179.59
21H	191.2	209.75	18.55	0.90	1.11	188.96
22H	200.7	220.10	19.40	0.85	1.11	198.29
23H	210.2	231.15	20.95	1.55	1.11	208.24
24H	219.7	242.20	22.50	1.55	1.11	218.20
25H	229.2	253.45	24.25	1.75	1.11	228.33
26H	238.7	264.35	25.65	1.40	1.11	238.15
202-1240C-						
1H	2.2	2.85	0.65	0.65	1.11	2.57
2H	11.7	12.05	0.35	–0.30	1.11	10.86
3H	21.2	22.85	1.65	1.30	1.11	20.59
4H	32.7	34.60	1.90	0.25	1.11	31.17
5H	42.2	46.05	3.85	1.95	1.11	41.49
6H	51.7	55.90	4.20	0.35	1.11	50.36
7H	61.2	67.10	5.90	1.70	1.11	60.45
8H	70.7	77.40	6.70	0.80	1.11	69.73

Table T2 (continued).

Core	Depth of core top		Depth offset		Translation to cmcd	
	Drillers (mbsf)	Composite (mcd)	Cumulative (m)	Differential (m)	Growth factor*	Depth (cmcd)†
202-1240D-						
D-1H	3.2	4.85	1.65	1.65	1.11	4.37
D-2H	12.7	14.30	1.60	–0.05	1.11	12.88
D-3H	22.2	26.00	3.80	2.20	1.11	23.42

Notes: * = calculated based on mbsf-mcd relationship for splice shown in Figure F11, p. 36. † = within the splice, the following equations apply: cmcd (mcd/growth factor), mcd = mbsf + cumulative depth offset, mcd = cmcd × growth factor, mbsf = cmcd × growth factor – cumulative offset. This table is also available in ASCII.

Table T3. Splice tie points, Site 1240.

Hole, core, section, interval (cm)	Depth (mbsf)	Depth (mcd)	Depth (cmcd)		Hole, core, section, interval (cm)	Depth (mbsf)	Depth (mcd)	Depth (cmcd)
202-					202-			
1240B-1H-4, 140	5.90	5.90	5.32	Tie to	1240C-1H-3, 5	5.25	5.90	5.32
1240C-1H-6, 75	10.45	11.10	10.00	Tie to	1240B-2H-1, 55	9.25	11.10	10.00
1240B-2H-3, 30	12.00	13.85	12.48	Tie to	1240C-2H-2, 30	13.50	13.85	12.48
1240C-2H-4, 105	17.25	17.60	15.86	Tie to	1240D-2H-3, 30	16.00	17.60	15.86
1240D-2H-5, 10	18.80	20.40	18.38	Tie to	1240B-3H-1, 85	19.05	20.40	18.38
1240B-3H-5, 130	25.50	26.85	24.19	Tie to	1240D-3H-1, 85	23.05	26.85	24.19
1240D-3H-5, 130	29.50	33.30	30.00	Tie to	1240B-4H-3, 50	31.20	33.30	30.00
1240B-4H-6, 145	36.65	38.75	34.91	Tie to	1240C-4H-3, 115	36.85	38.75	34.91
1240C-4H-5, 75	39.45	41.35	37.25	Tie to	1240B-5H-1, 120	38.40	41.35	37.25
1240B-5H-6, 5	44.75	47.70	42.97	Tie to	1240C-5H-2, 15	43.85	47.70	42.97
1240C-5H-5, 145	49.65	53.50	48.20	Tie to	1240B-6H-3, 135	51.05	53.50	48.20
1240B-6H-7, 15	55.85	58.30	52.52	Tie to	1240C-6H-2, 90	54.10	58.30	52.52
1240C-6H-5, 145	59.15	63.35	57.07	Tie to	1240B-7H-3, 100	60.20	63.35	57.07
1240B-7H-6, 100	64.70	67.85	61.13	Tie to	1240C-7H-1, 75	61.95	67.85	61.13
1240C-7H-6, 110	69.80	75.70	68.20	Tie to	1240B-8H-3, 130	70.00	75.70	68.20
1240B-8H-6, 90	74.10	79.80	71.89	Tie to	1240C-8H-2, 90	73.10	79.80	71.89
1240C-8H-6, 75	78.95	85.65	77.16	Tie to	1240B-9H-2, 5	78.75	85.65	77.16
1240B-9H-5, 125	84.45	91.35	82.30	Tie to	1240A-10H-2, 45	81.45	91.35	82.30
1240A-10H-5, 55	86.05	95.95	86.44	Tie to	1240B-10H-2, 25	88.45	95.95	86.44
1240B-10H-5, 135	94.05	101.55	91.49	Tie to	1240A-11H-2, 100	91.38	101.55	91.49
1240A-11H-6, 10	96.48	106.65	96.08	Tie to	1240B-11H-2, 10	97.80	106.65	96.08
1240B-11H-5, 145	103.65	112.50	101.35	Tie to	1240A-12H-2, 5	100.05	112.50	101.35
1240A-12H-6, 5	106.05	118.50	106.76	Tie to	1240B-12H-2, 35	107.55	118.50	106.76
1240B-12H-5, 50	112.20	123.15	110.95	Tie to	1240A-13H-2, 80	110.30	123.15	110.95
1240A-13H-6, 135	116.85	129.70	116.85	Tie to	1240B-13H-1, 125	116.45	129.70	116.85
1240B-13H-4, 90	120.60	133.85	120.59	Tie to	1240A-14H-3, 20	120.70	133.85	120.59
1240A-14H-6, 135	126.35	139.50	125.68	Tie to	1240B-14H-1, 110	125.80	139.50	125.68
1240B-14H-4, 85	130.05	143.75	129.50	Tie to	1240A-15H-2, 25	128.75	143.75	129.50
1240A-15H-6, 95	135.45	150.45	135.54	Tie to	1240B-15H-1, 135	135.55	150.45	135.54
1240B-15H-6, 110	142.80	157.70	142.07	Tie to	1240A-16H-4, 17.5	141.20	157.70	142.07
1240A-16H-6, 105	145.05	161.55	145.54	Tie to	1240B-16H-2, 15	145.35	161.55	145.54
1240B-16H-5, 40	150.10	166.30	149.82	Tie to	1240A-17H-2, 75	148.25	166.30	149.82
1240A-17H-6, 65	154.15	172.20	155.14	Tie to	1240B-17H-2, 50	155.20	172.20	155.14
1240B-17H-4, 110	158.80	175.80	158.38	Tie to	1240A-18H-1, 135	156.85	175.80	158.38
1240A-18H-6, 70	163.70	182.65	164.55	Tie to	1240B-18H-2, 25	164.45	182.65	164.55
1240B-18H-5, 40	169.10	187.30	168.74	Tie to	1240A-19H-2, 45	166.95	187.30	168.74
1240A-19H-5, 90	171.90	192.25	173.20	Tie to	1240B-19H-2, 40	174.10	192.25	173.20
1240B-19H-6, 105	180.75	198.90	179.19	Tie to	1240A-20H-2, 145	177.45	198.90	179.19
1240A-20H-5, 125	181.75	203.20	183.06	Tie to	1240B-20H-3, 85	185.55	203.20	183.06
1240B-20H-5, 110	188.80	206.45	185.99	Tie to	1240A-21H-1, 92.5	184.95	206.45	185.99
1240A-21H-6, 65	192.15	213.65	192.48	Tie to	1240B-21H-3, 90	195.10	213.65	192.48
1240B-21H-6, 50	199.20	217.75	196.17	Tie to	1240A-22H-2, 130	196.30	217.75	196.17
1240A-22H-5, 70	200.20	221.65	199.68	Tie to	1240B-22H-2, 5	202.25	221.65	199.68
1240B-22H-6, 75	208.95	228.35	205.72	Tie to	1240A-23H-3, 5	206.05	228.35	205.72
1240A-23H-6, 20	210.70	233.00	209.91	Tie to	1240B-23H-2, 35	212.05	233.00	209.91
1240B-23H-5, 75	216.95	237.90	214.32	Tie to	1240A-24H-2, 45	214.45	237.90	214.32
1240A-24H-6, 130	221.30	244.75	220.50	Tie to	1240B-24H-2, 105	222.25	244.75	220.50
1240B-24H-5, 105	226.75	249.25	224.55	Tie to	1240A-25H-2, 65	224.15	249.25	224.55
1240A-25H-6, 105	230.55	255.65	230.32	Tie to	1240B-25H-2, 67.5	231.40	255.65	230.32
1240B-25H-5, 50	235.70	259.95	234.19	Tie to	1240A-26H-2, 15	233.15	259.95	234.19
1240A-26H-6, 20	239.20	266.00	239.64	Tie to	1240B-26H-2, 15	240.35	266.00	239.64
1240B-26H-6, 5	246.25	271.90	244.95	Tie to	1240A-27H-3, 40	244.40	271.90	244.95
1240A-27H-7, 75	250.75	278.25	250.68					

Note: This table is also available in **ASCII.**

Table T4. OSUS-MS measurements, Hole 1240A.

Core, section, interval (cm)	Depth (mbsf)	Depth (mcd)	Magnetic susceptibility (instrument units)	Run number	Depth from top of core (cm)
202-1240A-					
1H-1, 5	0.05	0.05	4.8	1826	5
1H-1, 10	0.10	0.10	4.9	1826	10
1H-1, 15	0.15	0.15	4.9	1826	15
1H-1, 20	0.20	0.20	5.5	1826	20
1H-1, 25	0.25	0.25	5.5	1826	25
1H-1, 30	0.30	0.30	5.3	1826	30
1H-1, 35	0.35	0.35	4.9	1826	35
1H-1, 40	0.40	0.40	4.4	1826	40
1H-1, 45	0.45	0.45	4.1	1826	45
1H-1, 50	0.50	0.50	4.0	1826	50
1H-1, 55	0.55	0.55	4.0	1826	55
1H-1, 60	0.60	0.60	3.5	1826	60
1H-1, 65	0.65	0.65	2.9	1826	65
1H-1, 70	0.70	0.70	3.3	1826	70
1H-1, 75	0.75	0.75	2.7	1826	75
1H-1, 80	0.80	0.80	2.8	1826	80
1H-1, 85	0.85	0.85	2.6	1826	85
1H-1, 90	0.90	0.90	2.4	1826	90
1H-1, 95	0.95	0.95	1.8	1826	95
1H-1, 100	1.00	1.00	1.4	1826	100
1H-1, 105	1.05	1.05	1.4	1826	105
1H-1, 110	1.10	1.10	1.3	1826	110
1H-1, 115	1.15	1.15	1.1	1826	115
1H-1, 120	1.20	1.20	0.7	1826	120
1H-1, 125	1.25	1.25	0.7	1826	125
1H-1, 130	1.30	1.30	1.2	1826	130
1H-1, 135	1.35	1.35	0.9	1826	135
1H-1, 140	1.40	1.40	0.8	1826	140
1H-2, 5	1.56	1.56	1.7	1827	155
1H-2, 10	1.61	1.61	1.8	1827	160
1H-2, 15	1.66	1.66	1.7	1827	165
1H-2, 20	1.71	1.71	1.3	1827	170
1H-2, 25	1.76	1.76	1.3	1827	175
1H-2, 30	1.81	1.81	1.0	1827	180
1H-2, 35	1.86	1.86	1.0	1827	185
1H-2, 40	1.91	1.91	0.9	1827	190
1H-2, 45	1.96	1.96	0.7	1827	195
1H-2, 50	2.01	2.01	0.7	1827	200
1H-2, 55	2.06	2.06	0.5	1827	205
1H-2, 60	2.11	2.11	0.6	1827	210
1H-2, 65	2.16	2.16	0.5	1827	215
1H-2, 70	2.21	2.21	0.6	1827	220
1H-2, 75	2.26	2.26	0.4	1827	225
1H-2, 80	2.31	2.31	0.6	1827	230
1H-2, 85	2.36	2.36	0.5	1827	235
1H-2, 90	2.41	2.41	0.6	1827	240
1H-2, 95	2.46	2.46	0.5	1827	245
1H-2, 100	2.51	2.51	0.6	1827	250
1H-2, 105	2.56	2.56	0.5	1827	255
1H-2, 110	2.61	2.61	0.4	1827	260
1H-2, 115	2.66	2.66	0.6	1827	265
1H-2, 120	2.71	2.71	0.5	1827	270
1H-3, 5	2.87	2.87	0.8	1828	285
1H-3, 10	2.92	2.92	0.8	1828	290
1H-3, 15	2.97	2.97	0.8	1828	295
1H-3, 20	3.02	3.02	0.7	1828	300
1H-3, 25	3.07	3.07	0.8	1828	305
1H-3, 30	3.12	3.12	0.8	1828	310
1H-3, 35	3.17	3.17	0.8	1828	315
1H-3, 40	3.22	3.22	0.9	1828	320
1H-3, 45	3.27	3.27	0.8	1828	325
1H-3, 50	3.32	3.32	0.9	1828	330
1H-3, 55	3.37	3.37	0.8	1828	335

Note: Only a portion of this table appears here. The complete table is available in **ASCII**.

Table T5. OSUS-MS measurements, Hole 1240B.

Core, section, interval (cm)	Depth (mbsf)	Depth (mcd)	Magnetic susceptibility (instrument units)	Run number	Depth from top of core (cm)
202-1240B-					
1H-1, 5	0.05	0.05	5.3	1985	5
1H-1, 10	0.10	0.10	5.6	1985	10
1H-1, 15	0.15	0.15	7.2	1985	15
1H-1, 20	0.20	0.20	6.5	1985	20
1H-1, 25	0.25	0.25	6.1	1985	25
1H-1, 30	0.30	0.30	5.2	1985	30
1H-1, 35	0.35	0.35	4.7	1985	35
1H-1, 40	0.40	0.40	4.5	1985	40
1H-1, 45	0.45	0.45	4.1	1985	45
1H-1, 50	0.50	0.50	4.2	1985	50
1H-1, 55	0.55	0.55	4.2	1985	55
1H-1, 60	0.60	0.60	3.9	1985	60
1H-1, 65	0.65	0.65	3.4	1985	65
1H-1, 70	0.70	0.70	2.5	1985	70
1H-1, 75	0.75	0.75	2.4	1985	75
1H-1, 80	0.80	0.80	2.8	1985	80
1H-1, 85	0.85	0.85	2.1	1985	85
1H-1, 90	0.90	0.90	1.6	1985	90
1H-1, 95	0.95	0.95	1.1	1985	95
1H-1, 100	1.00	1.00	0.6	1985	100
1H-1, 105	1.05	1.05	0.3	1985	105
1H-1, 110	1.10	1.10	0.3	1985	110
1H-1, 115	1.15	1.15	0.5	1985	115
1H-1, 120	1.20	1.20	0.4	1985	120
1H-1, 125	1.25	1.25	0.6	1985	125
1H-1, 130	1.30	1.30	0.5	1985	130
1H-1, 135	1.35	1.35	0.5	1985	135
1H-1, 140	1.40	1.40	0.4	1985	140
1H-1, 145	1.45	1.45	0.2	1985	145
1H-2, 5	1.56	1.56	0.7	1986	155
1H-2, 10	1.61	1.61	0.6	1986	160
1H-2, 15	1.66	1.66	0.6	1986	165
1H-2, 20	1.71	1.71	0.5	1986	170
1H-2, 25	1.76	1.76	0.4	1986	175
1H-2, 30	1.81	1.81	0.2	1986	180
1H-2, 35	1.86	1.86	0.2	1986	185
1H-2, 40	1.91	1.91	0.2	1986	190
1H-2, 45	1.96	1.96	0.3	1986	195
1H-2, 50	2.01	2.01	0.3	1986	200
1H-2, 55	2.06	2.06	0.3	1986	205
1H-2, 60	2.11	2.11	0.3	1986	210
1H-2, 65	2.16	2.16	0.3	1986	215
1H-2, 70	2.21	2.21	0.2	1986	220
1H-2, 75	2.26	2.26	0.2	1986	225
1H-2, 80	2.31	2.31	0.2	1986	230
1H-2, 85	2.36	2.36	0.3	1986	235
1H-2, 90	2.41	2.41	0.3	1986	240
1H-2, 95	2.46	2.46	0.3	1986	245
1H-2, 100	2.51	2.51	0.3	1986	250
1H-2, 105	2.56	2.56	0.2	1986	255
1H-2, 110	2.61	2.61	0.2	1986	260
1H-2, 115	2.66	2.66	0.1	1986	265
1H-2, 120	2.71	2.71	0.0	1986	270
1H-2, 125	2.76	2.76	0.0	1986	275
1H-2, 130	2.81	2.81	0.0	1986	280
1H-2, 135	2.86	2.86	0.1	1986	285
1H-2, 140	2.91	2.91	0.0	1986	290
1H-2, 145	2.96	2.96	0.0	1986	295
1H-3, 5	3.07	3.07	0.6	1987	305
1H-3, 10	3.12	3.12	0.7	1987	310
1H-3, 15	3.17	3.17	0.7	1987	315
1H-3, 20	3.22	3.22	0.8	1987	320
1H-3, 25	3.27	3.27	0.7	1987	325

Note: Only a portion of this table appears here. The complete table is available in ASCII.

Table T6. OSUS-MS measurements, Hole 1240C.

Core, section, interval (cm)	Depth (mbsf)	Depth (mcd)	Magnetic susceptibility (instrument units)	Run number	Depth from top of core (cm)
202-1240C-					
1H-1, 5	2.25	2.90	0.9	2171	5
1H-1, 10	2.30	2.95	0.8	2171	10
1H-1, 15	2.35	3.00	0.7	2171	15
1H-1, 20	2.40	3.05	0.7	2171	20
1H-1, 25	2.45	3.10	0.7	2171	25
1H-1, 30	2.50	3.15	0.7	2171	30
1H-1, 35	2.55	3.20	0.7	2171	35
1H-1, 40	2.60	3.25	0.9	2171	40
1H-1, 45	2.65	3.30	0.7	2171	45
1H-1, 50	2.70	3.35	0.6	2171	50
1H-1, 55	2.75	3.40	0.7	2171	55
1H-1, 60	2.80	3.45	0.6	2171	60
1H-1, 65	2.85	3.50	0.5	2171	65
1H-1, 70	2.90	3.55	0.6	2171	70
1H-1, 75	2.95	3.60	0.7	2171	75
1H-1, 80	3.00	3.65	0.7	2171	80
1H-1, 85	3.05	3.70	0.7	2171	85
1H-1, 90	3.10	3.75	0.5	2171	90
1H-1, 95	3.15	3.80	0.6	2171	95
1H-1, 100	3.20	3.85	0.6	2171	100
1H-1, 105	3.25	3.90	0.6	2171	105
1H-1, 110	3.30	3.95	0.6	2171	110
1H-1, 115	3.35	4.00	0.6	2171	115
1H-1, 120	3.40	4.05	0.7	2171	120
1H-1, 125	3.45	4.10	0.7	2171	125
1H-1, 130	3.50	4.15	0.7	2171	130
1H-1, 135	3.55	4.20	0.7	2171	135
1H-1, 140	3.60	4.25	0.7	2171	140
1H-1, 145	3.65	4.30	0.7	2171	145
1H-2, 5	3.76	4.41	0.7	2172	155
1H-2, 10	3.81	4.46	0.8	2172	160
1H-2, 15	3.86	4.51	0.8	2172	165
1H-2, 20	3.91	4.56	0.9	2172	170
1H-2, 25	3.96	4.61	1.0	2172	175
1H-2, 30	4.01	4.66	0.8	2172	180
1H-2, 35	4.06	4.71	0.7	2172	185
1H-2, 40	4.11	4.76	0.7	2172	190
1H-2, 45	4.16	4.81	0.9	2172	195
1H-2, 50	4.21	4.86	1.0	2172	200
1H-2, 55	4.26	4.91	1.1	2172	205
1H-2, 60	4.31	4.96	1.1	2172	210
1H-2, 65	4.36	5.01	1.0	2172	215
1H-2, 70	4.41	5.06	1.3	2172	220
1H-2, 75	4.46	5.11	1.4	2172	225
1H-2, 80	4.51	5.16	1.4	2172	230
1H-2, 85	4.56	5.21	1.2	2172	235
1H-2, 90	4.61	5.26	1.2	2172	240
1H-2, 95	4.66	5.31	1.1	2172	245
1H-2, 100	4.71	5.36	1.1	2172	250
1H-2, 105	4.76	5.41	1.1	2172	255
1H-2, 110	4.81	5.46	1.0	2172	260
1H-2, 115	4.86	5.51	0.9	2172	265
1H-2, 120	4.91	5.56	0.7	2172	270
1H-2, 125	4.96	5.61	0.6	2172	275
1H-2, 130	5.01	5.66	0.5	2172	280
1H-2, 135	5.06	5.71	0.6	2172	285
1H-2, 140	5.11	5.76	0.4	2172	290
1H-2, 145	5.16	5.81	0.3	2172	295
1H-3, 5	5.27	5.92	0.5	2173	305
1H-3, 10	5.32	5.97	0.5	2173	310
1H-3, 15	5.37	6.02	0.5	2173	315
1H-3, 20	5.42	6.07	0.5	2173	320
1H-3, 25	5.47	6.12	0.8	2173	325

Note: Only a portion of this table appears here. The complete table is available in **ASCII**.

Table T7. OSUS-MS measurements, Hole 1240D.

Core, section, interval (cm)	Depth (mbsf)	Depth (mcd)	Magnetic susceptibility (instrument units)	Run number	Depth from top of core (cm)
202-1240D-					
1H-1, 5	3.25	4.90	0.5	2180	5
1H-1, 10	3.30	4.95	0.5	2180	10
1H-1, 15	3.35	5.00	0.6	2180	15
1H-1, 20	3.40	5.05	0.8	2180	20
1H-1, 25	3.45	5.10	0.6	2180	25
1H-1, 30	3.50	5.15	0.7	2180	30
1H-1, 35	3.55	5.20	0.7	2180	35
1H-1, 40	3.60	5.25	0.9	2180	40
1H-1, 45	3.65	5.30	0.9	2180	45
1H-1, 50	3.70	5.35	0.7	2180	50
1H-1, 55	3.75	5.40	0.6	2180	55
1H-1, 60	3.80	5.45	0.4	2180	60
1H-1, 65	3.85	5.50	0.6	2180	65
1H-1, 70	3.90	5.55	-0.2	2180	70
1H-1, 75	3.95	5.60	0.6	2180	75
1H-1, 80	4.00	5.65	0.7	2180	80
1H-1, 85	4.05	5.70	0.6	2180	85
1H-1, 90	4.10	5.75	0.6	2180	90
1H-1, 95	4.15	5.80	0.7	2180	95
1H-1, 100	4.20	5.85	0.7	2180	100
1H-1, 105	4.25	5.90	0.7	2180	105
1H-1, 110	4.30	5.95	0.7	2180	110
1H-1, 115	4.35	6.00	0.7	2180	115
1H-1, 120	4.40	6.05	0.6	2180	120
1H-1, 125	4.45	6.10	0.8	2180	125
1H-1, 130	4.50	6.15	0.8	2180	130
1H-1, 135	4.55	6.20	0.4	2180	135
1H-1, 140	4.60	6.25	0.4	2180	140
1H-1, 145	4.65	6.30	0.3	2180	145
1H-2, 5	4.75	6.40	1.2	2181	155
1H-2, 10	4.80	6.45	1.1	2181	160
1H-2, 15	4.85	6.50	0.9	2181	165
1H-2, 20	4.90	6.55	0.8	2181	170
1H-2, 25	4.95	6.60	0.7	2181	175
1H-2, 30	5.00	6.65	0.7	2181	180
1H-2, 35	5.05	6.70	0.7	2181	185
1H-2, 40	5.10	6.75	0.6	2181	190
1H-2, 45	5.15	6.80	0.6	2181	195
1H-2, 50	5.20	6.85	0.5	2181	200
1H-2, 55	5.25	6.90	0.6	2181	205
1H-2, 60	5.30	6.95	0.4	2181	210
1H-2, 65	5.35	7.00	0.2	2181	215
1H-2, 70	5.40	7.05	0.3	2181	220
1H-2, 75	5.45	7.10	0.2	2181	225
1H-2, 80	5.50	7.15	0.1	2181	230
1H-2, 85	5.55	7.20	0.2	2181	235
1H-2, 90	5.60	7.25	-0.1	2181	240
1H-2, 95	5.65	7.30	-0.1	2181	245
1H-2, 100	5.70	7.35	-0.1	2181	250
1H-2, 105	5.75	7.40	0.1	2181	255
1H-2, 110	5.80	7.45	0.0	2181	260
1H-2, 115	5.85	7.50	-0.1	2181	265
1H-2, 120	5.90	7.55	0.0	2181	270
1H-2, 125	5.95	7.60	0.0	2181	275
1H-2, 130	6.00	7.65	-0.2	2181	280
1H-2, 135	6.05	7.70	-0.3	2181	285
1H-2, 140	6.10	7.75	-0.4	2181	290
1H-2, 145	6.15	7.80	-0.4	2181	295
1H-3, 5	6.25	7.90	0.3	2182	304
1H-3, 10	6.30	7.95	0.3	2182	309
1H-3, 15	6.35	8.00	0.3	2182	314
1H-3, 20	6.40	8.05	0.3	2182	319
1H-3, 25	6.45	8.10	0.3	2182	324

Note: Only a portion of this table appears here. The complete table is available in **ASCII**.

Table T8. Lithologic Unit I, Site 1240.

Unit/ Subunit	Top			Base			Description	Interpretation
	Core, section, interval (cm)	Depth (mbsf)	Depth (mcd)	Core, section, interval (cm)	Depth (mbsf)	Depth (mcd)		
	202-			202-				
IA	1240A-1H-1, 0	0.00	0.00	1240A-15H-1, 20	127.20	142.20	Nannofossil ooze, often rich in diatoms and occasionally containing clay or foraminifers	Moderately productive pelagic setting
	1240B-1H-1, 0	0.00	0.00	1240B-14H-3, 80	128.50	142.20		
	1240C-1H-1, 0	2.20	2.85	1240C-8H-CC, 16	80.60	87.30		
	1240D-1H-1, 0	3.20	4.85	1240D-3H-CC, 19	31.59	35.39		
IB	1240A-15H-1, 20	127.20	142.20	1240A-21H-1, 90	184.90	206.40	Biogenic oozes, rich in nannofossils and diatoms, some containing clay minerals	Moderately productive pelagic setting with eolian terrigenous input
	1240B-14H-3, 80	128.50	142.20	1240B-20H-5, 105	188.75	206.40		
IC	1240A-21H-1, 90	184.90	206.40	1240A-28H-CC, 9	254.38	282.93	Nannofossil ooze, rich in diatoms	Moderately productive pelagic setting
	1240B-20H-5, 105	188.75	206.40	1240B-26H-CC, 33	248.81	274.46		

Table T9. Ash layers, Site 1240.

Number	Core, section, interval (cm)	Top depth (mbsf)	Top depth (mcd)	Top depth (cm)	Base depth (mbsf)	Base depth (mcd)	Core, section, interval (cm)	Top depth (mbsf)	Top depth (mcd)	Top depth (cm)	Base depth (mbsf)	Base depth (mcd)	Core, section, interval (cm)	Top depth (mbsf)	Top depth (mcd)	Top depth (cm)	Base depth (mbsf)	Base depth (mcd)
	202-1240A-						202-1240B-						202-1240C-					
1	Core gap						**3H-5, 12**	**24.34**	**25.69**	**14**	**24.36**	**25.71**	**3H-2, 133**	**24.04**	**25.69**	**136**	**24.07**	**25.72**
Wash	4H-1, 32	22.82	26.92	33	22.83	26.93												
2	5H-2, 93	34.43	39.73	100	34.50	39.80	Core gap						NF					
3	**12H-2, 28**	**100.28**	**112.73**	**35**	**100.35**	**112.80**	**11H-6, 15**	**103.86**	**112.71**	**20**	**103.91**	**112.76**						
4	**22H-6, 104**	**202.08**	**223.53**	**106**	**202.10**	**223.55**	**22H-3, 41**	**204.13**	**223.53**	**44**	**204.16**	**223.56**						
5	**25H-2, 85**	**224.36**	**249.46**	**93**	**224.44**	**249.54**	**24H-5, 129**	**227.03**	**249.53**	**135**	**227.09**	**249.59**						
6	25H-4, 78	227.31	252.41	88	227.41	252.51	Core gap											
7	**26H-7, 67**	**241.23**	**268.03**	**76**	**241.32**	**268.12**	**26H-3, 55**	**242.26**	**267.91**	**67**	**242.38**	**268.03**						
8	28H-1, 88	251.38	279.93	91	251.41	279.96	ND											

Notes: Ash layers that could be correlated between holes are located in the same row and printed in bold type. ND = not drilled, NF = not found.

Table T10. Age-depth control points, Hole 1240A.

Datum	Source	Age (Ma) Minimum	Age (Ma) Maximum	Top sample (FO presence/LO absence) Core, section, interval (cm)	Top sample (FO presence/LO absence) Depth (mbsf)	Bottom sample (LO presence/FO absence) Core, section, interval (cm)	Bottom sample (LO presence/FO absence) Depth (mbsf)	Age (Ma) Average	Age (Ma) Uncertainty (±)	Depth Average (mbsf)	Depth Average (mcd)	Depth Uncertainty (±m)
				202-1240A-		202-1240A-						
Start of *Emiliania huxleyi* acme	CN	0.08	0.08	2H-2, 75	5.76	2H-3, 75	7.27	0.08	0.00	6.52	7.87	0.76
LO *Globigerinoides ruber* pink	PF	0.12	0.12	2H-CC, 14	12.62	3H-CC, 11	22.84	0.12	0.00	17.73	19.38	5.11
FO *Emiliania huxleyi*	CN	0.26	0.26	3H-3, 75	16.77	3H-4, 75	18.27	0.26	0.00	17.52	19.47	0.75
FO *Globigerinoides ruber* pink	PF	0.40	0.40	5H-CC, 15	41.92	6H-CC, 11	51.33	0.40	0.00	46.63	53.48	4.71
LO *Pseudoemiliania lacunosa*	CN	0.46	0.46	5H-3, 75	35.76	5H-4, 75	37.27	0.46	0.00	36.52	41.82	0.76
LO *Nitzschia reinholdii*	D	0.62	0.62	4H-CC, 8	32.27	5H-CC, 15	41.92	0.62	0.00	37.10	41.80	4.83
LO *Globorotalia tosaensis*	PF	0.65	0.65	5H-CC, 15	41.92	6H-CC, 11	51.33	0.65	0.00	46.63	53.48	4.71
LO *Nitzschia fossilis*	D	0.70	0.70	7H-4, 75	56.28	7H-5, 75	57.79	0.70	0.00	57.04	64.49	0.75
LO *Reticulofenestra asanoi*	CN	0.88	0.88	8H-CC, 14	70.21	9H-1, 75	70.75	0.88	0.00	70.48	80.23	0.27
Reentry medium *Gephyrocapsa*	CN	1.02	1.02	9H-7, 40	79.44	9H-CC, 14	79.97	1.02	0.00	79.71	88.86	0.27
FO *Reticulofenestra asanoi*	CN	1.08	1.08	10H-CC, 9	88.73	11H-1, 75	89.75	1.08	0.00	89.24	99.28	0.51
LO *Rhizosolenia matuyamai*	D	1.05	1.05	9H-4, 75	75.27	9H-5, 75	76.78	1.05	0.00	76.03	85.18	0.76
FO *Rhizosolenia matuyamai*	D	1.18	1.18	11H-2, 75	91.13	11H-3, 75	92.64	1.18	0.00	91.89	102.06	0.75
LO *Gephyrocapsa* (large)	CN	1.24	1.24	11H-7, 40	98.33	11H-CC, 8	98.82	1.24	0.00	98.58	108.75	0.24
FO *Gephyrocapsa* (large)	CN	1.45	1.45	13H-1, 75	108.75	13H-2, 75	110.25	1.45	0.00	109.50	122.35	0.75
LO *Calcidiscus macintyrei*	CN	1.59	1.59	14H-5, 75	124.27	14H-6, 75	125.78	1.59	0.00	125.03	138.18	0.76
FO *Gephyrocapsa* (medium)	CN	1.67	1.67	14H-7, 40	126.94	14H- CC, 18	127.45	1.67	0.00	127.20	140.35	0.25
LO *Rhizosolenia praebergonii* v. *robusta*	D	1.73	1.73	14H-CC, 18	127.45	15H-1, 10	127.10	1.73	0.00	127.28	141.35	–0.17
LO *Globigerinoides extremus*	PF	1.77	1.77	13H-CC, 18	117.95	14H-CC, 18	127.45	1.77	0.00	122.70	141.35	4.75
LO *Discoaster brouweri*	CN	1.96	1.96	19H-CC, 20	174.89	20H-CC, 22	184.47	1.96	0.00	179.68	200.58	4.79
FO *Fragilariopsis doliolus*	D	2.00	2.00	19H-6, 75	173.29	19H-7, 40	174.45	2.00	0.00	173.87	194.22	0.58
LO *Globorotalia exilis*	PF	2.15	2.15	19H-CC, 20	174.89	20H-CC, 22	184.47	2.15	0.00	179.68	200.58	4.79
LO *Globorotalia pseudomiocenica*	PF	2.30	2.30	22H-CC, 20	203.52	23H-CC, 20	213.01	2.30	0.00	208.27	230.14	4.74
LO *Globorotalia limbata*	PF	2.38	2.38	22H-CC, 20	203.52	23H-CC, 20	213.01	2.38	0.00	208.27	230.14	4.74
LO *Globorotalia puncticulata*	PF	2.40	2.40	23H-CC, 20	213.01	24H-CC, 8	222.43	2.40	0.00	217.72	240.60	4.71
LO *Thalassiosira convexa* s.l.	D	2.41	2.41	22H-4, 75	198.77	22H-5, 75	200.28	2.41	0.00	199.53	220.98	0.75
LO *Globorotalia pertenuis*	PF	2.60	2.60	24H-CC, 8	222.43	25H-CC, 21	232.08	2.60	0.00	227.26	251.53	4.82
LO *Discoaster surculus*	CN	2.61	2.61	28H-3, 40	253.92	28H-CC, 0	254.29	2.61	0.00	254.11	282.66	0.19

Notes: FO = first occurrence, LO = last occurrence. CN = calcareous nannofossils, PF = planktonic foraminifers, D = diatoms.

Table T11. Distribution of calcareous nannofossils, Hole 1240A. (**See table notes.** Continued on next page.)

Core, section, interval (cm)	Depth (mbsf)	Depth (mcd)	Preservation	Abundance	*Calcidiscus macintyrei*	*Discoaster brouweri*	*Discoaster pentaradiatus*	*Discoaster surculus*	*Discoaster tamalis*	*Discoaster variabilis* gr.	*Emiliania huxleyi*	*Gephyrocapsa* spp. (large)	*Gephyrocapsa* spp. (medium)	*Gephyrocapsa* spp. (small)	*Helicosphaera sellii*	*Pseudoemiliania lacunosa*	*Reticulofenestra asanoi*	*Reticulofenestra pseudoumbilicus* >7 µm	*Reticulofenestra* spp. <7 µm	*Sphenolithus abies/neoabies*
202-1240A-																				
1H-1, 0	0.00	0.00	G	A							A		F	A						
1H-CC, 11	3.52	3.52	G	A							A		C	C						
2H-2, 75	5.76	7.11	G	A							C		C	A						
2H-3, 75	7.27	8.62	G	A							R		C	A						
2H-CC, 14	12.62	13.97	G	A							R		C	A						
3H-3, 75	16.77	18.72	M	A							R		A	A						
3H-4, 75	18.27	20.22	M	A									A	A						
3H-6, 75	21.29	23.24	M	A									A	A						
3H-CC, 14	22.87	24.82	M	A									A	A						
4H-CC, 8	32.27	36.37	G	A									F	A						
5H-3, 75	35.76	41.06	M	A									F	A						
5H-4, 75	37.27	42.57	M	A									F	A						
5H-5, 75	38.77	44.07	M	A									F	A		R				
5H-6, 75	40.28	45.58	M	A									F	A		F				
5H-CC, 15	41.92	47.22	M	A									F	A		C				
6H-CC, 11	51.33	59.73	G	A									A	A		C				
7H-CC, 22	60.95	68.40	G	A									A	A		C				
8H-CC, 14	70.21	80.55	G	A									C	A		C				
9H-1, 75	70.75	79.90	G	A									A	A			F			
9H-2, 75	72.25	81.40	G	A									A	A			C			
9H-4, 75	75.27	84.42	G	A									A	A			F			
9H-6, 75	78.29	87.44	G	A									A	A						
9H-7, 40	79.44	88.59	G	A										A						
9H-CC, 14	79.97	89.12	G	A										A		C	F			
10H-5, 75	86.27	96.17	G	A										A		C	F			
10H-7, 40	88.43	98.33	G	A										A		C	F			
10H-CC, 9	88.73	98.63	G	A										A		C	F			
11H-1, 75	89.75	99.92	G	A										A		F				
11H-2, 75	91.13	101.30	G	A										A		F				
11H-4, 75	94.15	104.32	G	A										A		F				
11H-6, 75	97.17	107.34	G	A										A		F				
11H-7, 40	98.33	108.50	G	A										A		F				
11H-CC, 8	98.82	108.99	G	A								F	C	A		F				
12H-CC, 14	108.09	120.54	M	A								C	C	A		F				R
13H-1, 75	108.75	121.60	M	A								F	C	A		F				
13H-2, 75	110.25	123.10	M	A									C	A		F				
13H-4, 75	113.26	126.11	M	A									C	A		F				
13H-CC, 17	117.95	130.80	M	A		R							C	A		F				
14H-3, 75	121.26	134.41	M	A									C	A		F				
14H-4, 75	122.76	135.91	M	A									C	A		F				
14H-5, 75	124.27	137.42	M	A	R								F	A		F				
14H-6, 75	125.78	138.93	M	A	R								F	A		F				
14H-7, 40	126.94	140.09	M	A	R								F	A		F				
14H-CC, 18	127.45	140.60	M	A	R									A	R	C				
15H-CC, 21	136.94	151.94	M	A	F	R								A		F				
16H-CC, 34	146.53	163.03	M	A	R	R	R							A	F	F		R		R
17H-CC, 21	155.99	174.04	M	A	R	R								A	F	F		R		R
18H-CC, 40	165.58	184.54	M	A	R	R		R						A	R	R				
19H-CC, 20	174.84	195.24	M	A	R									A	R	C			C	
20H-CC, 22	184.40	205.92	M	A	F	R								R	R	C			C	F
21H-4, 75	189.25	210.76	M	A		R								A	R	C			A	
21H-5, 75	190.75	212.27	M	A		R								C	R	C			C	
21H-6, 75	192.25	213.78	M	A		F								C	R	C			C	
21H-7, 40	193.40	214.94	M	A		F								C	R	C			C	
21H-CC, 12	193.74	215.29	M	A		F		R						A	R	C			A	R

Table T11 (continued).

Core, section, interval (cm)	Depth (mbsf)	Depth (mcd)	Preservation	Abundance	*Calcidiscus macintyrei*	*Discoaster brouweri*	*Discoaster pentaradiatus*	*Discoaster surculus*	*Discoaster tamalis*	*Discoaster variabilis* gr.	*Emiliania huxleyi*	*Gephyrocapsa* spp. (large)	*Gephyrocapsa* spp. (medium)	*Gephyrocapsa* spp. (small)	*Helicosphaera sellii*	*Pseudoemiliania lacunosa*	*Reticulofenestra asanoi*	*Reticulofenestra pseudoumbilicus* >7 µm	*Reticulofenestra* spp. <7 µm	*Sphenolithus abies/neoabies*
22H-CC, 20	203.46	224.97	M	A		F								C	R	F			C	
23H-CC, 20	212.96	235.31	M	A		F	R							C	R	C			C	R
24H-CC, 8	222.36	245.88	M	A		F								A	F	C			A	
25H-CC, 21	232.01	257.18	M	A		F	R							C	F	C			A	
26H-CC, 20	241.47	268.35	M	A		F								C	F	F		F	A	R
27H-CC, 31	251.09	278.67	M	A		F			R					A	F	C			A	R
28H-1, 75	251.25	279.80	M	A		F	R							C						
28H-2, 75	252.75	281.31	M	A		F								C						
28H-3, 40	253.90	282.47	M	A		F		R						C						
28H-CC, 0	254.27	282.84	M	A		F		R						C				R	A	

Notes: Preservation: G = good, M = moderate. Abundance: A = abundant, C = common, F = few, R = rare.

Table T12. Distribution of planktonic foraminifers, Hole 1240A.

Core, section, interval top (cm)	Depth (mbsf)	Depth (mcd)	Preparation	Preservation	Abundance	Benthic/planktonic foraminifers (%)	Remarks	*Globigerinoides rubescens*	*Globigerinella aequilateris*	*Globigerinoides extremus*	*Globigerinoides obliquus*	*Globigerinoides ruber*	*Globigerinoides ruber* pink	*Globigerinoides trilobus*	*Globorotalia crassaformis*	*Globorotalia crassula*	*Globorotalia exilis*	*Globorotalia hirsuta*	*Globorotalia inflata*	*Globorotalia limbata*	*Globorotalia menardii*	*Globorotalia pertenuis*	*Globorotalia pseudomiocenica*	*Globorotalia puncticulata*	*Globorotalia sacculifer*	*Globorotalia scitula*	*Globorotalia tosaensis*	*Globorotalia truncatulinoides*	*Globorotalia tumida*	*Globorotalia ungulata*	*Neogloboquadrina acostaensis*	*Neogloboquadrina dutertrei*	*Neogloboquadrina pachyderma*	*Orbulina universa*	*Pulleniatina obliquiloculata*	*Pulleniatina praecursor*	*Sphaeroidinella dehiscens*
202-1240A-																																				
Mudline	0.00	0.00	S	P	C	1/99	Radiolarians: F		F			F							R		F				R				R		F	F	R	F		
1H-CC, 11	3.52	3.52	S	P/M	C	1/99	Radiolarians: F		F			F							F		C				F				R		C	F	F	F		
2H-CC, 14	12.62	13.97	S	M	C	1/99	Radiolarians: C; Diatoms: F		F			F									C				F	F			R	F	C	F	F	C		R
3H-CC, 11	22.87	24.82	S	M	C	1/99	Radiolarians: F	F	F				C					F			C				F	F				F	C	F	F	F		
4H-CC, 8	32.27	36.37	S	M/G	C	1/99	Radiolarians: F	F					C					F			F				F	F					C	F	F	F		
5H-CC, 15	41.92	47.22	S	M	C	1/99	Radiolarians: F		F			R	F					F			C				F				C		C	F	F			R
6H-CC, 11	51.33	59.73	S	M	C	1/99	Radiolarians: F					F		F		F		F			F				F	F		F	F	R		C	F	F	F		
7H-CC, 22	60.95	68.40	S	M	F/C	1/99	Radiolarians: A					F		F					R		F				F	F			F	F	F	C	F	F	F		
8H-CC, 14	70.21	80.55	S	M/G	C	1/99	Radiolarians: F					F		F							F				F	F					C	F	C	F		F
9H-CC, 14	79.97	89.12	S	M	C	1/99	Radiolarians: C		R		F	F		F							C									F	C	F	C	F		
10H-CC, 9	88.73	98.63	S	M	C	1/99	Radiolarians: A		R		F	F		F	F				F		F				F	F			F		C	F		F		
11H-CC, 8	98.82	108.99	S	M	C	1/99	Radiolarians: F					F		F							F				F		R	R	F		F	C		F	F		F
12H-CC, 14	108.09	120.54	S	M/G	C	1/99	Radiolarians: F				F			F	F						F				F	F				R	F	C		F			F
13H-CC, 17	117.95	130.80	S	M	F	1/99	Radiolarians: A							F							F				F	F	R		F		F	C		F			R
14H-CC, 18	127.45	140.60	S	M	C	1/99	Radiolarians: C			F	F			F	F						F				F	F		R			F	C		F	F		F
15H-CC, 21	136.94	151.94	S	M	F/C	1/99	Radiolarians: A							F							F				F	R	F				F	C		F	F		
16H-CC, 34	146.53	163.03	S	M	F	1/99	Radiolarians: A			F	F	F		F							F				F	R					C		F	F		R
17H-CC, 21	155.99	174.04	S	M	F	5/95	Radiolarians: A			F				F							F				F					F	C		F			F
18H-CC, 40	165.58	184.54	S	M	F	1/99	Radiolarians: A			F				F							F									F	C	R	F	F		R
19H-CC, 20	174.84	195.24	S	M	R	10/90	Sponge spicules; Radiolarians: A			F				F							F				F				F	F	F	R	F				F
20H-CC, 22	184.40	205.92	S	M	F	3/97	Radiolarians: A			F				R			F				F					R				F	F	F	F				
21H-CC, 12	193.74	215.29	S	M	F	1/99	Radiolarians: A							F	F		F				F				F	F				F	F	F	F		F	F
22H-CC, 20	203.46	224.97	S	M/G	C	1/99	Radiolarians: C			F				F		R					F				F	F				F	C	F	F			F
23H-CC, 20	212.96	235.31	S	M/G	C	1/99	Radiolarians: A							F		R				C	C		C		F	F			F		C		F			R
24H-CC, 8	222.36	245.88	S	M/G	C	1/99	Radiolarians: F			F	F			F						F			F	R		F					C		F			F
25H-CC, 21	232.01	257.18	S	M	C	1/99	Radiolarians: C			F	F			F						F		F	F			F			F		C		F			F
26H-CC, 20	241.47	268.35	S	M/G	C	1/99	Radiolarians: F–C			F				F			F			F			F	R	R	F	R		F		C		F		R	R
27H-CC, 31	251.09	278.67	S	M/G	C	1/99	Radiolarians: C			F	F			F		R				F		F	F	R		F			F		C	F	F		F	F
28H-CC, 0	254.27	282.84	S	P/M	R	1/99	Radiolarians: R; Volcanic fragments: A							R						R				R		R				R				R			

Notes: Preparation: S = sieved. Preservation: G = good, M = moderate, P = poor. Abundance: A = abundant, C = common, F = few, R = rare.

Table T13. Distribution of diatoms, Hole 1240A. (See table notes. Continued on next page.)

Core, section, interval (cm)	Depth (mbsf)	Depth (mcd)	Identification	Method	Abundance	Preservation	*Actinocyclus ellipticus*	*Actinocyclus ellipticus* v. *lanceolata*	*Actinocyclus* spp.	*Actinoptychus senarius*	*Asteromphalus* spp.	*Azpeitia nodulifera*	*Chaetoceros* spp. (resting spores)	*Coscinodiscus* spp.	*Diploneis bombus*	*Fragilariopsis doliolus*	*Hemidiscus cuneiformis*	*Nitzschia cylindrica*	*Nitzschia marina*	*Nitzschia miocenica*	*Nitzschia reinholdii*	*Nitzschia fossilis*	*Nitzschia jousea*	*Paralia sulcata*	*Rhizosolenia* spp.	*Rhizosolenia matuyama*	*Rhizosolenia praebergonii robusta*	*Rhizosolenia praebergonii*	*Rossiela paleacea*	*Stephanopyxis* spp.	*Thalassionema* spp.	*Thalassionema convexa*	*Thalassionema convexa aspinosa*	*Thalassionema miocenica*	*Thalassionema oestrupii*	*Thalassiosira* spp.	*Thalassiothrix* spp.	Remarks
202-1240A-																																					
Mudline	0.00	0.00	PAL	S	C	M–G			R			F				F	F		F						R					F–C				F	R	F	
1H-CC, 11	3.52	3.52	PAL	S	VA	M–G			R	F	R	F		F		F	F		F	T					R					C–A				F	F	F	
2H-CC, 14	12.62	13.97	PAL	S	C–A	M–G				R	T	F				F	T		T						T					A				F–C	F	F	Reworked late Miocene forms
3H-CC, 11	22.84	24.79	PAL	S	C	M–G	T				T	F		T		F	F		T	T	T	T			F					F				F–C	R	F	Reworked late Miocene forms
4H-CC, 8	32.27	36.37	PAL	S	C	M–G				T		F		T		F	F		T			R			R					R					R	F	
5H-CC, 15	41.92	47.22	PAL	S	C–A	M–G				R				F		F			T	T		R			F	T				R				F	T	R	
6H-CC, 11	51.33	59.73	PAL	S	A	M–G				R		F		R		F	T		R			R			R	R–F				F				F		F	
7H-CC, 22	60.95	68.40	PAL	S	C–A	M–G						R		R		F	R		T		R–F	R–F			F	F				F				F		F	
8H-CC, 14	70.21	80.55	PAL	S	A	M–G			F		R	F				T	F		R–F		F	F				F	T				F				R–F		F	Reworked late Miocene forms
9H-4, 75	75.27	84.42	PAL	S	F–C	M			T		R	F				F			R			F			F					F–C				F		F–C	
9H-5, 75	76.78	85.93	PAL	S	F	M–P				R		F		T		R			R			F			R					F						F–C	Reworked late Miocene forms
9H-6, 75	78.29	87.44	PAL	S	F	M–P					R	F					F		F		F				F		R		T	F	R			F	F	F	
9H-CC, 14	79.97	89.12	PAL	S	C–A	M–G				F		F					F				F				F					C	R				F	C–A	
10H-CC, 9	88.73	98.63	PAL	S	C	M						F		R			F																		F	F	
11H-2, 75	91.13	101.30	PAL	S	C	M						F					F		F											F				F	F	F	
11H-3, 75	92.64	102.81	PAL	S	C–A	M					T	F					T		R–F	F	R–F	F			F		T			R	T		R	F		F–C	
11H-CC, 8	98.82	108.99	PAL	S	C–A	M–C																															
12H-CC, 14	108.09	120.54	PAL	S	C	M			R	F	F	F				R	F				R	F			F			F		F–C				F	F	F–C	
13H-CC, 17	117.95	130.80	PAL	S	F–C	P–M				F		F–C		R		T–R	F			T	F				F			F		F				F	F	F	Reworked late Miocene forms
14H-CC, 18	127.45	140.60	PAL	S	F–C	P–M	R		R	F		F–C					F		R–F		F	F			F			R		F				F	F	F	Reworked late Miocene forms
15H-1, 10	127.10	142.10	PAL	S	F–C	M			R–F	F		F		R			F		F	T	F				R			F		F			T	F	F–C	F	
15H-1, 13	127.13	142.13	PAL	S	C	M–G			R–F	F	R	F		R–F			F		F			F			F			F		F	R–F				F–C	F	
15H-2, 135	129.86	144.86	PAL	S	F	G			R–F		R	F		R–F			F		F			F			F			F		F	R–F			F	F–C	F	*Thalassiothrix* ooze
15H-2, 139	129.90	144.90	PAL	S	F	M–G			R			F–C		R			F	T			F	F						F		F–C	F–C	F		F	F	F	*Thalassiothrix* ooze
15H-CC, 21	136.94	151.94	PAL	S	F–C	P–M				R		F–C					F	T		T	F	F			F			F		F	F–C			F	F	F	
16H-CC, 34	146.53	163.03	PAL	S	C	M–G	T			R		F					F		T								F			F							F	Reworked late Miocene forms
17H-CC, 21	155.99	174.04	PAL	S	A	M		R				F					F		F								F			F	F			F		F	
18H-CC, 40	165.58	184.54	PAL	S	C	G				F	F	F	F	F	T	C	R		F	T				T	F				F	C	T	T		F	F–C	F	Thalassionema–Thalassiothrix rich, reworked late Miocene forms
19H-4, 75	170.25	190.62	PAL	S	F–C	G	T				T	F	F	T		T	R		R–F	T	R–F	F			R					R	R			F	F	F	
19H-6, 75	173.25	193.64	PAL	S	F–C	M				R	R	F	F	R		F	F		F		F	F			R–F			F		R	F			F	F	F	Reworked late Miocene forms
19H-7, 40	174.40	194.80	PAL	S	F–C	M			R	F		F	F	R			F	T	F		F	F			F			F			F		T	F	F	F	
19H-CC, 20	174.84	195.24	PAL	S	F–C	M–G			R	R		A	R	R		F	F		R–F						R–F					VA				F	F		Thalassionema–Thalassiothrix rich, reworked late Miocene forms
20H-CC, 22	184.40	205.92	PAL	S	C–A	M–G				F		F	R	R		F			F						F					C				F	F–C		Reworked late Miocene forms
21H-CC, 12	193.74	215.29	PAL	S	F–C	M–G	T		F	R		F	R	F		F	R–F		F		T				R					C–A				F	F–C		Reworked late Miocene forms
22H-CC, 20	203.46	224.97	PAL	S	C–A	M–G				F		F	R						F	R		F	R		F			F		F				F	F	F	Reworked late Miocene forms

Table T13 (continued).

Core, section, interval (cm)	Depth (mbsf)	Depth (mcd)	Identification	Method	Abundance	Preservation	*Actinocyclus ellipticus*	*Actinocyclus ellipticus* v. *lanceolata*	*Actinocyclus* spp.	*Actinoptychus senarius*	*Asteromphalus* spp.	*Azpeitia nodulifera*	*Chaetoceros* spp. (resting spores)	*Coscinodiscus* spp.	*Diploneis bombus*	*Fragilariopsis doliolus*	*Hemidiscus cuneiformis*	*Nitzschia cylindrica*	*Nitzschia marina*	*Nitzschia miocenica*	*Nitzschia reinholdii*	*Nitzschia fossilis*	*Nitzschia jousea*	*Paralia sulcata*	*Rhizosolenia* spp.	*Rhizosolenia matuyama*	*Rhizosolenia praebergonii robusta*	*Rhizosolenia praebergonii*	*Rossiela paleacea*	*Stephanopyxis* spp.	*Thalassionema* spp.	*Thalassionema convexa*	*Thalassionema convexa aspinosa*	*Thalassionema miocenica*	*Thalassionema oestrupii*	*Thalassiosira* spp.	*Thalassiothrix* spp.	Remarks
23H-CC, 20	212.96	235.31	PAL	S	F–C	G		F		F		F–C	R	R			F	T	F	T					R–F			F		R	F	F–C				C	F	Reworked late Miocene forms
24H-CC, 8	222.36	245.88	PAL	S	C	M	T			R	T	F	R–F			F	R		R–F			T			F					C–A				F		F	Reworked late Miocene forms
25H-CC, 21	232.01	257.18	PAL	S	F–C	M				R–F		F	R–F	T		R	F			T					R					R						F	Reworked late Miocene forms
26H-CC, 20	241.47	268.35	PAL	S	C–A	M–G						F	T	F		F	R				T	F			F	F				F				F	R	F	Reworked late Miocene forms
27H-CC, 31	251.09	278.67	PAL	S	C	M							T			R	R–F				T	T			F					F				F		F	Reworked late Miocene forms
28H-CC, 0	254.27	282.84	PAL	S	F	M	T		T	R–F		R	T	T		R	T		T		F	F			R		R			F				F		F	Reworked late Miocene forms

Notes: PAL = paleontology sample. S = smear slide. Abundance: A = abundant, C = common, M = moderate, F = few, R = rare, T = trace.

Table T14. Determinations of polarity chron boundaries, Site 1240.

	202-1240A-		202-1240B-			
Polarity interval	Depth (mcd)	Comments	Depth (mcd)	Comments	Polarity chron interpretation	Age (Ma)
Upper	68.0				C1n (b) Matuyama/Brunhes	
Middle		Core break			C1n (b) Matuyama/Brunhes	0.78
Lower	72.0				C1n (b) Matuyama/Brunhes	
Upper	78.0				C1r.1n (t) Jaramillo	
Middle		Core break			C1r.1n (t) Jaramillo	0.99
Lower	87.0				C1r.1n (t) Jaramillo	
Upper	93.0		92.5		C1r.1n (b) Jaramillo	
Middle		Mixed polarity		Core break	C1r.1n (b) Jaramillo	1.07
Lower	132.0		99.5		C1r.1n (b) Jaramillo	
Upper	162.0		168.5		C2n (t) Olduvai	
Middle		Mixed polarity		Mixed polarity	C2n (t) Olduvai	1.77
Lower	176.0		175.5		C2n (t) Olduvai	
Upper	194.0		198.5		C2n (b) Olduvai	
Middle		Mixed polarity		Core break	C2n (b) Olduvai	1.95
Lower	206.0		201.0		C2n (b) Olduvai	
Upper	256.5		251.0		C2An.1n (t) Gauss/Matuyama	
Middle		Mixed polarity		Mixed polarity	C2An.1n (t) Gauss/Matuyama	2.581
Lower	265.0		259.0		C2An.1n (t) Gauss/Matuyama	

Note: (b) = bottom, (t) = top.

Table T15. Paleomagnetic age control points based on polarity chron boundary interpretation, Site 1240.

Shipboard polarity chron boundaries interpretation	Age (Ma)	Depth (mcd)	Error (±m)
C1n/1r	0.78	70	2
C1r.1r/1r.1n	0.99	82	5
C1r.1n/1r.2r	1.07	96	4
C1r.2r/2n	1.77	172	4
C2n/2r	1.95	200	3
C2r/2An	2.581	257	7

Table T16. Headspace gas concentrations and C_1/C_2 ratios, Hole 1240A.

Core, section, interval (cm)	Depth (mbsf)	Depth (mcd)	C_1 (ppmv)	C_2 (ppmv)	C_1/C_2
202-1240A-					
1H-3, 0–5	2.82	2.82	1.9		
2H-4, 0–5	8.03	9.38	1.8		
3H-4, 0–5	17.52	19.47	2.7		
4H-4, 0–5	27.02	31.12	6.6		
5H-4, 0–5	36.52	41.82	10.6		
6H-4, 0–5	46.04	54.44	13.0		
7H-4, 0–5	55.53	62.98	19.2		
8H-4, 0–5	65.02	75.36	22.2		
9H-4, 0–5	74.52	83.67	19.4		
10H-4, 0–5	84.02	93.92	32.2		
11H-4, 0–5	93.40	103.57	18.9		
12H-4, 0–5	103.00	115.45	48.0		
13H-4, 0–5	112.51	125.36	32.6		
14H-4, 0–5	122.01	135.16	46.3	0.90	51.4
15H-4, 0–5	131.52	146.52	57.4	1.20	47.8
16H-4, 0–5	141.00	157.50	26.8		
17H-4, 0–5	150.52	168.57	41.4	1.00	41.4
18H-4, 0–5	160.00	178.95	29.2		
19H-4, 0–5	169.52	189.87	34.6	0.70	49.4
20H-4, 0–5	179.03	200.48	31.3		
21H-4, 0–5	188.51	210.01	33.1		
22H-4, 0–5	198.02	219.47	35.2	0.80	44.0
23H-4, 0–5	207.52	229.82	20.1		
24H-4, 0–5	217.03	240.48	16.2		
25H-4, 0–5	226.53	251.63	18.9		
26H-4, 0–5	236.03	262.83	10.7		
27H-4, 0–5	245.53	273.03	8.8		

Table T17. Interstitial water geochemical data, Hole 1240A.

Core, section, interval (cm)	Depth (mbsf)	Depth (mcd)	pH	Alkalinity (mM)	Salinity	Cl^- (mM)	Na^+ (mM)	SO_4^{2-} (mM)	HPO_4^{2-} (µM)	NH_4^+ (mM)	H_4SiO_4 (µM)	Mn^{2+} (µM)	Fe^{2+} (µM)	Ca^{2+} (mM)	Mg^{2+} (mM)	B (µM)	Sr^{2+} (µM)	Ba^{2+} (µM)	Li^+ (µM)	K^+ (mM)
202-1240A-																				
1H-1, 145–150	1.45	1.45	7.76	3.0	35.0	551	476	28.5	5	BDL	601	54.6	0.3	10.3	52.0	435	85	3.2	25	10.8
2H-3, 145–150	7.97	9.32	6.91	2.9	35.0	554	472	27.7	5	BDL	696	51.2	0.6	10.5	54.0	466	85	1.9	24	12.0
3H-3, 145–150	17.47	19.42	7.03	3.3	35.0	555	478	27.7	5	0.19	708	62.9	1.9	10.1	52.1	452	85	2.7	25	11.3
4H-3, 145–150	26.96	31.06	7.16	5.3	35.0	562	481	25.3	8	0.52	760	74.8	1.1	8.8	53.9	501	86	2.2	26	11.5
5H-3, 145–150	36.46	41.76	7.53	6.5	35.0	561	477	22.9	8	0.69	764	55.7	1.7	7.5	54.8	507	84	1.2	26	11.4
6H-3, 145–150	45.98	54.38	7.23	8.4	35.0	563	484	21.3	10	1.05	824	42.4	1.0	5.7	53.8	524	81	2.4	27	11.4
7H-3, 145–150	55.47	62.92	7.34	9.6	35.0	565	485	21.0	13	1.13	807	33.1	0.8	5.0	54.8	539	82	2.5	27	11.5
8H-3, 145–150	64.96	75.30	7.53	11.1	35.0	566	489	20.1	14	1.29	869	30.0	1.4	4.4	54.0	531	80	1.5	27	11.2
9H-3, 145–150	74.46	83.61	7.51	11.9	35.0	562	481	18.5	15	1.33	819	27.3	2.2	4.1	55.4	535	80	2.6	26	11.2
10H-3, 145–150	83.96	93.86	7.62	13.4	35.0	563	482	16.3	17	1.70	852	18.5	2.4	3.6	54.3	564	79	2.7	26	11.2
11H-3, 145–150	93.34	103.51	7.44	14.4	35.0	562	478	15.4	20	1.58	850	15.6	0.7	3.4	55.4	548	81	2.8	25	11.2
12H-3, 145–150	102.95	115.40	7.67	15.1	35.0	562	481	15.6	23	1.77	846	13.1	1.7	3.2	54.7	533	80	4.6	24	11.2
13H-3, 145–150	112.45	125.30	7.49	16.1	35.0	564	488	16.3	26	1.97	875	14.5	3.5	3.1	54.0	550	82	2.8	23	11.1
14H-3, 145–150	121.96	135.11	7.63	16.6	35.0	566	485	13.8	28	1.99	846	11.3	1.8	2.9	54.1	539	83	1.4	23	11.0
15H-3, 145–150	131.47	146.47	7.75	17.7	35.0	563	484	14.2	30	2.06	992	16.9	1.0	2.9	54.2	606	91	3.2	23	11.4
16H-3, 145–150	140.95	157.45	7.77	19.0	35.0	566	483	12.8	35	2.22	910	23.2	1.5	2.9	55.2	583	99	2.5	22	11.0
17H-3, 145–150	150.47	168.52	7.69	18.3	35.0	568	484	12.4	32	2.04	951	20.6	1.2	3.1	55.2	558	101	1.2	22	10.7
18H-3, 145–150	159.95	178.90	7.74	17.9	35.0	568	489	14.1	33	2.12	939	19.1	2.9	3.1	53.7	610	114	3.1	24	11.0
19H-3, 145–150	169.47	189.82	7.76	17.4	35.0	563	481	13.7	33	2.08	984	17.2	1.2	3.6	54.4	576	116	6.3	24	10.9
20H-3, 145–150	178.97	200.42	7.75	15.6	35.0	559	476	14.5	29	2.04	1052	14.1	1.5	4.0	54.6	565	125	4.9	24	10.7
21H-3, 145–150	188.47	209.97	7.69	14.6	35.0	561	477	15.0	23	1.92	976	11.7	1.7	4.3	54.0	557	133	2.1	24	11.8
22H-3, 145–150	197.97	219.42	7.53	13.2	35.0	564	482	15.7	21	1.67	943	6.5	1.2	5.0	52.8	620	143	3.6	28	10.7
23H-3, 145–150	207.47	229.77	7.61	9.8	35.0	564	482	17.7	14	1.49	939	6.2	4.0	5.9	51.9	654	177	6.0	33	11.0
24H-3, 145–150	216.97	240.42	7.66	9.8	35.0	567	489	19.1	11	1.38	1001	2.9	0.8	6.4	51.2	523	150	2.4	25	11.0
25H-3, 145–150	226.47	251.57	7.64	8.6	35.0	563	481	20.5	8	1.12	994	4.7	1.1	7.4	52.8	500	147	2.4	24	10.8
26H-3, 145–150	235.97	262.77	7.65	6.8	35.0	564	485	22.5	7	0.86	955	6.4	0.9	7.9	52.2	477	131	0.4	23	10.5
27H-3, 145–150	245.47	272.97	7.62	5.2	35.0	563	485	24.6	3	0.48	1003	5.0	0.6	8.8	52.1	471	119	1.3	22	10.4
28H-2, 145–150	253.46	282.01	7.47	2.8	35.0	557	475	25.7	2	0.17	739	3.3	1.1	9.4	53.4	433	87	0.3	23	10.7

Note: BDL = below detection limit (NH_4^+ = 0.15 mM).

Table T18. Inorganic carbon, calcium carbonate, total carbon, total organic carbon, total organic carbon on a carbonate-free basis, and total nitrogen concentrations, and TOC/TN ratios, Hole 1240A. (**See table note.** Continued on next page.)

Core, section, interval (cm)	Depth (mbsf)	Depth (mcd)	IC (wt%)	$CaCO_3$ (wt%)	TC (wt%)	TOC (wt%)	TOC CFB (wt%)	TN (wt%)	TOC/TN (atomic)
202-1240A-									
1H-1, 74–75	0.74	0.74	6.05	50.4					
1H-2, 74–75	2.25	2.25	7.09	59.1					
1H-3, 20–21	3.02	3.02	6.66	55.5	6.92	0.26	0.57	0.23	0.94
2H-1, 74–75	4.24	5.59	5.98	49.8	7.17	1.19	2.37	0.17	6.08
2H-2, 74–75	5.75	7.10	5.45	45.4					
2H-3, 74–75	7.26	8.61	5.86	48.8	7.35	1.49	2.91	0.20	6.29
2H-4, 74–75	8.77	10.12	4.99	41.6					
2H-5, 74–75	10.28	11.63	6.12	51.0	6.95	0.83	1.68	0.13	5.49
2H-6, 74–75	11.79	13.14	5.92	49.3					
3H-1, 74–75	13.74	15.69	6.71	55.9	8.23	1.52	3.45	0.20	6.55
3H-2, 74–75	15.25	17.20	6.06	50.5					
3H-3, 74–75	16.76	18.71	6.38	53.1	7.49	1.11	2.37	0.16	5.96
3H-4, 74–75	18.26	20.21	7.38	61.5					
3H-5, 74–75	19.77	21.72	4.46	37.1	5.28	0.82	1.30	0.15	4.80
3H-6, 74–75	21.28	23.23	7.33	61.0					
3H-7, 20–21	22.24	24.19	7.34	61.1	8.08	0.74	1.91	0.13	5.01
4H-1, 74–75	23.24	27.34	8.44	70.3	9.45	1.01	3.38	0.15	5.59
4H-2, 74–75	24.75	28.85	7.47	62.3					
4H-3, 74–75	26.25	30.35	7.69	64.1	8.39	0.69	1.93	0.10	5.78
4H-4, 74–75	27.76	31.86	8.83	73.6					
4H-5, 74–75	29.26	33.36	7.51	62.6	8.60	1.09	2.91	0.14	6.76
4H-6, 74–75	30.77	34.87	8.77	73.1					
4H-7, 20–21	31.73	35.83	8.93	74.4	9.48	0.55	2.14	0.11	4.39
5H-1, 74–75	32.74	38.04	8.85	73.7	9.47	0.62	2.36	0.09	5.68
5H-2, 74–75	34.24	39.54	8.17	68.1					
5H-3, 74–75	35.75	41.05	8.50	70.8	9.17	0.67	2.29	0.10	5.92
5H-4, 74–75	37.26	42.56	9.10	75.8					
5H-5, 74–75	38.76	44.06	9.64	80.3	9.99	0.35	1.76	0.08	3.78
5H-6, 74–75	40.27	45.57	8.94	74.5					
5H-7, 20–21	41.24	46.54	8.32	69.3	8.66	0.34	1.12	0.08	3.49
6H-1, 74–75	42.24	50.64	8.17	68.0	8.58	0.41	1.28	0.07	4.74
6H-2, 74–75	43.76	52.16	7.83	65.2	8.34	0.51	1.48	0.08	5.29
6H-3, 74–75	45.27	53.67	8.05	67.0					
6H-4, 74–75	46.78	55.18	6.46	53.8					
6H-5, 74–75	48.29	56.69	7.35	61.2	7.93	0.58	1.50	0.09	5.36
7H-1, 74–75	51.74	59.19	7.88	65.7	8.44	0.56	1.62	0.09	5.12
7H-3, 74–75	54.76	62.21	8.06	67.1	8.51	0.45	1.37	0.09	4.11
7H-5, 74–75	57.78	65.23	6.74	56.1	7.33	0.59	1.34	0.10	4.99
7H-7, 20–21	60.26	67.71	5.72	47.7	6.42	0.70	1.34	0.10	5.83
8H-1, 74–75	61.24	71.58	7.75	64.6	8.35	0.60	1.70	0.11	4.82
8H-3, 74–75	64.25	74.59	7.66	63.8					
8H-5, 74–75	67.27	77.61	7.92	66.0	8.91	0.98	2.90	0.13	6.65
9H-1, 74–75	70.74	79.89	7.69	64.0	8.11	0.42	1.15	0.09	3.91
9H-3, 74–75	73.75	82.90	7.49	62.4					
9H-5, 74–75	76.77	85.92	8.42	70.2	8.75	0.32	1.09	0.08	3.38
10H-1, 74–75	80.24	90.14	8.05	67.1	8.51	0.46	1.38	0.08	4.76
10H-3, 74–75	83.25	93.15	7.45	62.1					
10H-5, 74–75	86.26	96.16	5.93	49.4	6.53	0.60	1.18	0.10	4.98
11H-3, 74–75	92.63	102.80	6.94	57.8	7.28	0.34	0.80	0.10	2.99
11H-5, 74–75	95.65	105.82	7.70	64.2	8.18	0.48	1.34	0.11	3.75
12H-1, 74–75	99.24	111.69	6.80	56.6	7.42	0.62	1.43	0.10	5.12
12H-3, 74–75	102.24	114.69	6.38	53.2	6.94	0.56	1.20	0.10	4.94
12H-5, 74–75	105.24	117.69	4.80	40.0	5.24	0.44	0.74	0.10	3.96
13H-1, 74–75	108.74	121.59	6.40	53.3	7.00	0.60	1.29	0.10	5.28
13H-3, 74–75	111.74	124.59	7.73	64.4	8.25	0.52	1.47	0.10	4.40
13H-5, 74–75	114.75	127.60	5.40	45.0	6.12	0.72	1.32	0.13	4.67
14H-1, 74–75	118.24	131.39	6.56	54.6	7.05	0.49	1.07	0.24	1.70
14H-3, 74–75	121.25	134.40	6.26	52.2	7.04	0.78	1.62	0.14	4.81
14H-5, 74–75	124.26	137.41	5.85	48.7	6.82	0.97	1.88	0.17	4.81
15H-1, 74–75	127.74	142.74	5.32	44.3	7.52	2.20	3.96	0.37	5.13
15H-3, 74–75	130.76	145.76	5.48	45.7	7.40	1.92	3.54	0.46	3.62
15H-5, 74–75	133.76	148.76	4.46	37.1	7.54	3.08	4.89	0.47	5.67
16H-1, 74–75	137.24	153.74	4.79	39.9	6.07	1.28	2.13	0.33	3.29
16H-3, 74–75	140.24	156.74	6.28	52.3	7.35	1.07	2.25	0.15	6.20

Table T18 (continued).

Core, section, interval (cm)	Depth (mbsf)	Depth (mcd)	IC (wt%)	$CaCO_3$ (wt%)	TC (wt%)	TOC (wt%)	TOC CFB (wt%)	TN (wt%)	TOC/TN (atomic)
16H-5, 74–75	143.24	159.74	4.82	40.1	7.02	2.20	3.68	0.24	7.96
17H-1, 74–75	146.74	164.79	5.31	44.2	6.69	1.38	2.47	0.18	6.69
17H-3, 74–75	149.76	167.81	5.19	43.2					
17H-5, 74–75	152.77	170.82	3.94	32.8	5.89	1.95	2.91	0.21	8.17
18H-1, 74–75	156.24	175.19	2.73	22.8	5.83	3.10	4.02	0.29	9.04
18H-3, 74–75	159.24	178.19	4.74	39.5					
18H-5, 74–75	162.24	181.19	5.17	43.1	7.72	2.55	4.48	0.44	4.99
19H-1, 74–75	165.74	186.09	4.79	39.9	7.16	2.37	3.95	0.44	4.62
19H-3, 74–75	168.76	189.11	5.27	43.9					
19H-5, 74–75	171.77	192.12	4.90	40.8	6.45	1.55	2.62	0.18	7.52
20H-1, 74–75	175.24	196.69	4.68	39.0	6.54	1.86	3.04	0.19	8.37
20H-3, 74–75	178.26	199.71	4.89	40.7					
20H-5, 74–75	181.28	202.73	4.37	36.4	6.64	2.27	3.58	0.24	8.19
21H-1, 74–75	184.74	206.24	3.66	30.5	6.16	2.50	3.60	0.70	3.07
21H-3, 74–75	187.76	209.26	6.30	52.5					
21H-5, 74–75	190.76	212.26	7.94	66.1	9.21	1.27	3.76	0.46	2.39
22H-1, 74–75	194.24	215.69	8.21	68.4	8.87	0.65	2.07	0.37	1.54
22H-3, 74–75	197.26	218.71	4.79	39.9					
22H-5, 74–75	200.27	221.72	7.59	63.2	8.42	0.83	2.25	0.21	3.43
23H-1, 74–75	203.74	226.04	7.58	63.2	8.46	0.88	2.40	0.11	6.88
23H-3, 74–75	206.76	229.06	7.19	59.9					
23H-5, 74–75	209.77	232.07	7.16	59.6	7.92	0.76	1.88	0.06	10.22
24H-1, 74–75	213.24	236.69	8.07	67.2	8.61	0.54	1.64	0.05	10.09
24H-3, 74–75	216.26	239.71	8.70	72.5					
24H-5, 74–75	219.28	242.73	5.75	47.9	7.05	1.30	2.49	0.13	8.42
25H-1, 74–75	222.74	247.84	7.89	65.7	8.42	0.53	1.55	0.07	6.60
25H-3, 74–75	225.76	250.86	6.12	50.9					
25H-5, 74–75	228.78	253.88	7.18	59.8	7.71	0.53	1.31	0.05	9.53
26H-1, 74–75	232.24	259.04	5.44	45.3	6.82	1.38	2.53	0.15	7.95
26H-3, 74–75	235.26	262.06	6.54	54.4					
26H-5, 74–75	238.28	265.08	7.66	63.8	8.02	0.36	0.98	0.04	7.13
27H-1, 74–75	241.74	269.24	7.46	62.1	7.85	0.39	1.03	0.04	8.42
27H-3, 74–75	244.76	272.26	5.40	45.0					
27H-5, 74–75	247.78	275.28	7.55	62.9	8.17	0.62	1.66	0.05	10.56
28H-1, 70–71	251.20	279.75	7.97	66.4	8.28	0.31	0.91	0.03	8.68
28H-3, 20–21	253.72	282.27	9.07	75.6	9.26	0.19	0.77	0.01	13.97

Note: IC = inorganic carbon, TC = total carbon, TOC = total organic carbon, CFB = carbonate-free basis, TN = total nitrogen.

Table T19. Results of Rock-Eval pyrolysis analyses of selected sediment samples, Hole 1240A.

Core, section, interval (cm)	Depth (mbsf)	Depth (mcd)	TOC (wt%)	S_1 (mg/g)	S_2 (mg/g)	T_{max} (°C)	HI (mg HC/g C)
202-1240A-							
15H-3, 74–75	130.76	145.75	1.92	0.69	6.95	415	362
15H-5, 74–75	133.76	148.76	3.08	0.96	11.19	417	363
16H-3, 74–75	140.24	156.74	1.07	0.43	2.72	416	254
17H-1, 74–75	146.74	164.79	1.38	0.50	4.66	419	338
19H-1, 74–75	165.74	186.09	2.37	0.89	8.99	419	379
19H-5, 74–75	171.77	192.12	1.55	0.54	5.73	420	370
20H-1, 74–75	175.24	196.69	1.86	0.56	6.68	421	359
21H-1, 74–75	184.74	206.24	2.50	0.98	9.38	416	375
21H-5, 20–21	190.76	212.26	1.27	0.37	4.69	425	369

Notes: TOC = total organic carbon. S_1 = amount of volatile hydrocarbons, S_2 = amount of hydrocarbons due to thermal cracking of kerogen. T_{max} = peak temperature of kerogen breakdown. HI = hydrogen index ($100 \times S_2$/TOC).

Table T20. Age-depth model, linear sedimentation rates, and mass accumulation rates, Site 1240.

Age (Ma)	Depth (mcd)	LSR (mcd/m.y.)	mcd growth factor	Corrected LSR (m/m.y.)	Dry density (g/cm^3)	$CaCO_3$ average concentration (wt%)	TOC average concentration (wt%)	Total MAR ($g/cm^2/k.y.$)	$CaCO_3$ MAR ($g/cm^2/k.y.$)	TOC MAR ($g/cm^2/k.y.$)	Noncarbonate MAR ($g/cm^2/k.y.$)
0.0	0.0										
0.4	35.1	88	1.11	79	0.44	56.2	0.49	3.5	2.0	0.017	1.5
0.8	71.1	90	1.11	81	0.58	67.0	0.37	4.7	3.1	0.017	1.5
1.2	102.9	80	1.11	72	0.56	62.7	0.37	4.0	2.5	0.015	1.5
1.6	135.0	80	1.11	72	0.55	53.7	0.58	3.9	2.1	0.023	1.8
2.0	205.8	177	1.11	160	0.47	40.8	1.57	7.5	3.1	0.118	4.4
2.4	244.3	96	1.11	87	0.63	57.6	0.73	5.5	3.1	0.040	2.3

Notes: LSR = linear sedimentation rate, MAR = mass accumulation rate. TOC = total organic carbon. This table is also available in **ASCII.**